

COMPLEX DYNAMICS OF LOCALIZED PATTERNS IN
REACTION-DIFFUSION SYSTEMS

by

Shuangquan Xie

Submitted in partial fulfillment of the
requirements for the degree of
Doctor of Philosophy

at

Dalhousie University
Halifax, Nova Scotia
August 2017

© Copyright by Shuangquan Xie, 2017

Table of Contents

List of Tables	iv
List of Figures	v
Abstract	vi
List of Abbreviations and Symbols Used	vii
Acknowledgements	viii
Chapter 1 Introduction	1
Chapter 2 Oscillation of Many Interfaces in the Near-shadow Regime of Two Component Reaction-diffusion System	10
2.1 The Derivation of a Moving Boundary Problem	12
2.2 Long Time Behaviour of N Interfaces	15
2.3 Dynamics of $2K$ Interfaces	25
2.4 Discussion	27
Chapter 3 Moving and Jumping Spot in a Two Dimensional Reaction- diffusion Model	29
3.1 Equilibrium Solution	32
3.2 Some Properties of Function w	35
3.3 Stability: Large (Mode Zero) Eigenvalue	36
3.4 Small Eigenvalues	40
3.5 Estimating κ_1, κ_2 for Small A	45
3.6 Threshold Crossing	46
3.7 Rotating Spot	47
3.8 Green's Function For Rotating Spot	52
3.9 Discussion	55

Chapter 4	Dynamics of the Spot in Three Dimensional Schankenberg Model	58
4.1	Slow Spot Dynamics	59
4.1.1	Spot Dynamics with a Spatially Varying Feed-Rate	69
4.2	Discussion	74
Chapter 5	Multi-vortex Crystal Lattices in Bose-Einstein Condensates with a Rotating Trap	77
5.1	Vortex Dynamics	80
5.1.1	Single Vortex	81
5.1.2	Multiple Vortices	86
5.2	Multi-vortex Lattice Density, Isotropic Trap.	87
5.3	Two Vortices, Anisotropic Trap	90
5.4	Large N Limit with Strongly Anisotropic Trap	93
5.5	Discussion	97
Chapter 6	Conclusions and Future Research	99
Bibliography		102

List of Tables

4.1	Energy function	68
-----	---------------------------	----

List of Figures

1.1	Patterns in nature	1
1.2	Interface configuration	6
2.1	Four interfaces oscillate	11
2.2	The interfaces oscillate asynchronously	28
3.1	Moving and jumping spot	30
3.2	Hopf bifurcations values for height and position oscillations	31
3.3	Core problem	34
3.4	Radius of rotating spot	47
3.5	Complex spot trajectories	55
4.1	Core problem	60
4.2	κ_1 and κ_2	66
4.3	Comparison	73
5.1	Many vortices in isotropic trap	78
5.2	Vortices distribution comparison	81
5.3	Number of vortices N vs a	89
5.4	A pair of vortices	92
5.5	Vortices in elliptic trap	94
5.6	Strong anisotropic trap	96

Abstract

In this thesis we study complex dynamics of the localized patterns that occur in certain partial differential equations. We study three different types of localized patterns: interfaces in one dimension, spots in two and three dimensions, and vortices in two dimensions.

In the first part of the thesis, we study the oscillatory motion of multiple interfaces in one dimension for a certain class of reaction-diffusion systems. Within that class, we prove that the eventual fate of the system can be reduced to the study of a single interface.

We then study a pattern consists of a single spot within a circular domain in a two-dimensional Schnakenberg model. Depending on parameter regime, such a spot can undergo periodic height oscillations or oscillations in its position. These oscillations are due to the presence of two different Hopf bifurcations. We derive explicit thresholds on the parameters which delineate these two regimes. Beyond the Hopf bifurcation, we also study the motion of a rotating spot and characterise explicitly the radius and frequency of its rotation. In three-dimensional context, we derive the slow dynamics of spot patterns and extend the analysis to the spatially varying feeding rate case.

We then study vortex dynamics in the context of Bose-Einstein Condensates (BECs) with a rotating trap, with or without anisotropy. Starting with the Gross-Pitaevskii equation (GPE), we derive a novel reduced ODE system that governs the slow dynamics and stability of multiple co-rotating vortices. In the limit of many vortices, we derive the effective vortex crystal density and its radius. For an anisotropic potential, we show that a pair of vortices lying on the long (short) axis is linearly stable (unstable), which is in agreement with full PDE simulations. We then further investigate the many-vortex limit in the case of strong anisotropic potential. In this limit, the vortices tend to align themselves along the long axis, and we compute the effective one-dimensional vortex density.

In each case, extensive full numerical simulations are used to confirm our analytical predictions.

List of Abbreviations and Symbols Used

Δ	Laplace operator
\gg	much greater than
\ll	much less than
∇	Gradient operator
\sim	to leading order
BEC	Bose-Einstein Condensate
GPE	Gross-Pitaevskii equation
MFPT	mean first passage time
ODE	ordinary differential equation
PDE	partial differential equation

Acknowledgements

I would like to thank my supervisor, Prof. Theodore Kolokolnikov for his supporting and mentoring in completing this thesis. He has guided me with enthusiasm through this journey from beginning to end. I would also like to thank our collaborators, Justin Tzou, Michael Ward and Panayotis Kevrekidis. I appreciate the inspirational discussion with them. To the end, I would like to especially thank Prof. Michael Ward for so kindly supporting me as a visiting student of UBC for a year.

This work has been supported by Dalhousie graduate scholarship and NSGS Scholarship.

Chapter 1

Introduction

Formation of the localized patterns is one of the most frequently observed phenomena in many models of physics, chemistry, and biology. Many phenomena, including, but not limited to, cell differentiation, the reaction of chemicals, propagation of flame fronts, laser interference patterns and sea shell patterns, fall into this category. In



Figure 1.1: Pattern in nature: (a) Interfaces of polymer [1]. (b) Spots on the leopard skin [2]. (c) Vortices in Bose-Einstein Condensate [3].

this thesis, we study several classes of singularly perturbed models, exhibiting three different types of localized structures: interfaces in one dimension, spots in two and three dimensions, and vortices in two dimensions. These structures can exhibit very complex dynamics, which is the main topic of investigation here.

The first type is the pattern consists of multiple back-to-back interfaces. An example of a model exhibiting such structure is the FitzHugh Nagumo model [4]. This system was introduced as a simplification of the Hodgkin-Huxley equation that was derived as a model for the propagation of action potentials in the giant nerve axon of the squid. It can be written in the form [5]:

$$\begin{cases} \frac{\partial u}{\partial t} = D_u \frac{\partial^2 u}{\partial x^2} + u(1-u)(u-a) - v \\ \frac{\partial v}{\partial t} = D_v \frac{\partial^2 v}{\partial x^2} + b(u-v) \end{cases} \quad (1.1)$$

where u represents the combined membrane voltage and sodium activation, v represents the combined sodium inactivation and potassium activation, a is the excitation threshold, b is the ratio of time scales, and the diffusion coefficients, D_u and D_v , are constants. This model has been widely studied as a qualitative prototype for excitable systems in many biological and chemical contexts.

The second type of patterns that we consider consist of “spikes” or “spots”, such as shown in the figure 1.1(b). A simple model that can produce this pattern is the Schnakenberg model [6]:

$$\begin{cases} \frac{\partial v}{\partial t} = D_1 \Delta v + k_1 b - k_2 v + k_3 v^2 u \\ \frac{\partial u}{\partial t} = D_2 \Delta u + k_4 a - k_3 v^2 u \end{cases} \quad (1.2)$$

It is a particular case of the activator-substrate system, where u and v are the concentration of two chemicals X and Y , Y is consumed by a slowly diffusing activator X , and supplied to the system at a constant rate. At the same time, X activates itself. This mechanism drives sharply localized spatial spots of activator coupled with nearby shallow dips of the substrate. It was originally formulated as a simplified model of a trimolecular autocatalytic reaction with diffusion. It is also a limiting case of both the Gray-Scott model [7] as well as the Klausmeyer model of vegetation pattern formation on flat ground when the water evaporation is limited [8]. Some applications of Schnakenberg model to biology include pattern formation in embryogenesis and skin patterns [9, 10].

The third type of pattern is a vortex pattern. A vortex is a region in a fluid in which the flow rotates around an axis line. Vortex patterns are widely observed in fluid dynamics. A mathematical model that can be used to describe the dynamics of the condensate at zero temperature is the Gross–Pitaevskii equation (GPE) [11]:

$$i\hbar \frac{\partial \Psi}{\partial t} = \left(-\frac{\hbar}{2m} \nabla^2 + V(r) + g|\Psi(r, t)|^2 \right) \Psi(r, t) \quad (1.3)$$

where m is the mass of the atoms of the condensate, $|\Psi|^2$ is the atomic density, $V(r)$ represents an external potential and g is a parameter that measures the atomic interactions. The GPE is effectively a mean-field approximation for the interparticle interactions. If we consider the case of a boson in one dimension in a uniform potential, we will get dark soliton solution or bright soliton solution depending on the type of

interaction. Dark soliton shows a deficit of condensate in a space of nonzero density, represented by a sharp interface. Bright soliton exhibits a concentration of condensate in the space of zero density, represented by a spike shape. Vortex patterns emerge in two and higher dimensions and are the analogues of bright soliton in 1-D.

A large body of literature exist, describing the formation and dynamics of localized patterns in such models. We focus on the translation instability and the dynamics of such patterns beyond the instability. The method of matched asymptotic expansions is the main tool we use to solve singularly perturbed differential equations. The idea is to reduce the original PDE system to a much simpler system by formal asymptotic methods. Since the reduced system preserves the essential properties such as location and mass of the localized structure, we are able to retrieve these key properties of the initial system by a detailed analysis of the reduced system.

Many problems presented in the thesis share a common theme: moving singularities in PDE systems. In the asymptotic limit, the localized structure reduces to a singularity such as a delta function in case of a spot or a vortex, or a step function (i.e. the integral of a delta function) in the case of a one-dimensional interface. We try to understand how these singularities move and interact with environment and each-other. Eventually we aim at characterizing the trajectories of these singularities.

Overview of Thesis

In Chapter 2, we consider the general class of two-component reaction-diffusion systems on a finite domain that admit interface solutions in one of their components, and we study the dynamics of n interfaces in one dimension. In the limit where the second component has large diffusion, we fully characterize the possible behaviours of n interfaces. We show that after the transients die out, the motion of n interfaces is described by the motion of a *single* interface on the domain that is $1/n$ the size of the original domain. Depending on parameter regimes and initial conditions, one of the following three outcomes results: (1) some interfaces collide; (2) all n interfaces reach a symmetric steady state; (3) all n interfaces oscillate indefinitely. In the latter case, the oscillations are described by a simple harmonic motion with even-numbered interfaces oscillating in phase while odd-numbered interfaces are oscillating in anti-phase. The work has been published in [19].

In Chapter 3, we consider a single spot solution for the Schnakenberg Model in a two-dimensional unit disk in the singularly perturbed limit of a small diffusivity ratio. For large values of the reaction-time constant, this spot can undergo two different types of instabilities, both due to a Hopf bifurcation. The first type induces oscillatory instability in the height of the spot. The second type induces a periodic motion of the spot center. We use formal asymptotics to investigate when these instabilities are triggered, and which one dominates. In the parameter regime where spot motion occurs, we construct a periodic solution consisting of a rotating spot, and compute its radius of rotation and angular velocity. Detailed numerical simulations are performed to validate the asymptotic theory, including rotating spots. More complex, non-circular spot trajectories are also explored numerically. The results of Chapter 3 have been published in [20]

In Chapter 4, we extend our two-dimensional calculation to a three-dimensional context. We provide the first systematic asymptotic study of the dynamics of spot patterns in an arbitrary bounded 3-D domain for a two-component singularly perturbed RD system. It is shown that the locations of spots in a quasi-equilibrium configuration evolve on a long time-scale according to an ODE system characterized by a gradient flow of a certain discrete energy, the minima of which define stable equilibrium points of the ODE. The theory also illustrates that new equilibrium points can be created when the feeding rate is spatially variable, and that finite-time pinning away from minima of the energy can occur when feeding rate is localized. These results have been published in section 4 of the paper [21].

In Chapter 5, we use asymptotic techniques following [22] to derive a novel set of equations which describe the distribution of vortex lattices in rotating BEC. The equations we derive are valid for both isotropic and anisotropic case. We then use the new equations to study the following important limits: (1) Many vortices in an isotropic trap. By taking a continuum limit of the effective equations of motion, we derive the effective density of the vortex crystals, as well as the size of the lattice. In addition, this computation yields the *maximum* number of vortices that can form stable lattice configurations, as a function of rotation speed. (2) Many-vortices in the trap with high anisotropy. When the anisotropy is sufficiently high, the vortices align along the longer axis of the trap. In this limit, we compute the one-dimensional density

of the resulting vortex configuration by using techniques involving the Chebyshev polynomials. As in the isotropic case, this leads to an expression relating the maximum number of vortices in a stable configuration and other problem parameters such as the anisotropy and the rotation rate.

We finish in Chapter 6 with our conclusions and suggestions for future work.

Literature Review

• Oscillations In Reaction Diffusion System

The formation of Mesa patterns is one of the most prevalent phenomena observed in reaction-diffusion systems. A sequence of highly localized interfaces that is separated in space by regions where the solution is nearly constant constitutes such patterns. A large body of literature have been devoted to this topic in the last three decades. See for example [24–29] and references there in.

In this thesis, we are concerned with the following class of reaction-diffusion models:

$$\begin{cases} u_t = \varepsilon^2 u_{xx} + f(u, w) \\ \tau w_t = Dw_{xx} + g(u, w) \end{cases} \quad (1.4)$$

with homogeneous Neumann boundary conditions on a one dimensional interval.

According to Turing theory, under certain general conditions on nonlinearities f and g , when the diffusivity ratio D/ε^2 is large, the homogeneous solution becomes unstable and a stable heterogeneous solution develops. With some specific constrains on f and g that will be stated later, the system (1.4) admits a solution u consists of sharp back to back interfaces, which is called the “Mesa” pattern. A typical solution is shown in Figure 1.2. The construction of the mesa patterns and its stability is originally done by [24], where the author presented stability theorem for large amplitude singularly perturbed solutions (SPS) of reaction-diffusion systems on a finite interval. In [30, 31], for a special model, the author show that a K -mesa solution is stable under the assumption that $\tau = 0$ and $D = O(1)$. More specifically, if D exceeds an exponentially large upper bound, then the number of mesas is diminished through a coarsening process and if D is too small, then self-replication is observed until such time that DK^2 is large enough, where K is the number of the interfaces. Then an explicit sequence of threshold values $D_1 > D_2 > D_3 > \dots$, where D_i is

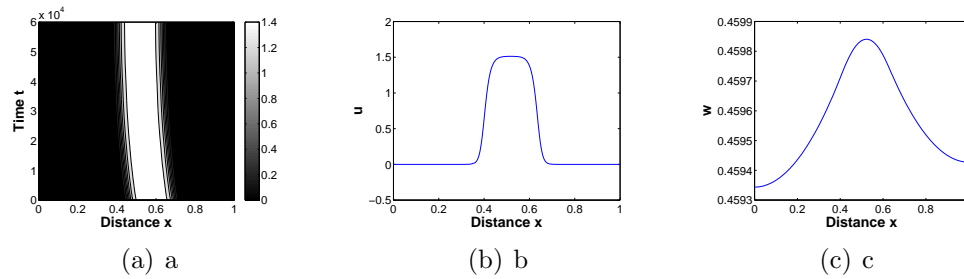


Figure 1.2: (a) Gierer-Meinhardt model with saturation, starting with random initial conditions. Time evolution of u is shown; the parameter values are $\varepsilon = 0.01$, $D = 100$, $\tau = 0$, $\kappa = 1$, domain size is 1 with Neumann boundary condition for both u and w . (b)(c) The snapshot of u and w at $t = 60000$.

exponentially large, determining the stability of the K mesa solution on the domain of a fixed size $2L$, is computed in [32]. For $\tau > 0$, It has been known for quite some time [33] that such interfaces can undergo a transition from a stationary state to an oscillatory motion, whereby interfaces exhibit a periodic motion in time, as the parameter τ is increased past some threshold τ_{hopf} . This was first reported in [33] for a system (1.4) with piecewise-linear nonlinearities f and g . Since then, similar oscillatory behavior was reported and analyzed in many other reaction diffusion systems in one and higher dimensions, see for example [34–39]. This change could be understood in the following way as stated in Rozada’s thesis [40]: “*when τ is small, the difference in diffusivity marks the $w(x)$ equation as the fast component in the system. However, if τ grows to be $O(\frac{1}{\varepsilon})$, or even bigger, the w equation will slow down and approach the time scale of the u equation. When this happens, feedback will happen between the two equations, leading to phenomena characteristic of delay differential equations such as oscillatory instabilities.*” In the paper [41], the “breather” motion of one or two interfaces was fully characterized with additional assumption $D \gg 1$. This assumption makes a detailed analysis possible by using the method of multiple scales even for values of τ well above the Hopf bifurcation threshold.

• Instability and Dynamics of the Schnakenberg Model

The Schnakenberg model often serves as a simple prototype model for studying pattern formation in reaction-diffusion systems: it is among the simplest class of models which

generate stable inhomogeneous patterns. As such, the Schnakenberg and related models such as Gray-Scott, the Brusselator, and the Gierer-Meinhardt model, have been extensively studied (especially in one, but also in two and higher dimensions), and phenomena such as spike formation, stability, self-replication, oscillations and motion has been analysed in detail. A very incomplete list of references includes [42–55].

Here we specify several results that are closely related to this model. In [44–46] the authors have found that a single spike in a one-dimensional Gray-Scott model can undergo destabilizing oscillations in *either* its height or position. The height oscillations happen on a much faster timescale when compared to the position oscillations. Which instability is triggered first depends on the value of the feed-rate A representing the amount of the substrate chemical that is being pumped into the system. Typically, height oscillations were triggered at lower feed rates than the position oscillations. Periodic spike motion in one dimensional GS model was further investigated in [54].

In one-dimensional domain, there has been much work over the past decade in analyzing the stability, dynamics, and self-replication of spike patterns for the Schnakenberg model and related models with similar structure. The stability problem for equilibrium spike patterns in infinite domain has been studied in [51] and [48] following earlier work on Gierer-Meinhardt model [56]. In [57], the authors studied Hopf bifurcations and oscillatory instabilities of spike solutions of Gierer-Meinhardt model for various ranges of the reaction-time constant. For a recent summary on pattern formation in GM model, see [58] and references therein. A detailed study of self-replication, overcrowding instability, and spike height and position oscillations for the Gray-Scott model is conducted in [43–46, 54, 59]. Self-replication in slowly growing domains was also studied in [60] and [61].

In two dimensions, Muratov and Osipov [47] were among the first to study the Gray-Scott model, including self-replication thresholds. Wei and Winter [49] reviewed analytical methods for a rigorous study of the existence and stability of stationary, multiple spots for reaction-diffusion systems and considered two classes of reaction-diffusion systems: activator-inhibitor systems (such as the Gierer-Meinhardt system) and activator-substrate systems (such as the Gray-Scott system or the Schnakenberg model). In [50], spot replication for the Schnakenberg model was studied. In [53], the authors studied multi-spot patterns including competition, spot motion, and

self-replication, for the related Gray-Scott model.

In three dimension context, only the limiting shadow problem, derived from the large inhibitor diffusivity limit, has been analyzed previously (cf. [62, 63]).

• Dynamics of vortices in a trapped Bose-Einstein condensate

Theoretical and experimental studies on vortices in rotating Bose-Einstein condensate has attracted great interest in the past 20 years, see, e.g., [78], the review [79] and the monograph [80] where extensive lists of references can be found. In most of the theoretical research, the GP model has served to study the emergence and dynamics of vortices. As an approximation of the quantum mechanical many-body problem, Gross-Pitaevskii theory was rigorously established in [81] for the non-rotating case and in [82] for rotating systems. One of the most interesting features observed experimentally is that when the angular speed gets larger, the number of vortices increases and they arrange themselves in a regular pattern around the center of the condensate [83, 84]. It is natural to explore the mechanism of this behavior mathematically. Under the framework of GP theory, the critical angular velocity was rigorously computed in [85, 86] and the distribution of the first few vortices to appear in the condensate in the condensate was studied in [87]. Another striking observation in the experiment is that the vortex lattices seem to be homogeneous when the matter density profile of the condensate imposed by the trap is not homogeneous [88, 89]. The relation between the matter density and the vortex density has been formulated and answered by [90, 91] based on formal argument. Then the author rigorously proved in [92] that the vortex distribution is strongly inhomogeneous close to the critical speed and gradually homogenizes when the rotation speed is increased.

There have been two approaches to the dynamics of vortices in an trapped condensate. The first approach is direct, it relies on the fact that GP equation is the Euler-Lagrange equation for the time-dependent Lagrangian functional under variation of the wave function. If the condensate wave function depends on one or more parameters, the resulting Lagrangian functional provides approximate Lagrangian equations of motion for these parameters [93]. Another approach is to study GP equation itself. Due to the two length scale in the problem: the size of vortex core and the inter-vortex distance, it is possible to employ the method of matched asymptotics

[94–97]. However, most of the literature focuses on the dynamics of one vortex with an isotropic potential and give a qualitative result about several vortices.

Chapter 2

Oscillation of Many Interfaces in the Near-shadow Regime of Two Component Reaction-diffusion System

The results in this chapter have appeared in [19]. We consider the following class of one-dimensional reaction diffusion systems:

$$\begin{cases} u_t = \varepsilon^2 u_{xx} + f(u, w) \\ \frac{\tau D}{\varepsilon} w_t = D w_{xx} + g(u, w) \end{cases} . \quad (2.1)$$

We are concerned with the regime:

$$\varepsilon \ll 1, \quad D \gg 1.$$

Suppose that there exists a constant w_0 and two constants $u_+ \neq u_-$ such that boundary value problem

$$U_{0yy} + f(U_0, w_0) = 0 \quad (2.2)$$

$$U_0(y) \rightarrow u_{\pm} \text{ as } y \rightarrow \mp\infty \quad (2.3)$$

admits a solution. Then $U_0(-y)$ also solves (2.2). The required conditions are that u_{\pm} and w_0 must satisfy

$$\int_{u_-}^{u_+} f(u, w_0) du = 0, \quad f(u_+, w_0) = 0 = f(u_-, w_0), \quad (2.4)$$

with $u_+ \neq u_-$. To be concrete, consider the following system of the general form (2.1),

$$\begin{cases} u_t = \varepsilon^2 u_{xx} + 2(u - u^3) + w \\ \tau_0 \frac{D}{\varepsilon} w_t = D w_{xx} - u + \beta \end{cases} . \quad (2.5)$$

For this special case of f and g , we may choose $w_0 = 0$, $u_{\pm} = \pm 1$, $U_0(y) = -\tanh(y)$. As was shown in [41], this system has a solution in the form of a single interface on a unit interval $x \in [0, 1]$ with $u(x, t) \sim \tanh((l(t) - x)/\varepsilon)$; $w \sim 0$, where

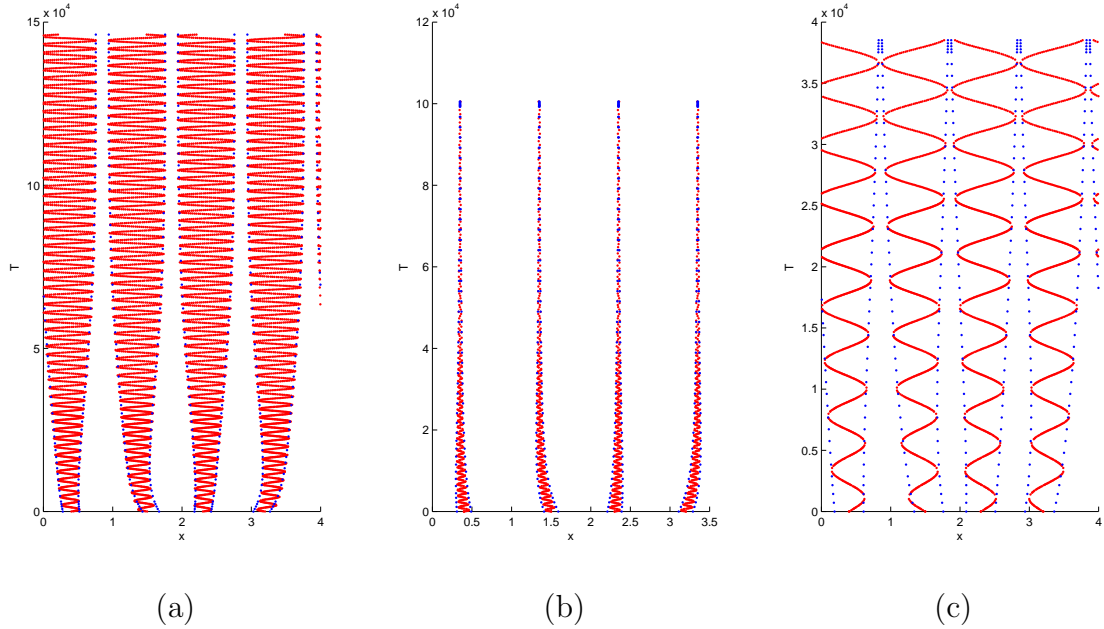


Figure 2.1: Simulation of the cubic model (2.5) with initial conditions consisting of four interfaces. Different initial conditions have been used to conduct the simulation and all of them show the same qualitative behaviours. Parameters are $\varepsilon = 0.01$, $D = 50$, $\beta = 0$ and with τ_0 as indicated. The red lines show the locations of interfaces corresponding to the roots of $u = 0$. The areas denoted by + and - correspond to the regions where $u \approx \pm 1$, respectively. The dotted lines correspond to the envelope computation of the interface locations as derived in section §2.3. (a) With $\tau_0 = 0.3$, oscillations eventually die out and four interfaces settle to a steady state. (b) With $\tau_0 = 1$, four interfaces eventually oscillate in synchrony. (c) With $\tau_0 = 3$, the oscillations increase until the interfaces collide resulting in the constant solution $u = -1$ thereafter. Asymptotics correctly predict the time of collision.

the interface location l oscillates according to the formula $l(t) = (1 + \beta)/2 + A(\varepsilon D^{-1}t) \cos(\sqrt{3/\tau_0} \varepsilon D^{-1/2}t + \phi_0)$ where the envelope A satisfies

$$A'(\varepsilon D^{-1}t) = \left(\frac{1}{4}(1 - 3\beta^2) - \frac{1}{8\tau_0} \right) A - \frac{3}{4}A^3.$$

Our goal in the chapter is to extend this computation to multiple interfaces. Our main conclusion is succinctly summarized as follows.

Main Result. *After the transients die out, the dynamics of n interfaces on the domain of size n follow the dynamics of a single interface on the domain of size one, copied over n times using even reflections.*

Figure 2.1(b) illustrates this conclusion. At the start, the four interfaces are

unevenly distributed. However they synchronize after a transient period, forming two phase-locked “breathers”. In the case of two interfaces, this result was already obtained in [41].

In § 2.1, we derive the moving boundary problem from [41].

In § 2.2, we conduct an analysis about the reduced system for n interfaces and reach our main conclusion.

In § 2.3, we give a autonomous dynamic system to describe the the motion of n interfaces.

2.1 The Derivation of a Moving Boundary Problem

Starting from equation (2.1), we first expand

$$u = u_0 + \frac{1}{D}u_1 + \dots, \quad w = w_0 + \frac{1}{D}w_1 + \dots .$$

to obtain

$$0 = \varepsilon^2 u_{0xx} + f(u_0, w_0), \tag{2.6}$$

$$Du_{0t} = \varepsilon^2 u_{1xx} + f_u(u_0, w_0)u_1 + f_w(u_0, w_0)w_1, \tag{2.7}$$

$$0 = w_{0xx}, \tag{2.8}$$

$$\frac{\tau}{\epsilon} w_{1t} = w_{1xx} + g(u_0, w_0) + \frac{1}{D}g_u(u_0, w_0)u_1 + \frac{1}{D}g_w(u_0, w_0)w_1. \tag{2.9}$$

In the subsequent analysis, the time scaling will be chosen in such a way that the term Du_{0t} is of the same order as the other terms in (2.7). Note that we also kept to $O(1/D)$ terms here for w_1 . These are not needed to compute the Hopf bifurcation threshold but are necessary for envelope calculation. Consider a single interface located at $x = \xi(t)$ in the domain $[0, 1]$, with $u \sim u_+$ for $0 < x < \xi$ and with $u \sim u_-$ for $\xi < x < 1$. In the inner region, we have

$$u_0(x, t) = U_0 \left(\frac{x - \xi(t)}{\varepsilon} \right) = U_0(y) \tag{2.10}$$

where U_0 is defined (2.2). Multiplying (2.6) by u_{0x} and integrating by parts over the domain, we obtain

$$-\xi'(t) \int_0^1 u_{0x}^2 dx = \frac{1}{D} \int_0^1 f_w w_1 u_{0x} dx. \tag{2.11}$$

where we neglected the exponentially small boundary terms. In the inner variables, we approximate $w_1 \sim w_1(\xi)$. After rearranging, we now have an equation for the dynamics of the interface

$$\xi_t = \frac{\varepsilon}{D} \frac{\int_{u_-}^{u_+} f_w du}{\int_{-\infty}^{\infty} U_{0y}^2 dy} w_1(\xi). \quad (2.12)$$

Away from the interface, we neglect the diffusion term u_{1xx} as well the left hand side in (2.7), so that

$$u_1 \sim -\frac{f_w(u_0, w_0)}{f_u(u_0, w_0)} w_1.$$

and we obtain a moving boundary problem

$$\frac{\tau}{\varepsilon} w_{1t} = w_{1xx} + g(x) + \frac{1}{D} \sigma(x) w_1 \quad (2.13)$$

where

$$g(x) = \begin{cases} g(u_+, w_0), & x < \xi \\ g(u_-, w_0), & x > \xi \end{cases},$$

$$\sigma(x) = \begin{cases} \left(g_w - \frac{f_w}{f_u} g_u \right)_{u=u_+, w=w_0}, & x < \xi \\ \left(g_w - \frac{f_w}{f_u} g_u \right)_{u=u_+, w=w_0}, & x > \xi \end{cases}.$$

and with ξ controlled by (2.12). A posteriori analysis suggests the following rescaling:

$$\tau = \tau_0 \frac{D}{\varepsilon}$$

$$w_1 = \sqrt{D} \frac{\int_{-\infty}^{\infty} U_{0y}^2 dy}{\int_{u_-}^{u_+} f_w du} \tau_0 W$$

$$t = \frac{\tau_0 \sqrt{D}}{\varepsilon} \hat{t}$$

which yields the scaled system

$$W_{xx} = \tilde{\varepsilon}(W_{\hat{t}} + h(x)) - \sigma(x) \tilde{\varepsilon}^2 W, \quad \frac{d}{d\hat{t}} \xi = W(\xi, \hat{t})$$

where

$$\tilde{\varepsilon} = \frac{1}{\sqrt{D}}, \quad h(x) = -g(x) \frac{\int_{u_-}^{u_+} f_w du}{\int_{-\infty}^{\infty} U_{0y}^2 dy} \tau_0.$$

Dropping the tilde yields the system.

$$\begin{cases} W_{xx} = \varepsilon(W_t + h(x)) - \sigma(x) \varepsilon^2 W \\ \frac{d}{dt} \xi = W(\xi, t) \\ W_x(0) = W_x(1) = 0 \end{cases} \quad (2.14)$$

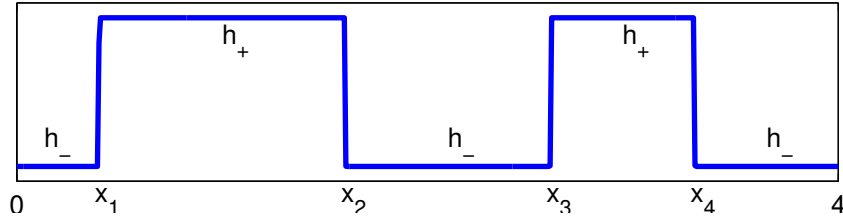
The reduced system for multiple interfaces is readily to derived in an identical manner. For the convenience of analysis, we will assume periodic boundary conditions for multiple interfaces solution. The periodicity requires an even number of interfaces, $n = 2K$, so that the value of u to the left of the leftmost interface is the same as its value to the right of the rightmost interface. However the result also holds for Neumann boundary conditions (in which case one can have an odd number of interfaces). This can be seen as follows: take the system that has n interfaces on a bounded interval with Neumann boundary conditions. Extend the solution using even reflection in space about either endpoint. Then the resulting system on the domain twice the size satisfies periodic boundary conditions and has $2n$ interfaces. We can then apply our results to the extended system to show that the $2n$ interfaces behave just like a single interface in the long-run. Therefore the same is true for the original system of n interfaces. We can reduce the motion of n interfaces to the following diffusion-type equation with n moving boundaries:

$$W_{xx} = \varepsilon(W_t + h(x)) - \sigma(x)\varepsilon^2 W \quad (2.15a)$$

$$\frac{d}{dt}x_i = (-1)^i W(x_i), \quad i = 1 \dots n, \quad n \text{ even} \quad (2.15b)$$

$$W \text{ is periodic on the domain } [0, n], \quad (2.15c)$$

where functions $h(x)$ and $\sigma(x)$ are piecewise constant, alternating between two values with jumps precisely at the interface locations x_j , as illustrated here for h :



that is

$$h = \begin{cases} h_- & \text{for } x \in (0, x_1) \cup (x_2, x_3) \cup \dots \cup (x_{2K-2}, x_{2K-1}) \cup (x_{2K}, n) \\ h_+ & \text{for } x \in (x_1, x_2) \cup (x_3, x_4) \dots \cup (x_{2K-1}, x_{2K}) \end{cases}$$

and similarly for σ . Note that the ε and t in (2.15) are not the same as the ε and t in (2.1). The n moving boundaries x_i represent interface locations ordered in increasing order. For the basic model (2.5), these functions are given by

$$h_{\pm} = \frac{3}{2}\tau_0(\pm 1 + \beta); \quad \sigma_+ = \sigma_- = -\frac{1}{4};$$

In [25], the authors took a similar approach of reducing the dynamics of a single interface to a free-boundary problem similar to (2.14). By solving this problem numerically (assuming piecewise-linear nonlinearities f , g , but without assuming that D is large), they also found that it can capture oscillatory dynamics of the interfaces. The authors also computed the eigenvalues of the associated linear problem analytically, showing directly the existence of the Hopf bifurcation. In a related work [36], the authors studied the motion of two interfaces for piecewise-linear nonlinearities f , g and without assuming large D . They showed the possibility of in-sync oscillations when the interfaces are very close to each other.

2.2 Long Time Behaviour of N Interfaces

In this section, we prove the main conclusion about n interfaces dynamics:

Proposition 2.2.1 *Consider the system (2.15) with $n = 2K$ interfaces and with $\varepsilon \ll 1$. Suppose that the interface locations x_i never cross each-other. Then in the limit $t \gg 1$, we have:*

$$\begin{aligned} x_{2j-1} &\sim -A \cos(\omega(t + \phi)) + (2j - 2) - l_0 + x_0, \quad j = 1 \dots K \\ x_{2j} &\sim A \cos(\omega(t + \phi)) + (2j - 2) + l_0 + x_0, \quad j = 1 \dots K \end{aligned}$$

where:

$$l_0 = -h_- / (h_+ - h_-)$$

and A is the stable equilibrium of the ODE

$$\frac{dA}{ds} = -\frac{A^3}{4} - \left(\frac{1}{6} - l_0 + l_0^2 + \frac{\sigma_- + (\sigma_+ - \sigma_-) l_0}{2} \right) A. \quad (2.16)$$

The proof of Theorem 2.2.1 is given in the following subsection. It depends lemmas 2.2.2 and 2.2.4 whose proofs are also given there, as well as lemma 2.2.3 previously proven in [41].

The proof of Theorem 2.2.1 is a direct consequence of the following two lemmas.

Lemma 2.2.2 *Consider the system (2.15). Suppose that the interface locations $x_j(t)$ never collide. Suppose that they are ordered in the increasing order $0 < x_1 < x_2 < \dots < x_{2K} < 2K$. Define*

$$m_1 = \frac{x_1 + x_2}{2}, \quad m_2 = \frac{x_3 + x_4}{2}, \quad \dots, \quad m_K = \frac{x_{2K-1} + x_{2K}}{2}$$

and similarly, define

$$\hat{m}_1 = \frac{x_2 + x_3}{2}, \quad \hat{m}_2 = \frac{x_4 + x_5}{2}, \quad \dots \quad \hat{m}_K = \frac{x_{2K} + (x_1 + 2K)}{2}$$

Then in the limit $t \rightarrow \infty$, we have the following properties:

$$m_{j+1} - m_j \rightarrow 2 \text{ as } t \rightarrow \infty, \quad j = 1 \dots K - 1 \quad (2.17)$$

$$\hat{m}_{j+1} - \hat{m}_j \rightarrow 2 \text{ as } t \rightarrow \infty, \quad j = 1 \dots K - 1. \quad (2.18)$$

Lemma 2.2.3 Consider the system

$$W_{xx} = \varepsilon(w_t + h(x; \xi)) - \varepsilon^2 \sigma(x; \xi) w \quad (2.19a)$$

$$\frac{d}{dt} \xi(t) = W(\xi, t) \quad (2.19b)$$

$$W_x = 0 \text{ at } x = 0, \text{ and } x = 1 \quad (2.19c)$$

$$h(x; \xi) = \begin{cases} h_+ & \text{if } 0 < x < \xi \\ h_- & \text{if } \xi < x < 1 \end{cases}; \quad \sigma(x; \xi) = \begin{cases} \sigma_+ & \text{if } 0 < x < \xi \\ \sigma_- & \text{if } \xi < x < 1 \end{cases}. \quad (2.19d)$$

In the limit $\varepsilon \rightarrow 0$, the system (2.15) has solution of the form

$$\xi(t) \sim A(s) \cos(\omega t + \phi_0) + l_0$$

where

$$s = \varepsilon t$$

$$\omega = \sqrt{h_+ - h_-};$$

$$l_0 = -h_- / (h_+ - h_-)$$

and A satisfies

$$A_s = -\frac{A^3}{4} - \left(\frac{1}{6} - l_0 + l_0^2 + \frac{\sigma_- + (\sigma_+ - \sigma_-) l_0}{2} \right) A. \quad (2.20)$$

Lemma 2.2.3 was proven in [41]; for completeness and reader's convenience, we include a slightly different derivation. We first prove Theorem 2.2.1 followed by the proof of Lemma 2.2.3 and 2.2.2.

Proof of Theorem 2.2.1. For reader's convenience, we will give the proof for four interfaces here; the proof is similar for $2K$ interfaces.

By lemma 2.2.2, there exist constants c_0 and c_1 such that for large t we have:

$$x_1(t) + x_2(t) \sim 2c_0 + 2 \quad (2.21)$$

$$x_2(t) + x_3(t) \sim 2c_1 + 4 \quad (2.22)$$

$$x_3(t) + x_4(t) \sim 2c_0 + 6 \quad (2.23)$$

$$x_4(t) + x_1(t) \sim 2c_1 + 4. \quad (2.24)$$

Taking (2.21)-(2.22)+(2.23)-(2.24) we obtain

$$c_0 = c_1.$$

By shifting x_j we may assume without loss of generality that $c_0 = c_1 = 0$. The resulting linear system (2.21-2.24) has a one-dimensional null space and its solution is parameterized by a free parameter ξ and may be written as

$$\begin{aligned} x_1(t) &\sim 1 - \xi(t), & x_2(t) &\sim 1 + \xi(t), \\ x_3(t) &\sim 3 - \xi(t), & x_4(t) &\sim 3 + \xi(t). \end{aligned}$$

This implies that the solution is an even periodic extension of the interval of size one copied over n times; in particular u is even around $x = 1, 2, 3, \dots, n - 1$. Therefore the solution in this regime is equivalent to an oscillation of a single interface on domain of size one with Neumann boundary conditions. This is precisely the situation captured by lemma 2.2.3, which concludes the proof. ■

Proof of lemma 2.2.3

We perform multiple scale analysis on (2.19). Introduce a slow-time scale

$$s = \varepsilon t, \quad w = W(x, t, s), \quad \xi = \xi(t, s)$$

Expand

$$W = W_0 + W_1\delta + W_2\delta^2 \dots$$

First, we expand

$$H(\xi - x) = H(\xi_0 + \varepsilon\xi_1 - x) = H(\xi_0 - x) + \varepsilon\xi_1\delta(\xi_0 - x) + O(\varepsilon^2)$$

where δ is the delta function. We therefore obtain

$$W_{0xx} = 0 \quad (2.25)$$

$$W_{1xx} = W_{0t} + c + dH(\xi_0 - x) \quad (2.26)$$

$$W_{2xx} = W_{1t} + W_{0s} + \xi_1 d\delta(x_0 - x) - \sigma W_0 \quad (2.27)$$

Similarly, expanding (2.19b) we obtain

$$\xi_{0t} = W_0(\xi_0, t, s) \quad (2.28)$$

$$\xi_{1t} + \xi_{0s} = \xi_1 W_{0x}(\xi_0, t, s) + W_1(\xi_0, t, s) \quad (2.29)$$

Equation (2.25) along with the boundary conditions $W_{0x} = 0$ at $x = 0, 1$ yields

$$W_0(x, t, s) = W_0(t, s).$$

Integrating equation (2.26) and using Neumann boundary conditions yields

$$W_{0t} + c + d\xi_0 = 0$$

so that the leading-order behaviour is

$$W_{0t} = -c - d\xi_0; \quad \xi_{0t} = W_0 \quad (2.30)$$

which is a harmonic oscillator assuming $d > 0$, whose solution is given by

$$\begin{aligned} \xi_0 &= l_0 + A(s) \sin(\omega t + \Phi), \\ W_0 &= \omega A(s) \cos(\omega t + \Phi) \end{aligned}$$

where we defined

$$l_0 := -c/d; \quad \omega^2 := d.$$

Substituting (2.30) into (2.26), W_1 satisfies

$$W_{1xx} = d(H(\xi_0 - x) - \xi_0).$$

The solution to W_1 is then given by

$$W_1 = dF(x) + V(t) \quad (2.31)$$

where F is the solution to

$$\begin{cases} F_{xx} = H(\xi_0 - x) - \xi_0, \\ F_x(0) = 0 = F_x(1), \\ \int_0^1 F(x) dx = 0. \end{cases}$$

Explicitly we obtain

$$F = \begin{cases} -\frac{\xi_0(x-1)^2}{2} + \frac{\xi_0 - \xi_0^2}{2} + A, & x > \xi_0 \\ \frac{(1-\xi_0)}{2}x^2 + A, & x < \xi_0 \end{cases}, \quad \text{where } A := \frac{\xi_0(2 - \xi_0)(\xi_0 - 1)}{6}$$

and evaluating at $x = \xi_0$ we have

$$F(\xi_0) = \frac{1}{3}\xi_0(2\xi_0 - 1)(1 - \xi_0). \quad (2.32)$$

Substituting (2.31–2.32), into (2.27) and integrating for $x = 0 \dots 1$ we obtain

$$0 = V_t + W_{0s} + \xi_1 d - \hat{\sigma} W_0 \quad (2.33)$$

where

$$\hat{\sigma} = (\sigma_+ - \sigma_-)\xi_0 + \sigma_- \quad (2.34)$$

and (2.29) simplifies to

$$\xi_{1t} + \xi_{0s} = dF(\xi_0) + V. \quad (2.35)$$

Eliminating V and V_t from (2.33) and (2.35) yields

$$\xi_{1tt} + \omega^2 \xi_1 = dF'(\xi_0)\xi_0' - 2W_{0s} + \{(\sigma_+ - \sigma_-)\xi_0 + \sigma_-\} W_0$$

where $\omega^2 := d$, so that

$$\xi_{1tt} + \omega^2 \xi_1 = d(F(\xi_0))_t - \omega [(2A_s - \{(\sigma_+ - \sigma_-)\xi_0 + \sigma_-\} A) \cos(\omega t + \Phi) - 2A\Phi_s \sin(\omega t + \Phi)] \quad (2.36)$$

Multiplying both sides of (2.36) by $\sin(\omega t + \Phi)$ and integrating on $t = 0 \dots 2\pi/\omega$ we obtain $A\Phi_s = 0$. Similarly, multiplying (2.36) by $\cos(\omega t + \Phi)$ we obtain

$$\begin{aligned} \int_0^{2\pi/\omega} d(F(\xi_0))_t \cos(\omega t + \Phi) dt &= \omega d \int_0^{2\pi/\omega} F(\xi_0) \sin(\omega t + \Phi) dt \\ &= -\pi \frac{A^3}{2} - \frac{\pi}{3} (1 - 6l_0 + 6l_0^2) A \\ &= \pi [(2A_s - (\sigma_- + (\sigma_+ - \sigma_-)l_0) A)] \end{aligned}$$

so that

$$A_s = -\frac{A^3}{4} - \left(\frac{1}{6} - l_0 + l_0^2 + \frac{(\sigma_- + (\sigma_+ - \sigma_-)l_0)}{2} \right) A. \quad (2.37)$$

Proof of Lemma 2.2.2. Define

$$l_i = \frac{x_{2i} - x_{2i-1}}{2}, \quad i = 1 \dots K \quad (2.38)$$

and define a symmetric unit box of size $2l$ to be

$$B(x;l) = \frac{1}{2} (H(x-l) + H(l-x)) = \begin{cases} 1 & \text{if } |x| < l \\ 0 & \text{if } |x| > l \end{cases}$$

(where H is the Heaviside function) so that we may write $h(x)$ as

$$h(x) = c + d \sum_{j=1}^{n/2} B(x - m_j, l_j), \quad \text{where } d = h_+ - h_-, \quad c = h_-. \quad (2.39)$$

We perform multiple scales analysis. Introduce a slow-time scale

$$s = \varepsilon t, \quad w = W(x, t, s), \quad \xi_j = \xi_j(t, s)$$

and expand

$$W(x, t) = W_0 + W_1 \varepsilon + W_2 \varepsilon^2 \dots$$

and

$$x_j = \xi_j + \varepsilon \eta_j + \dots$$

Expanding h to two orders, we have

$$h(x) = h_0(x) + \varepsilon h_1(x)$$

where h_0 is as given by (2.39) but with ξ_j replaced by ξ_{j0} , and

$$h_1(x) = \sum (-1)^j d \eta_j \delta(x - \xi_j)$$

where δ is the delta function. We therefore obtain

$$W_{0xx} = 0 \quad (2.40)$$

$$W_{1xx} = W_{0t} + h_0(x) \quad (2.41)$$

$$W_{2xx} = W_{1t} + W_{0s} + h_1(x) - \sigma W_0 \quad (2.42)$$

Similarly, expanding (2.15c) we obtain

$$\xi_{jt} = (-1)^j W_0(\xi_j, t, s) \quad (2.43)$$

$$\eta_{jt} + \xi_{js} = (-1)^j \eta_j W_{0x}(\xi_j, t, s) + (-1)^j W_1(\xi_j, t, s). \quad (2.44)$$

From (2.40) and periodicity, W_0 is independent of x :

$$W_0(x, t, s) = W_0(t, s)$$

so that (2.43, 2.44) becomes

$$\xi_{jt} = (-1)^j W_0(t, s); \quad \eta_{jt} + \xi_{js} = (-1)^j W_1(\xi_j, t, s). \quad (2.45)$$

Integrating (2.26) assuming periodic b.c. we get

$$W_{0t} = -\frac{1}{n} \int_0^n h_0(x) dx = -c - \frac{d}{n} \sum_{j=1}^n (-1)^j \xi_j. \quad (2.46)$$

This suggests that we define a new variable

$$Y = c + \frac{d}{L} \sum_{j=1}^n (-1)^j \xi_j.$$

From (2.45) and (2.46) we then obtain

$$Y_t = \omega^2 W_0; \quad W_{0t} = -Y \quad \text{where } \omega := \sqrt{d}.$$

From this we obtain

$$W_0 = A(s) \omega \cos(\omega t + \Phi(s)); \quad Y = A(s) \omega^2 \sin(\omega t + \Phi(s))$$

We can therefore write

$$\xi_j = (-1)^j A(s) \sin(\omega t + \Phi(s)) + B_j(s)$$

with an additional algebraic constraint

$$0 = c + \frac{d}{L} \sum_{j=1}^n (-1)^j B_j.$$

Next let's compute W_1 . We have

$$W_{1xx} = h_0 - \frac{1}{L} \int_0^L h_0, \quad W_1 \text{ periodic on } [0, L] \quad (2.47)$$

Define $\hat{F}(x; l, L)$ to be the unique periodic solution to the equation

$$\hat{F}_{xx} = B(x, l) - \frac{1}{L} \int_{-L/2}^{L/2} B(x, l) dx \quad \text{inside } [-L/2, L/2];$$

$$\int_{-L/2}^{L/2} \hat{F}(x) dx = 0 \quad \text{and } \hat{F} \text{ is periodic on } [-L/2, L/2].$$

Direct computations show that

$$\hat{F}(x; l, L) = \begin{cases} -\frac{1}{6} \frac{l}{L} (L-l)(L-2l) + \left(\frac{1}{2} - \frac{l}{L}\right)x^2, & |x| < l \\ -\frac{1}{6} \frac{l}{L} (L-l)(L-2l) + \left(-\frac{l}{L}x^2 + l|x| - \frac{l^2}{2}\right), & l < |x| < \frac{L}{2} \\ \hat{F}(\text{mod}(x + \frac{L}{2}, L) - \frac{L}{2}, l, L) & \text{otherwise} \end{cases} . \quad (2.48)$$

Next define

$$F(x; \xi_1 \dots \xi_n) = \sum_{j=1}^{n/2} \hat{F}(x - m_j, l_j, L) \quad (2.49)$$

so that

$$W_1 = dF(x) + R(t, s)$$

and

$$\eta_{jt} + \xi_{js} = (-1)^j (dF(x) + R(t, s)) .$$

First, assume $n = 4$. We expand (with a slight abuse of notation)

$$\begin{aligned} m_j &= m_j + \varepsilon M_j + \dots \\ l_j &= l_j + \varepsilon \Lambda_j + \dots \end{aligned}$$

Then

$$\begin{aligned} m_{1s} + M_{1t} &= \frac{d}{2} [F(\xi_2) - F(\xi_1)] ; \\ m_{2s} + M_{2t} &= \frac{d}{2} [F(\xi_4) - F(\xi_3)] . \end{aligned}$$

We now explicitly compute these expressions. Recall that

$$\begin{aligned} \xi_1 &= m_1 - l_1; & \xi_2 &= m_1 + l_1 \\ \xi_3 &= m_2 + l_2; & \xi_4 &= m_2 - l_2 \end{aligned}$$

and we compute

$$\begin{aligned} F(\xi_1) &= \hat{F}(-l_1, l_1, 4) + \hat{F}(m_1 - m_2 - l_1, l_2, 4) \\ &= \hat{F}(l_1, l_1, 4) + \hat{F}(m_2 - m_1 + l_1, l_2, 4) \\ F(\xi_2) &= \hat{F}(-l_1, l_1, 4) + \hat{F}(m_1 - m_2 + l_1, l_2, 4) \\ &= \hat{F}(l_1, l_1, 4) + \hat{F}(m_2 - m_1 - l_1, l_2, 4) \end{aligned}$$

From (2.48), note that

$$\hat{F}(x - a, l, L) - \hat{F}(x + a, l, L) = la \left(2 - \frac{4}{L}x \right) \quad \text{provided that } l < x \pm a < L,$$

from which it follows that

$$F(\xi_2) - F(\xi_1) = l_2 l_1 (m_2 - m_1 - 2).$$

Similarly,

$$F(\xi_3) = \hat{F}(m_2 - m_1 - l_2, l_1, 4) + \hat{F}(l_2, l_2, 4)$$

$$F(\xi_4) = \hat{F}(m_2 - m_1 + l_2, l_1, 4) + \hat{F}(l_2, l_2, 4)$$

so that

$$F(\xi_4) - F(\xi_3) = l_1 l_2 (2 - (m_2 - m_1)).$$

Change variables,

$$m_1 = 1 + y_1; \quad m_2 = 3 + y_2$$

so that

$$y_{1s} + M'_{1t} = \frac{d}{2} l_2 l_1 (y_2 - y_1);$$

$$y_{2s} + M'_{2t} = \frac{d}{2} l_1 l_2 (y_1 - y_2).$$

More generally, for $n = 2K$ interfaces, we change variables $m_j = 2j - 1 + y_j$, $j = 1 \dots K$ to obtain:

$$\begin{pmatrix} y_{1s} + M'_{1t} \\ y_{2s} + M'_{2t} \\ \dots \\ y_{Ks} + M'_{Kt} \end{pmatrix} = \frac{d}{K} M \begin{pmatrix} y_1 \\ y_2 \\ \dots \\ y_K \end{pmatrix},$$

$$M = \begin{pmatrix} -(l_1 l_2 + l_1 l_3 + \dots l_1 l_K) & l_1 l_2 & \dots & l_1 l_K \\ l_2 l_1 & -(l_2 l_1 + l_2 l_3 + \dots l_2 l_K) & \dots & l_2 l_K \\ \vdots & & & \vdots \\ l_K l_1 & \dots & l_K l_{K-1} & -(l_K l_1 + l_K l_3 + \dots l_K l_{K-1}) \end{pmatrix}.$$

Integrating each equation from 0 to $2\pi/\omega$ this yields

$$\begin{pmatrix} y_{1s} \\ y_{2s} \\ \dots \\ y_{Ks} \end{pmatrix} = \tilde{M}(s) \begin{pmatrix} y_1 \\ y_2 \\ \dots \\ y_K \end{pmatrix}$$

where $\tilde{M}_{ij}(s) = \frac{1}{2\pi/\omega} \frac{d}{K} \int_0^{2\pi/\omega} M_{ij}(s, t) dt$. Note that assuming $l_j > 0$ for $j = 1 \dots K$, each off-diagonal entry of \tilde{M} is positive. It follows by Lemma 2.2.4 below that $y_j \rightarrow \bar{y}$ as $t \rightarrow \infty$, where $\bar{y} = \frac{1}{K} \sum_j^K y_j$. This shows the formula (2.17) of lemma 2.2.2. To show formula (2.18), apply exactly the same argument after shifting all of the indices by one (so that x_1 becomes x_2 , x_2 becomes x_3 ... and x_n becomes x_1). ■

It remains to show the following lemma.

Lemma 2.2.4 *Let $A(t)$ be an $K \times K$ matrix with the following properties:*

- (a) *There exists a constant m such that $A_{ij}(t) \geq m$ for all $t \geq 0$ and for all off-diagonal entries $i \neq j$;*
- (b) *A is symmetric;*
- (c) *$A_{ii}(t) = -\sum_{j \neq i} A_{ij}(t)$.*

Suppose that y solves

$$y'(t) = A(t)y(t). \tag{2.50}$$

Then $y(t) \rightarrow \bar{y}\mathbf{1}$ as $t \rightarrow \infty$, where \bar{y} is the average $\bar{y} = \frac{1}{K} \sum_{j=1}^K y_j(0)$, and $\mathbf{1} = (1, 1, \dots, 1)^T$. More precisely, there there exists a constant C such that

$$|y(t) - \bar{y}\mathbf{1}| \leq Ce^{-mKt} \text{ for all } t \geq 0 \tag{2.51}$$

Proof. First, note that that $y(t) = c\mathbf{1}$ is a solution to (2.50) for any constant c , since A admits an eigenvalue of zero whose corresponding eigenvector is $\mathbf{1}$. Let $z(t) = y(t) - \bar{y}\mathbf{1}$ where $\bar{y} = \frac{1}{K} \sum_{j=1}^K y_j(0)$. Then z also satisfies $z' = Az$ with $\sum z_i = 0$. Multiply both sides by z^T on the left to obtain:

$$(|z|^2)' = 2z^T Az.$$

Next we claim that $z^T A z \leq -mK |z|^2$. To see this we have

$$\begin{aligned}
z^T A z &= -\frac{1}{2} \sum_i \sum_j A_{ij} (z_j - z_i)^2 \\
&\leq -\frac{m}{2} \sum_i \sum_j (z_j - z_i)^2 \\
&= -\frac{m}{2} \sum_i \sum_j (z_j^2 + z_i^2 - 2z_i z_j) \\
&= -\frac{m}{2} \left[2K \sum_i z_i^2 - 2 \sum_i z_i \left(\sum_j z_j \right) \right] \\
&= -mK |z|^2
\end{aligned}$$

so that $(|z|^2)' \leq -2mK |z|^2$. By Gronwall's inequality, it follows that $|z|^2 \leq C e^{-2mKt}$ which shows (2.51). ■

2.3 Dynamics of $2K$ Interfaces

Following the proof of the Lemma 2.2.2, we start from the following reduced system:

$$W_0 = A(s) \omega \cos(\omega t + \Phi(s)) \quad (2.52)$$

$$Y = A(s) \omega^2 \sin(\omega t + \Phi(s)) \quad (2.53)$$

$$\xi_j = (-1)^j A(s) \sin(\omega t + \Phi(s)) + B_j(s) \quad (2.54)$$

$$W_1 = dF(x) + R(t, s) \quad (2.55)$$

$$\eta_{jt} + \xi_{js} = (-1)^j (dF(\xi_j) + R(t, s)) \quad (2.56)$$

$$2K (R_t + W_{0s}) - W_0 \int_0^{2K} \sigma(x) dx + \sum (-1)^j d\eta_j = 0 \quad (2.57)$$

Define

$$Y_1 = \frac{\sum_{j=1}^{2K} (-1)^j \eta_j}{2K}.$$

Then Y_1 satisfies

$$Y_{1t} + \frac{\sum (-1)^j \xi_{js}}{2K} = \frac{d \sum_{j=1}^{2K} F(\xi_j)}{2K} + R(s, t). \quad (2.58)$$

Notice that $Y = c + \frac{d}{2K} \sum (-1)^j \xi_j$, which implies $\frac{\sum (-1)^j \xi_{js}}{2K} = \frac{Y_s}{d}$, thus

$$Y_{1t} + \frac{Y_s}{d} = \frac{d \sum_{j=1}^{2K} F(\xi_j)}{2K} + R(s, t) \quad (2.59)$$

and

$$\frac{\int_0^{2K} \sigma(x) dx}{2K} = (\sigma^+ - \sigma^-) \frac{\sum_1^{2K} (-1)^j \xi_j}{2K} + \sigma^- = (\sigma^+ - \sigma^-) \frac{Y - c}{d} + \sigma^- \quad (2.60)$$

Taking the derivative of (2.59) and combining it with (2.57), we obtain:

$$Y_{1tt} + \omega^2 Y_1 = \frac{d \sum_{j=1}^{2K} F_x(\xi_j) \xi_{jt}}{2K} - \frac{Y_{st}}{d} - W_{0s} + \frac{W_0 \int_0^{2K} \sigma(x) dx}{2K} \quad (2.61)$$

and also from (2.56), we obtain

$$R(t, s) = Y_{1t} + \frac{Y_s}{d} - \frac{d \sum_{j=1}^{2K} F(\xi_j)}{2K}.$$

Plugging it back into (2.56), we obtain

$$\eta_{jt} + \xi_{js} = (-1)^j \left(dF(\xi_j) + Y_{1t} + \frac{Y_s}{d} - \frac{d \sum_{j=1}^{2K} F(\xi_j)}{2K} \right). \quad (2.62)$$

Multiplying both sides of (2.61) by $\sin(\omega t + \Phi)$ and integrating on $t = 0 \dots 2\pi/\omega$ we obtain $A\Phi_s = 0$. Similarly, multiplying (2.61) by $\cos(\omega t + \Phi)$, we obtain

$$\int_0^{2\pi/\omega} \left(\frac{d \sum_{j=1}^{2K} F_x(\xi_j) \xi_{jt}}{2K} - \frac{Y_{st}}{d} - W_{0s} + \frac{W_0 \int_0^{2K} \sigma(x) dx}{2K} \right) \cos(\omega t + \Phi) = 0 \quad (2.63)$$

Integrating (2.62) on $t = 0 \dots 2\pi/\omega$ we obtain

$$B_{js} = (-1)^j \int_0^{2\pi/\omega} \left(dF(\xi_j) + \frac{Y_s}{d} - \frac{d \sum_{j=1}^{2K} F(\xi_j)}{2K} \right) \quad (2.64)$$

Now we have the reduced ODE systems to describe the evolution of the envelope:

$$\left\{ \begin{array}{l} W_0 = A(s) \omega \cos(\omega t + \Phi(s)) \\ Y = A(s) \omega^2 \sin(\omega t + \Phi(s)) \\ \xi_j = (-1)^j A(s) \sin(\omega t + \Phi(s)) + B_j(s) \\ \int_0^{2\pi/\omega} \left(\frac{d \sum_{j=1}^{2K} F_x(\xi_j) \xi_{jt}}{2K} - \frac{Y_{st}}{d} - W_{0s} + \left(\frac{(\sigma^+ - \sigma^-)(Y - c)}{d} + \sigma^- \right) W_0 \right) \cos(\omega t + \Phi) = 0 \\ B_{js} = (-1)^j \int_0^{2\pi/\omega} \left(dF(\xi_j) + \frac{Y_s}{d} - \frac{d \sum_{j=1}^{2K} F(\xi_j)}{2K} \right) \\ 0 = c + \frac{d}{2K} \sum_{j=1}^{2K} (-1)^j B_j \end{array} \right. \quad (2.65)$$

We used Maple to evaluate these integrals for the particular case of four interfaces, resulting in a set of ODE's for B_j and A . The right-hand side of each of these equations involves a cubic polynomial in B_j and A with over 40 terms. These ODE's were then integrated numerically. The resulting numerical solution is shown using dotted lines in Figure 2.1.

2.4 Discussion

In this chapter we established that, the behaviour of n interfaces for the two-component near-shadow system (2.1) on the domain of size n is fully described by a single interface on the domain of size one. In particular, n interfaces are stable if and only if a single interface is. In fact, one of the following three scenarios give a complete list of possible behaviours:

1. Some interfaces eventually cross each other, leading to annihilation of the two interfaces (Fig 2(c)).
2. $2K$ interfaces eventually reach a steady state (Fig 2(a)).
3. $2K$ interfaces oscillate indefinitely. The long-time dynamics consist of K “breathers” (see Fig 2(b)) that oscillate synchronously (in-phase).

Unlike some other literature e.g. [36, 98] which shows the presence of oscillations as a result of a Hopf bifurcation of the ground state, our results are more “global” as they do not rely on linearization around the steady state. For instance, our results hold even far from the Hopf bifurcation point. In particular, it shows that even if both in-phase and out-of-phase modes become linearly unstable, the solution with two or more interfaces will converge to the in-phase mode. The situation can be much richer if D is not assumed to be large in (2.1) [36], or for systems consisting of more than two equations, such as two competing species mediated by a predator [99], or a system with one activator and two inhibitors [39]. In [36], both in-phase as well as out-of-phase oscillations of two interfaces were observed and analysed for a two-component system with piece-wise linear nonlinearities, and with $D = O(1)$. Out-of-phase oscillations were found when the two interfaces were close to each-other. In [39], in addition to synchronous and asynchronous oscillations, the authors found regimes where chaotic oscillations of two interfaces was observed. An interesting open question we would work on is whether the multiple-scales type methods can be applied to the three-component system in some sub-regime, and if so, what kind of envelope equations can be. Figure 2.2 shows the wiggling behaviour of 2 interfaces in the following cubic model with 3

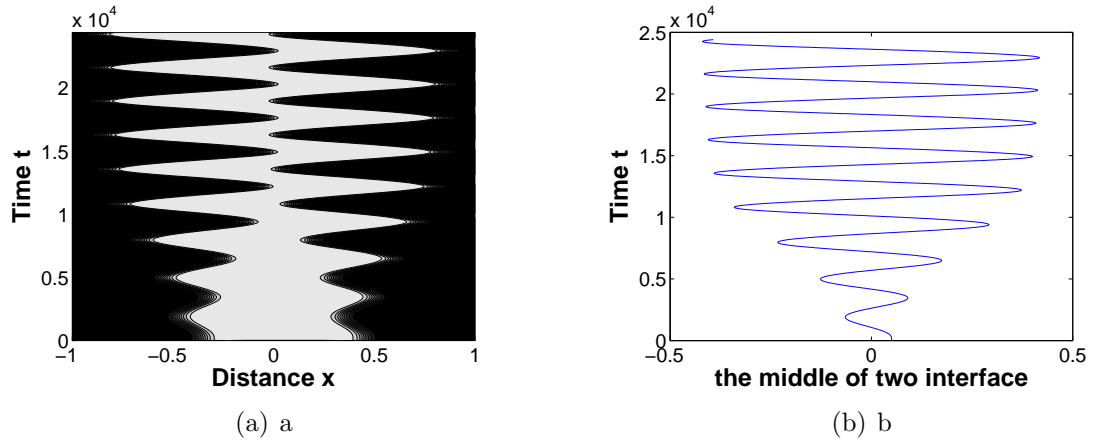


Figure 2.2: (a) cubic model with three components, starting with $u = \tanh(\frac{(x+0.3)}{\varepsilon}) - \tanh(\frac{(x-0.4)}{\varepsilon}) - 1$. Time evolution of u is shown. The parameter values are $\varepsilon = 0.01$, $D = 10$, $\tau = 16000$. The domain size is 2 with Neumann boundary condition for both u and w . (b) The middle point of 2 interfaces

components.

$$\begin{cases} u_t = \varepsilon^2 u_{xx} + 2(u - u^3) - v - w \\ \tau Dv_t = Dv_{xx} + u \\ w = \int_{-1}^1 u(x, t) dx \end{cases} \quad (2.66)$$

Chapter 3

Moving and Jumping Spot in a Two Dimensional Reaction-diffusion Model

The results in this chapter have appeared in [20]. We will use the following scaling of the Schankenberg model

$$v_t = \varepsilon^2 \Delta v - v + v^2 u, \quad \tau u_t = \Delta u + A - \frac{v^2 u}{\varepsilon^2} \quad \text{inside } \Omega \subset \mathbb{R}^2; \quad (3.1)$$

subjected to the Neumann Boundary condition $\partial_n v = \partial_n u = 0$ on $\partial\Omega$. Throughout this chapter, we assume Ω to be a unit disk,

$$\Omega \text{ is a unit disk; } \Omega = \{x \in \mathbb{R}^2 : |x| < 1\}, \quad (3.2)$$

although some of our results can be extended to more general domains.

Here, $\varepsilon \ll 1$, $A > 0$ and $\tau > 0$, represent diffusivity, the feed-rate and the reaction-time constant respectively. The equations model the following process: the fast-diffusing substrate u is consumed by a slowly diffusing activator v , which decays in time. The substrate is being pumped into the system at a constant rate, represented by parameter A . The reaction kinetics for u and v occur at different scales (depending on the choice of τ). Of particular interest to us will be the regime where τ is very large, so that u reacts much slower than v . As we will show, the oscillatory instabilities (both for spike height and positions) are triggered when τ is very large.

In this chapter we consider the effect of increasing the parameter τ on a single spot at the center of the unit disk. The associated linearized eigenvalue problem has eigenfunctions of the form $\phi(r)e^{im\theta}$ in the polar coordinates. Due to underlying translational invariance, the eigenvalues corresponding to mode $m = \pm 1$ are asymptotically small as $\varepsilon \rightarrow 0$ and their instability induces a slow (possibly periodic) motion of the spot. We refer to these eigenvalues as *small eigenvalues*. All other eigenvalues are referred to as *large eigenvalues*. The mode $m = 0$ corresponds to purely radial perturbations and its instability can induce spike oscillation or collapse, whereas the instability with respect

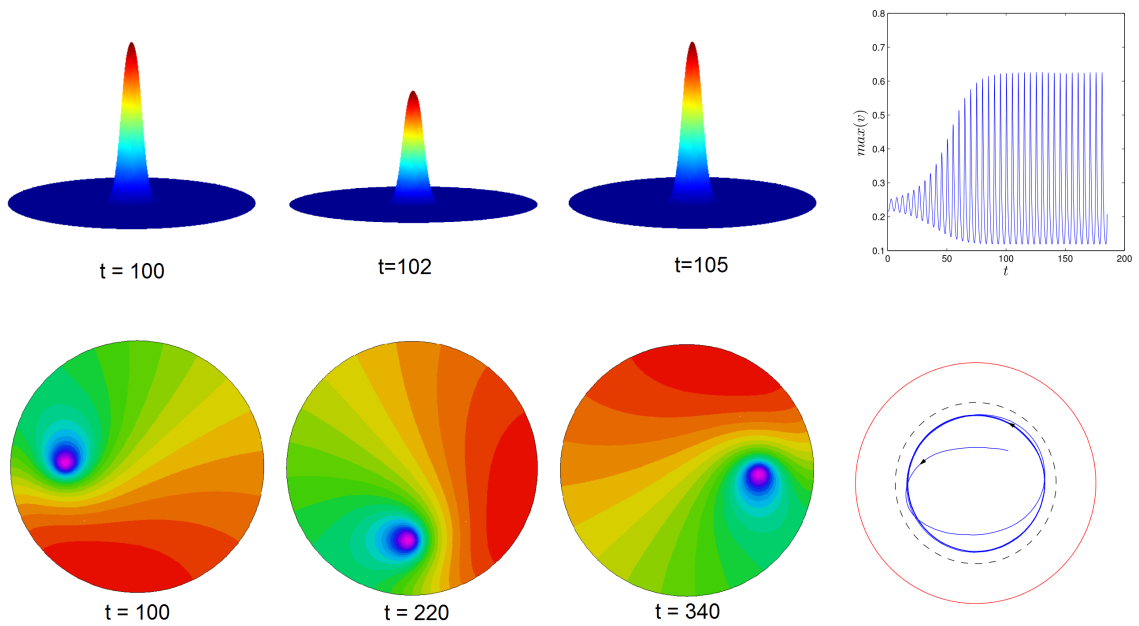


Figure 3.1: Two types of dynamics of a single spike solution of the Schnakenberg model. Top row: height oscillations on $O(1)$ timescale. Three snapshots of $v(x, t)$ are shown at times as indicated. Parameters are $\varepsilon = 0.03$, $A = 1$, $\tau = 0.07$. Top right shows the height of the spike as a function of time. The spike remains at the center of the disk. Bottom row: periodic motion of the spot on a slow timescale. Three snapshots of $u(x, t)$ are shown. Bottom right shows the trajectory of the spot center. Parameters are $\varepsilon = 0.02$, $A = 8$, $\tau = 0.15/\varepsilon^2$. Dashed line shows the asymptotic prediction for the spot trajectory (Proposition 3.7.1)

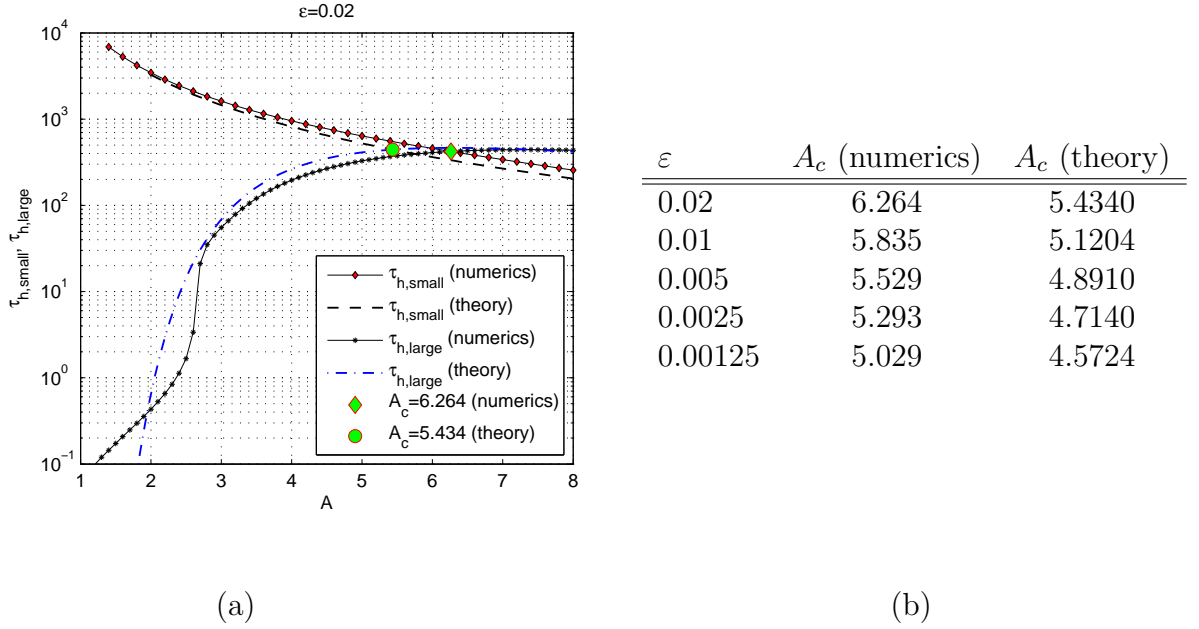


Figure 3.2: (a) Hopf bifurcations values for height and position oscillations ($\tau_{h,large}$ and $\tau_{h,small}$, respectively), as a function of A , and with $\varepsilon = 0.02$. Theoretical predictions given by Propositions 3.3.1 and 3.4.1 are also shown. The intersection of $\tau_{h,large}$ and $\tau_{h,small}$ is denoted by A_c . (b) Comparison between the asymptotic value of A_c given by (3.3) and the numerically computed value for several small ε .

to mode $m = 2$ eigenvalues triggers self-replication [47, 50, 53, 100]. Here, we only concentrate on modes $m = 0, 1$ since τ does not appear to trigger instability of the higher modes.

Two different types of instabilities can be triggered when τ is sufficiently increased as illustrated in Figure 3.1: either large or small eigenvalues can undergo a Hopf bifurcation. The former instability triggers height oscillations, whereas the latter triggers slow translational instabilities in spike position, inducing (typically periodic) spike motion. Which one is triggered *first* depends on values of ε and A .

Our main task is to classify precisely for which parameters A and ε does the spike motion (as opposed to height oscillations) occur when τ is increased sufficiently? In §3.6 (Proposition 3.6.1) we give a concise characterisation in terms of the following threshold. Let

$$A_c \sim \frac{6.283}{\sqrt{\log \left\{ \left(\log \frac{1}{\varepsilon} \right) 1.010 - 0.1433 \right\}}}. \quad (3.3)$$

In the limit $\varepsilon \rightarrow 0$, for values of A bigger than A_c , spike motion is observed as τ is sufficiently increased, whereas when $A < A_c$, increasing τ triggers height oscillations. This threshold follows from computing the thresholds $\tau_{h,large}$ and $\tau_{h,small}$, corresponding to the Hopf bifurcation points for small and large eigenvalues, respectively. This is done in §3.3, and §3.4 to obtain

$$\tau_{h,large} \sim \frac{19.929}{A^2 \varepsilon^2} \exp\left(\frac{-39.474}{A^2}\right); \quad \tau_{h,small} \sim \frac{1}{\varepsilon^2 A^2} \frac{19.737}{\log \frac{1}{\varepsilon} - 0.1419} \quad (3.4)$$

in the critical regime $O\left(\frac{1}{\log 1/\varepsilon}\right) \ll A^2 \ll O(1)$. In fact the threshold (3.3) is obtained from (3.4) by simply setting $\tau_{h,large} = \tau_{h,small}$.

The threshold (3.3) has a striking log log scaling. Despite such a slow convergence rate, remarkably it agrees relatively well with numerical experiments even when $\varepsilon = 0.01$ (see Figure 3.2).

In §3.7 we analyse what happens beyond the Hopf bifurcation for small eigenvalues, in the regime $\tau_{h,small} < \tau < \tau_{h,large}$. In this regime, the spot starts to move and there exists time-dependent solutions in a form of a rotating spot. We compute the radius and speed of the rotation in Proposition 3.7.1. By computing the radius of rotation r_0 as a function of τ , we find that $r_0 \rightarrow 0$ as $\tau \rightarrow \tau_{h,small}$ from above. In other words, the rotating spot solution bifurcates from a stationary spot as a result of a Hopf bifurcation. This is illustrated in Figure 3.4. We conclude with numerical experiments demonstrating even more complex spike motion (see Figure 3.5).

3.1 Equilibrium Solution

We start by reviewing the construction of the equilibrium solution to (3.1) using the method of matched asymptotic expansions as was previously done in [50]. At the equilibrium, the steady state satisfies

$$0 = \varepsilon^2 \Delta v - v + uv^2, \quad 0 = \Delta u + A - \frac{uv^2}{\varepsilon^2} \quad (3.5)$$

with Neumann boundary conditions on Ω . We assume that Ω is a unit disk with the spike located at the center. Near the core of the spike, we rescale:

$$v(x) = V(y), \quad u(x) = U(y) \quad , y = \varepsilon^{-1}x \quad (3.6)$$

Then (3.5) becomes

$$\Delta_y V - V + UV^2 = 0, \quad \Delta_y U + A\varepsilon^2 - UV^2 = 0, \quad y \in \mathbb{R}^2.$$

where Δ_y denotes the Laplacian in y . We expand

$$U = U_0 + \varepsilon^2 U_1 + \dots, \quad V = V_0 + \varepsilon^2 V_1 + \dots.$$

To leading order, we look for a radially symmetric solution given by $V_0 = V_0(\rho)$ and $U_0 = U_0(\rho)$, with $\rho = |y|$. It satisfies the following coupled nonlinear radially symmetric “core problem”,

$$\Delta_\rho V_0 - V_0 + U_0 V_0^2 = 0, \quad \Delta_\rho U_0 - U_0 V_0^2 = 0, \quad 0 < \rho < \infty \quad (3.7a)$$

$$V_0 \rightarrow 0, \quad U_0 \sim S \log \rho + \chi(S) \quad \text{as } \rho \rightarrow \infty. \quad (3.7b)$$

The core problem (3.7), was first identified in one dimension in [42]. It is closely related to the phenomenon of self-replicating spots [47, 50, 53].

To determine the source strength S , we integrate the second equation in (3.5) to obtain

$$A\pi = \int_\Omega \frac{uv^2}{\varepsilon^2} dx \sim \int_{\mathbf{R}^2} U_0 V_0^2 dy.$$

On the other hand integrating the second equation in (3.7a) and using the divergence theorem, we obtain

$$2\pi S = \int_{\mathbf{R}^2} U_0 V_0^2 dy$$

so that

$$S = \frac{A}{2}. \quad (3.8)$$

In general, the solution to (3.7a) as well as the function $\chi(S)$ in (3.7b) must be computed numerically. This was done for example in [47, 50, 53]. Figure 3.1(b) shows the function $\chi(S)$. However for small S , equations (3.7a) become weakly coupled since U_0 becomes nearly constant and we may estimate the solution to (3.7a) as follows. Assume that $S \ll 1$ and $U_0(y) \sim U_0$ is constant to leading order in S . Then V_0, U_0 satisfy at leading order,

$$V_0(y) = w(y) \sigma; \quad U_0(y) = 1/\sigma \quad (3.9)$$

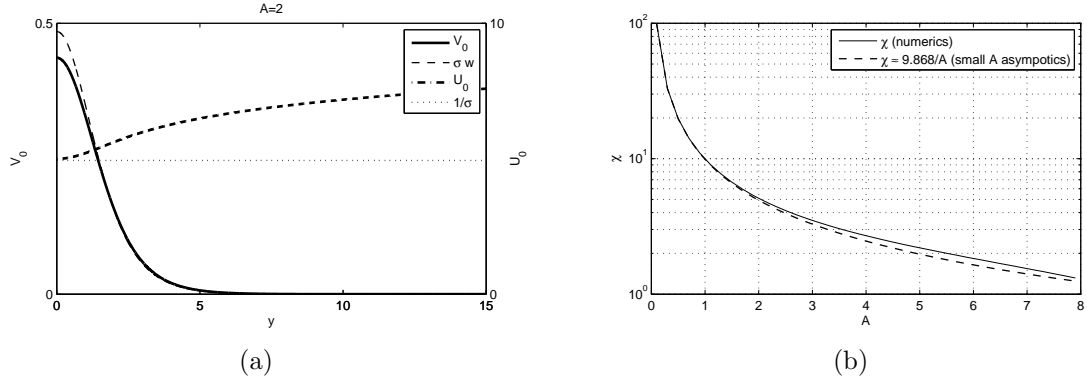


Figure 3.3: (a) Core problem V_0, U_0 and its asymptotics (Proposition 3.1.1). Good comparison between numerics and asymptotics (3.9) is observed even for relatively “large” $A = 2$. (b) A versus χ . Asymptotics denote the regime $A \ll O(1)$ given by $\chi \approx 9.868/A$.

where w is the unique positive ground-state solution to

$$\Delta w - w + w^2 = 0; \quad w \rightarrow 0 \text{ as } |y| \rightarrow \infty; \quad (3.10)$$

and

$$2\pi S \sim \sigma \int w^2 dy; \quad \chi(S) \sim \frac{1}{\sigma}.$$

This yields an asymptotic expression

$$A \sim 2\sigma \int_0^\infty w^2(\rho) \rho d\rho, \quad S \sim \sigma \int_0^\infty w^2(\rho) \rho d\rho, \quad \chi(S) \sim \frac{1}{\sigma}. \quad (3.11)$$

The resulting integral is evaluated numerically in the next section § 3.2. We summarize this construction as follows.

Proposition 3.1.1 *In the limit $0 < \varepsilon \ll 1$, the leading order steady-state solution to (3.5) near the origin satisfies*

$$v(x) \sim V_0(y), \quad u(x) \sim U_0(y) \quad , y = \varepsilon^{-1}x \quad (3.12)$$

where V_0, U_0 satisfy core problem (3.7) and where the constant S is given by (3.8). In the regime $0 < A \ll O(1)$, we have the asymptotics

$$V_0(x) \sim \sigma w(y), \quad y = \varepsilon x \quad (3.13a)$$

$$U_0(x) \sim \frac{1}{\sigma} \quad (3.13b)$$

where $w(y)$ is the unique ground state given by (3.10) and where

$$\sigma = \frac{1}{2 \int_0^\infty w^2 \rho d\rho} A \approx \frac{A}{9.868} \ll 1. \quad (3.13c)$$

Figure 3.1(b) shows the graph of S versus $\chi(S)$, as well as its asymptotic approximation. While the asymptotics are formally valid in the regime $A \ll 1$, they agree well with full numerics even when A is relatively large. For example when $A = 2$, full numerics yield $\chi \approx 5.103$ whereas formula (3.11) yields $\sigma \approx 0.2026$, $\chi \approx 4.934$, for a relative error of only 3%. Note also that this error is independent of ε to leading order. Figure 3.1(a) gives a comparison between $V_0(x)$ and $\sigma w(y)$ with $A = 2$. Excellent agreement is observed. This is in part because the effective small parameter is $\sigma \approx 0.2 \ll 1$ when $A = 2$.

3.2 Some Properties of Function w

We start from the ground state $w(y) = w(\rho)$, $\rho = |y|$. It satisfies

$$w'' + \frac{w'}{\rho} - w + w^2 = 0, \quad w'(0) = 0, \quad w \rightarrow 0 \text{ as } \rho \rightarrow \infty \quad (3.14)$$

Multiplying (3.14) by $w\rho$ and $w'\rho^2$ respectively and integrating over the domain yields

$$-\int_0^\infty w_\rho^2 \rho d\rho - \int_0^\infty w^2 \rho d\rho + \int_0^\infty w^3 \rho d\rho = 0 \quad (3.15)$$

$$\int_0^\infty w^2 \rho d\rho - \frac{2}{3} \int_0^\infty w^3 \rho d\rho = 0 \quad (3.16)$$

Combining these two equations leads to

$$\frac{\int_0^\infty w_\rho^2 \rho d\rho}{\int_0^\infty w^3 \rho d\rho} = \frac{1}{3}, \quad \frac{\int_0^\infty w^2 \rho d\rho}{\int_0^\infty w^3 \rho d\rho} = \frac{2}{3}. \quad (3.17)$$

Finally, we will use the following numerical estimate:

$$\int_0^\infty w^2 \rho d\rho \approx 4.9343$$

It is obtained by solving (3.14) using Matlab's boundary value problem solver `bvp4c`, then using numerical quadrature for the resulting integral.

3.3 Stability: Large (Mode Zero) Eigenvalue

Having constructed the steady state, we now consider its stability. Linearizing around the steady state in (3.1) we write.

$$u(x, t) = v(r) + e^{\lambda t} \phi(x), \quad u(x, t) = u(r) + e^{\lambda t} \psi(x)$$

The linearized system of (3.1) then becomes:

$$\begin{cases} \lambda \phi = \varepsilon^2 \Delta \phi - \phi + v^2 \psi + 2uv\phi & x \in \Omega \\ \tau \lambda \psi = \Delta \psi - \frac{1}{\varepsilon^2} (v^2 \psi + 2uv\phi) & \\ \partial_n \phi = 0 = \partial_n \psi & x \in \partial \Omega \end{cases} \quad (3.18)$$

In the inner region, we expand

$$\phi = e^{im\theta} (\Phi_0(\rho) + \varepsilon^2 \Phi_1(\rho) + \dots) \quad \psi = e^{im\theta} (\Psi_0(\rho) + \varepsilon^2 \Psi_1(\rho) + \dots) \quad (3.19)$$

where $\rho = |y|$ $y = \varepsilon^{-1}x$. Substituting (3.19) into (3.18), then to leading order we obtain the following radially symmetric eigenvalue problem:

$$\begin{aligned} \lambda \Phi_0 &= \Delta_m \Phi_0 - \Phi_0 + V_0^2 \Psi_0 + 2U_0 V_0 \Phi_0 \\ 0 &= \Delta_m \Psi_0 - (V_0^2 \Psi_0 + 2U_0 V_0 \Phi_0) \end{aligned} \quad (3.20)$$

Here $\Delta_m \Phi_0 \equiv \partial_{\rho\rho} \Phi_0 + \rho^{-1} \partial_\rho \Phi_0 - m^2 \rho^{-2} \Phi_0$. and U_0, V_0 are solutions to (3.7).

Because of the decay term in the equation for Φ_0 , we assume that Φ_0 decays exponentially for large $|y|$. On the other hand, the appropriate far-field boundary condition for Ψ_0 depends on whether $m = 0$ or $m \geq 1$.

We begin by considering the mode $m = 0$. In this case the far-field conditions for Ψ_0 exhibits logarithmic growth, $\Psi_0 \sim C \log |y| + B$, $|y| \gg 1$. We can scale the eigenfunction to set $C = 1$, so that Ψ_0 then satisfies

$$\Psi_0 \sim \ln |y| + B, \quad |y| \gg 1. \quad (3.21)$$

By integrating over the equation for Ψ_0 and using the Divergence theorem, this scaling is equivalent to

$$\int_{\mathbb{R}^2} (V_0^2 \Psi_0 + 2U_0 V_0 \Phi_0) = 2\pi. \quad (3.22)$$

The constant B is determined by matching to the outer region. Since v is assumed to decay away from the spike, using (3.22) we have

$$\int_{\Omega} \frac{1}{\varepsilon^2} (v^2 \psi + 2uv\phi) dx \sim 2\pi$$

and the outer problem for ψ is

$$\lambda\tau\psi = \Delta\psi - 2\pi\delta(x) \text{ inside } \Omega; \quad \partial_n\psi = 0 \text{ on } \partial\Omega \quad (3.23)$$

whose solution is given by

$$\psi(x) \sim \frac{K'_0(\sqrt{\tau\lambda})}{I'_0(\sqrt{\tau\lambda})} I_0(\sqrt{\tau\lambda}r) - K_0(\sqrt{\tau\lambda}r), \quad r = |x|. \quad (3.24)$$

Expanding for small r we have

$$\begin{aligned} \psi(x) &\sim \log(r) + \frac{K'_0(\sqrt{\tau\lambda})}{I'_0(\sqrt{\tau\lambda})} - \log(2) + \gamma + \log(\sqrt{\lambda\tau}) \quad \text{as } r \rightarrow 0 \\ &\sim \log(|y|) + \frac{K'_0(\sqrt{\tau\lambda})}{I'_0(\sqrt{\tau\lambda})} + \log\left(\frac{e^\gamma}{2}\sqrt{\varepsilon^2\lambda\tau}\right). \end{aligned} \quad (3.25)$$

Note that the above expansion assumes that $\sqrt{\tau\lambda}\varepsilon \ll 1$. This will be shown to be self-consistent later on. Then matching (3.21) and (3.25), yields

$$B = \frac{K'_0(\sqrt{\tau\lambda})}{I'_0(\sqrt{\tau\lambda})} + \log\left(\frac{e^\gamma}{2}\sqrt{\varepsilon^2\lambda\tau}\right). \quad (3.26)$$

Together with (3.20), this provides a closed-system which determines the eigenvalue λ . We summarize this construction:

Proposition 3.3.1 *In the limit $\varepsilon \rightarrow 0$, the mode-zero eigenvalue λ of the linearized problem (3.18) is asymptotic to the eigenvalue problem (3.20) with $m = 0$ subject to the outer condition (3.21) where B is given by (3.26), as long as $\sqrt{\tau\lambda}\varepsilon \ll 1$.*

We now concentrate on the weakly-coupled regime to $A \ll 1$ given by (3.13c). Substitute the steady-state expansion (3.13) into (3.20) to obtain to leading order

$$\begin{aligned} \lambda\Phi_0 &= \Delta_0\Phi_0 - \Phi_0 + 2w\Phi_0 + w^2\sigma^2\Psi_0 \\ 0 &= \Delta_0\Psi_0 - (w^2\sigma^2\Psi_0 + 2w\Phi_0). \end{aligned} \quad (3.27)$$

Rescale $\Phi_0 = \sigma^2\hat{\Phi}_0$ and drop the hat to obtain

$$\begin{aligned} \lambda\Phi_0 &= \Delta_0\Phi_0 - \Phi_0 + 2w\Phi_0 + w^2\Psi_0 \\ 0 &= \Delta_0\Psi_0 - \sigma^2(w^2\Psi_0 + 2w\Phi_0). \end{aligned} \quad (3.28)$$

whereas (3.22) becomes

$$\int_{\mathbb{R}^2} (w^2 \Psi_0 + 2w \Phi_0) dy = 2\pi \sigma^{-2}. \quad (3.29)$$

In addition, we will assume à-priori that $|\tau\lambda| \gg 1$ (this self-consistency of this assumption will be verified at the end). Under this assumption, using the large-argument expansion of the Bessel functions, the term $\frac{K'_0(\sqrt{\tau\lambda})}{I'_0(\sqrt{\tau\lambda})}$ is exponentially small so that

$$B \sim \log \left(\frac{e^\gamma}{2} \sqrt{\varepsilon^2 \lambda \tau} \right).$$

Furthermore suppose $B \gg 1$. Then we may estimate Ψ_0 by a constant,

$$\Psi_0 \sim \log \left(\frac{e^\gamma}{2} \sqrt{\varepsilon^2 \lambda \tau} \right).$$

We further rescale $\Phi_0(y) = -\Psi_0 \Phi(y)$ which leads to the reduced problem

$$(L_0 - \lambda)\Phi = w^2; \quad (3.30a)$$

$$-2 \int w \Phi + \int w^2 dx = \frac{2\pi \sigma^{-2}}{\log \left(\frac{e^\gamma}{2} \sqrt{\varepsilon^2 \lambda \tau} \right)}. \quad (3.30b)$$

where the operator L_0 is defined by

$$L_0 \Phi := \Delta_0 \Phi - \Phi + 2w \Phi. \quad (3.31)$$

One of the key properties of the operator L_0 is that

$$L_0 w = w^2$$

as can be readily verified using (3.10). This suggests that we seek a Hopf bifurcation point of (3.30) assuming λ is small. We therefore expand in λ

$$\Phi = w + \lambda \Phi_1, \quad \lambda \ll 1 \quad (3.32)$$

to obtain

$$\Phi_1 = L_0^{-1}(w).$$

Define

$$\tau_0 := \left(\frac{e^\gamma}{2} \right)^{-2} \varepsilon^2 \tau \quad (3.33)$$

and assume that λ is purely imaginary,

$$\lambda = i\lambda_I; \quad \lambda_I \ll 1.$$

Then (3.30) becomes

$$-2\lambda_I i \int w L_0^{-1}(w) dy - \int w^2 dy = \frac{2\pi\sigma^{-2}}{\log(\sqrt{i\lambda_I\tau_0})}. \quad (3.34)$$

Using the identity

$$L_0^{-1}w = w + \frac{1}{2}y \cdot \nabla w = w + \frac{1}{2}\rho w'(\rho)$$

and integrating by parts, we obtain

$$2 \int w L_0^{-1}(w) dy = \int w^2 dy \quad (3.35)$$

so that (3.34) becomes

$$\log(\sqrt{i\lambda_I\tau_0}) = \frac{-2\pi\sigma^{-2}}{\int w^2 dy} \frac{1}{\lambda_I i + 1} = \frac{2 \int w^2 dy}{A^2\pi} \left(\frac{i\lambda_I - 1}{\lambda_I^2 + 1} \right). \quad (3.36)$$

Equating real and imaginary parts we obtain

$$\begin{cases} \frac{1}{2} \log(\lambda_I\tau_0) = \frac{2 \int w^2 dy}{A^2\pi} \frac{-1}{\lambda_I^2 + 1} \\ \frac{\pi}{4} = \frac{2 \int w^2 dy}{A^2\pi} \frac{\lambda_I}{\lambda_I^2 + 1} \end{cases} \quad (3.37)$$

These equations yields, to leading order in $A \ll 1$,

$$\begin{cases} \lambda_I \sim \frac{\pi^2 A^2}{8 \int w^2 dy} \\ \tau_0 = \exp\left(\frac{-4 \int w^2 dy}{A^2\pi}\right) \frac{8 \int w^2 dy}{\pi^2 A^2} \end{cases}, \quad A \ll 1 \quad (3.38)$$

Using (3.33) we finally obtain the critical value of $\tau = \tau_h$ at the Hopf bifurcation point for large eigenvalue:

$$\tau_h = \frac{1}{A^2\epsilon^2} \exp\left(\frac{-4 \int w^2 dy}{A^2\pi}\right) \frac{2e^{2\gamma} \int w^2 dy}{\pi^2}.$$

We made three assumptions in this derivation: (i) $\lambda\tau \gg 1$; (ii) $\epsilon^2\tau\lambda \ll 1$ and (iii) $\lambda \ll 1$. Assumptions (ii) and (iii) are satisfied since $A \ll 1$ (see (3.38), (3.33)). On the other hand, assumption (i) is equivalent to $\exp\left(\frac{-4 \int w^2 dy}{A^2\pi}\right) \gg \epsilon^2$, or $A^2 \gg O\left(\frac{1}{\log \epsilon^{-1}}\right)$.

In summary, we have:

Proposition 3.3.2 *Suppose that*

$$\frac{1}{\log 1/\varepsilon} \ll A^2 \ll 1.$$

Then the spike solution from Proposition 3.1.1 undergoes a Hopf bifurcation as τ is increased past $\tau = \tau_{h,\text{large}}$ where

$$\tau_{h,\text{large}} \sim \frac{1}{A^2 \varepsilon^2} a_0 \exp\left(\frac{-a_1}{A^2}\right) \quad (3.39)$$

and

$$a_0 = \frac{4e^{2\gamma} \int_0^\infty w^2(\rho) \rho d\rho}{\pi} \approx 19.929, \quad a_1 = 8 \int_0^\infty w^2(\rho) \rho d\rho \approx 39.474.$$

3.4 Small Eigenvalues

We study the Hopf bifurcation in the small eigenvalue problem corresponding to the mode $m = 1$ in (3.20). A posteriori analysis reveals that the relevant scaling is

$$\lambda = \lambda_0 \varepsilon^2 \quad \tau = \tau_0 \varepsilon^{-2}$$

where λ_0 and τ_0 are $O(1)$ with respect to ε . The leading order eigenvalue problem is

$$0 = \Phi_0'' + \frac{1}{\rho} \Phi_0' - \frac{1}{\rho^2} \Phi_0 - \Phi_0 + V_0^2 \Psi_0 + 2U_0 V_0 \Phi_0 \quad (3.40a)$$

$$0 = \Psi_0'' + \frac{1}{\rho} \Psi_0' - \frac{1}{\rho^2} \Psi_0 - (V_0^2 \Psi_0 + 2U_0 V_0 \Phi_0) \quad (3.40b)$$

where $\rho = |y| = |x|/\varepsilon$. The solution to (3.40) is given by:

$$\Phi_0 = \frac{C}{S} V_{0\rho} \quad \Psi_0 = \frac{C}{S} U_{0\rho}. \quad (3.41)$$

and satisfies the far field condition given by

$$\Phi_0 \rightarrow 0, \quad \Psi_0 \sim \frac{C}{\rho}, \quad \text{as } \rho \rightarrow \infty. \quad (3.42)$$

The constant C will be obtained through matching to the outer solution. The outer problem for ψ is

$$\tau_0 \lambda \psi = \Delta \psi, \quad r \neq 0$$

subject to $\frac{\partial \psi}{\partial r}(1) = 0$ and $\psi \sim \frac{C\varepsilon e^{i\theta}}{r}$ as $r \rightarrow 0$. This yields an explicit solution

$$\psi = C\varepsilon\sqrt{\tau_0\lambda_0} \left(-\frac{K'_1(\sqrt{\tau_0\lambda_0})}{I'_1(\sqrt{\tau_0\lambda_0})} I_1(\sqrt{\tau_0\lambda_0}r) + K_1(\sqrt{\tau_0\lambda_0}r) \right) e^{i\theta}. \quad (3.43)$$

Recall the small-argument expansion for K_1 and I_1 is given by

$$K_1(z) \sim \frac{1}{z} + \frac{1}{2}z(\log z + b_0) + O(z^2 \ln z), \quad \text{where } b_0 = \gamma - \frac{1}{2} - \ln 2. \quad (3.44a)$$

$$I_1(z) \sim \frac{1}{2}z + O(z^3) \quad (3.44b)$$

Writing (3.43) in inner variables $r = \rho\varepsilon$ and using expansions (3.44) we then obtain

$$\begin{aligned} \psi &\sim \left(\frac{C}{\rho} + \varepsilon^2 \frac{1}{2} C \tau_0 \lambda_0 \rho \left\{ \log \left(\sqrt{\tau_0 \lambda_0} \rho \varepsilon \right) - \frac{K'_1(\sqrt{\tau_0 \lambda_0})}{I'_1(\sqrt{\tau_0 \lambda_0})} + b_0 \right\} \right) e^{i\theta} \\ &\sim e^{i\theta} (\Psi_0(\rho) + \varepsilon \Psi_1(\rho)) \end{aligned}$$

The $O(1)$ terms yields the far-field behaviour for $\Psi(\rho)$ given by (3.42). The $O(\varepsilon^2)$ terms yield the far-field behaviour for $\Psi_1(\rho)$,

$$\Psi_1 \sim \frac{1}{2} C \tau_0 \lambda_0 \rho \left\{ \log \rho + \log \left(\sqrt{\tau_0 \lambda_0} \varepsilon \right) - \frac{K'_1(\sqrt{\tau_0 \lambda_0})}{I'_1(\sqrt{\tau_0 \lambda_0})} + b_0 \right\}, \quad \rho \gg 1. \quad (3.45)$$

To determine λ_0 requires an expansion at the next order. The steady state satisfies

$$\Delta V_1 - V_1 + 2U_0 V_0 V_1 + U_1 V_0^2 = 0, \quad (3.46a)$$

$$\Delta U_1 + A - U_1 V_0^2 - 2U_0 V_0 V_1 = 0, \quad (3.46b)$$

and the corresponding eigenvalue problem is

$$\lambda_0 \Phi_0 = \Delta_1 \Phi_1 - \Phi_1 + V_0^2 \Psi_1 + 2U_0 V_0 \Phi_1 + 2(V_0 U_1 + U_0 V_1) \Phi_0 + 2V_0 V_1 \Psi_0 \quad (3.47a)$$

$$\tau_0 \lambda_0 \Psi_0 = \Delta_1 \Psi_1 - (V_0^2 \Psi_1 + 2U_0 V_0 \Phi_1) - 2(V_0 U_1 + U_0 V_1) \Phi_0 - 2V_0 V_1 \Psi_0 \quad (3.47b)$$

subject to the far field condition (3.45).

We express (3.47) in matrix form as

$$\Delta_1 \mathbf{W} + M \mathbf{W} = E \mathbf{f}_1 + \mathbf{f}_2, \quad 0 < \rho < \infty \quad (3.48a)$$

$$\mathbf{W} \sim \begin{pmatrix} 0, \\ C_1 \rho \ln |\rho| + C_2 \rho \end{pmatrix}, \quad \text{as } \rho \rightarrow \infty \quad (3.48b)$$

where:

$$M = \begin{pmatrix} -1 + 2U_0V_0 & V_0^2 \\ -2U_0V_0 & -V_0^2 \end{pmatrix}, \quad E = \begin{pmatrix} -2(U_0V_1 + U_1V_0) & -2V_0V_1 \\ 2(U_0V_1 + U_1V_0) & 2V_0V_1 \end{pmatrix}, \quad (3.48c)$$

$$\mathbf{W} = \begin{pmatrix} \Phi_1 \\ \Psi_1 \end{pmatrix}, \quad \mathbf{f}_1 = \begin{pmatrix} \Phi_0 \\ \Psi_0 \end{pmatrix}, \quad \mathbf{f}_2 = \begin{pmatrix} \lambda_0\Phi_0 \\ \tau_0\lambda_0\Psi_0 \end{pmatrix}, \quad (3.48d)$$

$$C_1 = \frac{1}{2}C\tau_0\lambda_0, \quad C_2 = \frac{1}{2}C\tau_0\lambda_0 \left\{ \log\left(\sqrt{\tau_0\lambda_0}\varepsilon\right) - \frac{K_1'(\sqrt{\tau_0\lambda_0})}{I_1'(\sqrt{\tau_0\lambda_0})} + b_0 \right\}. \quad (3.48e)$$

Let \mathbf{P} be the solution of the adjoint problem,

$$\Delta_1\mathbf{P} + M^t\mathbf{P} = 0 \quad (3.49a)$$

subjected to the far-field behaviour condition

$$\mathbf{P} \sim \begin{pmatrix} 0 \\ \frac{1}{\rho} \end{pmatrix} \quad \text{for } \rho \gg 1. \quad (3.49b)$$

We multiply (3.48a) by $\rho\mathbf{P}^t$ and integrate to obtain

$$\int_0^R \mathbf{P}^t (\Delta_1\mathbf{W} + M \cdot \mathbf{W}) \rho d\rho = \int_0^R \mathbf{P}^t \cdot (E\mathbf{f}_1 + \mathbf{f}_2) \rho d\rho. \quad (3.50)$$

Here, R is a big number which we will take to infinity later. Integrating by parts, the left hand side becomes

$$\int_0^R \mathbf{P}^t (\Delta_1\mathbf{W} + M \cdot \mathbf{W}) \rho d\rho = \left(\mathbf{P}^t \cdot \left(\rho \frac{\partial \mathbf{W}}{\partial \rho} \right) - \left(\rho \frac{\partial \mathbf{P}^t}{\partial \rho} \right) \cdot \mathbf{W} \right)_{\rho=R} \quad (3.51)$$

$$= (2C_1 \ln R + 2C_2 + C_1) \quad (3.52)$$

To calculate the right hand side of (3.50), we introduce $\mathbf{N} = \left(\frac{\partial V_1}{\partial \rho}, \frac{\partial U_1}{\partial \rho} \right)^t$. Upon differentiating the system for V_1 and U_1 with respect to ρ , we obtain

$$\Delta_1\mathbf{N} + M \cdot \mathbf{N} = \begin{pmatrix} -2(U_0V_0)_\rho V_1 - (V_0^2)_\rho U_1 \\ 2(U_0V_0)_\rho V_1 + (V_0^2)_\rho U_1 \end{pmatrix}.$$

The key observation is that

$$E\mathbf{f}_1 = \frac{C}{S} \begin{pmatrix} -2(U_0V_0)_\rho V_1 - (V_0^2)_\rho U_1 \\ 2(U_0V_0)_\rho V_1 + (V_0^2)_\rho U_1 \end{pmatrix} = \frac{C}{S} (\Delta_1\mathbf{N} + M \cdot \mathbf{N})$$

It follows that

$$\begin{aligned} \int_0^R \mathbf{P}^t \cdot (E \cdot \mathbf{f}_1) \rho d\rho &= \frac{C}{S} \int_0^R \mathbf{P}^t \cdot (\Delta_1 \mathbf{N} + M \cdot \mathbf{N}) \rho d\rho \\ &= \frac{C}{S} \left(\mathbf{P}^t \cdot \left(\rho \frac{\partial \mathbf{N}}{\partial \rho} \right) - \left(\rho \frac{\partial \mathbf{P}^t}{\partial \rho} \right) \cdot \mathbf{N} \right) \Big|_{\rho=R} \\ &= -2C. \end{aligned}$$

Next we simplify

$$\int_0^R \mathbf{P}^t \cdot \mathbf{f}_2 \rho d\rho = \int_0^R (P_1 \Phi_0 + \tau_0 P_2 \Psi_0) \lambda_0 \rho d\rho$$

and we further compute

$$\begin{aligned} \int_0^R \tau_0 P_2 \Psi_0 \lambda_0 \rho d\rho &= \frac{C}{S} \tau_0 P_2 U_0 \lambda_0 \rho \Big|_0^R - \frac{C}{S} \int_0^R \tau_0 (P_2 \rho)_\rho U_0 \lambda_0 d\rho \\ &= \frac{C}{S} \tau_0 \lambda_0 (S \log(R) + \chi(S)) - \frac{C}{S} \int_0^R \tau_0 (P_2 \rho)_\rho U_0 \lambda_0 d\rho. \end{aligned}$$

In summary, we obtain that the right hand side of (3.50) simplifies to

$$\begin{aligned} \int_0^R \mathbf{P}^t \cdot (E \mathbf{f}_1 + \mathbf{f}_2) \rho d\rho &= \lambda_0 \int_0^R P_1 \Phi_0 \rho d\rho + C \tau_0 \lambda_0 \log(R) \\ &\quad + \frac{C \tau_0 \lambda_0}{S} \chi(S) - \frac{C}{S} \int_0^R \tau_0 (P_2 \rho)_\rho U_0 \lambda_0 d\rho - 2C. \end{aligned} \quad (3.53)$$

Equating (3.52) and (3.53), note that the $\log R$ terms cancel each other out and after factoring out C , and we finally obtain

$$\frac{\lambda_0 \kappa_1 - \tau_0 \lambda_0 \kappa_2}{S} = \tau_0 \lambda_0 \left(\log \left(\frac{e^\gamma}{2} \sqrt{\tau_0 \lambda_0 \varepsilon} \right) - \frac{K_1'(\sqrt{\tau_0 \lambda_0})}{I_1'(\sqrt{\tau_0 \lambda_0})} \right) + 2 \quad (3.54a)$$

where κ_1 and κ_2 are given by

$$\kappa_1 := \int_0^\infty P_1 V_{0\rho} \rho d\rho, \quad \kappa_2 := \int_0^\infty (P_2 \rho)_\rho [U_0 - \chi(S)] d\rho. \quad (3.54b)$$

Next, we seek a Hopf bifurcation for (3.54). Setting $\lambda_0 = i\lambda_I$ in (3.54a) and equating real and imaginary parts yields $\tau_0 \lambda_I = \omega_c$ where ω_c satisfies

$$\omega_c \operatorname{Im} \left(\log(\sqrt{i\omega_c}) - \frac{K_1'(\sqrt{i\omega_c})}{I_1'(\sqrt{i\omega_c})} \right) - 2 = 0 \quad (3.55a)$$

and

$$\tau_0 = \frac{\kappa_1}{S \operatorname{Re} \left(-\frac{K_1'(\sqrt{i\omega_c})}{I_1'(\sqrt{i\omega_c})} + \log \left(\frac{e^\gamma}{2} \sqrt{i\omega_c \varepsilon} \right) \right) + \kappa_2} \quad (3.55b)$$

A remarkable fact is that the equation (3.55a) is independent of any parameters. Numerical plotting shows that there is a unique solution to (3.55a) given by

$$\omega_c \approx 3.02603687. \quad (3.55c)$$

Expression (3.55b) is further simplified by rewriting

$$\operatorname{Re} \left(-\frac{K_1'(\sqrt{i\omega_c})}{I_1'(\sqrt{i\omega_c})} + \log \left(\frac{e^\gamma}{2} \sqrt{i\omega_c} \varepsilon \right) \right) = \alpha_1 + \log(\varepsilon)$$

where

$$\alpha_1 := \operatorname{Re} \left(-\frac{K_1'(\sqrt{i\omega_c})}{I_1'(\sqrt{i\omega_c})} \right) + \log \left(\frac{e^\gamma}{2} \sqrt{\omega_c} \right) = -0.14623425. \quad (3.56)$$

In general, the constants κ_1, κ_2 must be computed numerically. However asymptotic expansion is available in the intermediate regime, when A is small, and is given in section § 3.5. We summarize.

Proposition 3.4.1 *The translational eigenvalue corresponding to mode $m = 1$ of the steady state in Proposition 3.1.1 undergoes a Hopf bifurcation as τ is increased past $\tau \sim \tau_{h,small}$ where*

$$\tau_{h,small} = \frac{1}{\varepsilon^2} \frac{\kappa_1}{\frac{A}{2} (\log \varepsilon + \alpha_1) + \kappa_2}. \quad (3.57)$$

The constants κ_i are independent of ε (depend only on A) and are given in (3.54b). The constant $\alpha_1 = -0.1462342$ is a universal constant defined through (3.56). In the asymptotic limit $A \ll 1$, the formula (3.57) simplifies to

$$\tau_{h,small} = \frac{1}{\varepsilon^2 A^2} \frac{2\kappa_{10}}{\log \frac{1}{\varepsilon} - \alpha_1 - 2\kappa_{20}}. \quad (3.58)$$

where

$$\kappa_{10} \approx 9.86855; \quad \kappa_{20} \approx 0.1441$$

whose exact value is derived in Appendix 3.5.

Figure 3.2 shows a very good agreement between the full numerical simulations of the eigenvalue problem (3.18) and formula (3.58).

3.5 Estimating κ_1, κ_2 for Small A .

In this section we compute the asymptotic expansion for κ_1, κ_2 given by (3.54b) for small A . In this limit, we recall from (3.9) that $U_0 \sim \chi = \sigma^{-1}$ and $V_0 \sim \sigma w$ where $\sigma = \frac{A}{2 \int_0^\infty w^2 \rho d\rho}$. The adjoint problem (3.49) simplifies to

$$(\partial_{\rho\rho} + \rho^{-1}\partial_\rho - \rho^{-2}) P_1 - P_1 + 2wP_1 - 2wP_2 \sim 0, \quad 0 < \rho < \infty, \quad P_1 \sim 0 \text{ as } \rho \rightarrow \infty \quad (3.59a)$$

$$(\partial_{\rho\rho} + \rho^{-1}\partial_\rho - \rho^{-2}) P_2 + \sigma^2 w^2 (P_1 - P_2) \sim 0, \quad 0 < \rho < \infty, \quad P_2 \sim \rho^{-1}, \text{ as } \rho \rightarrow \infty. \quad (3.59b)$$

The solution to this limiting system is given by

$$P_1 = \sigma^{-2} \left(-\frac{3w_\rho}{\int_0^\infty w^3 s ds} + O(\sigma^2) \right), \quad P_2 = \frac{1}{\rho} \frac{\int_0^\rho w^3 s ds}{\int_0^\infty w^3 s ds} + O(\sigma^2) \quad (3.60)$$

and we then obtain

$$\kappa_1 \sim \frac{-3 \int_0^\infty w_\rho^2 \rho d\rho}{\int_0^\infty w^3 \rho d\rho} \sigma^{-1}, \quad \kappa_2 \sim \frac{1}{\int_0^\infty w^3 \rho d\rho} \int_0^\infty [U_0 - \sigma^{-1}] w^3 \rho d\rho. \quad (3.61)$$

To compute κ_2 further, we let $U_0 - \sigma^{-1} = \sigma \hat{U} + O(\sigma^2)$ where \hat{U} satisfies

$$\Delta \hat{U} = w^2$$

subject to the far-field condition $\hat{U} \sim S \log \rho + 0, \rho \gg 1$. The solution to \hat{U} is given by

$$\hat{U}(\rho) = \int_0^\rho \frac{F(s)}{s} ds - \int_1^\infty \frac{F(s) - F(\infty)}{s} ds - \int_0^1 \frac{F(s)}{s} ds$$

where

$$F(s) = \int_0^s w^2(\rho) \rho d\rho;$$

κ_2 is then given by

$$\kappa_2 \sim \sigma \frac{\int_0^\infty \hat{U} w^3 \rho d\rho}{\int_0^\infty w^3 \rho d\rho}.$$

The integrals $\int_0^\infty \hat{U} w^3 \rho d\rho$ is computed numerically. In summary, we obtain the following expansions for κ_1, κ_2 :

$$\kappa_1 \sim -\frac{1}{A} \kappa_{10}; \quad \kappa_2 \sim A \kappa_{20}$$

where (using (3.17)),

$$\kappa_{10} = 2 \int_0^\infty w^2 \rho d\rho; \quad \kappa_{20} = \frac{\int_0^\infty \hat{U} w^3 \rho d\rho}{2 \int_0^\infty w^2 \rho d\rho \int_0^\infty w^3 \rho d\rho}.$$

The numerical estimates for κ_1 and κ_2 , computed using numerical quadrature, are

$$\kappa_{10} \approx 9.8686; \quad \kappa_{20} \approx 0.1441.$$

3.6 Threshold Crossing

As Figure 3.2 shows, the Hopf curves $\tau_{h,large}$ and $\tau_{h,small}$ intersect as A is increased at some critical value $A = A_c$. Having computed asymptotically the Hopf bifurcations for both small and large eigenvalues, we are finally in position to determine this crossing by equating $\tau_{h,large} = \tau_{h,small}$ (where $\tau_{h,large}$ and $\tau_{h,small}$ are given in Propositions 3.3.2 and 3.4.1, respectively). Solving for A yields

$$A_c \sim \frac{c_1}{\left[\ln\left(c_2 \ln \frac{1}{\varepsilon} + c_3\right)\right]^{1/2}} \quad (3.62)$$

where

$$\begin{aligned} c_1 &= a_1^{1/2} \approx 6.2828; \\ c_2 &= \frac{e^{2\gamma}}{\pi} \approx 1.00975, \\ c_3 &= \frac{(-\alpha_1 - 2\kappa_{20})a_0}{2\kappa_{10}} \approx -0.14334. \end{aligned}$$

From the formulas for $\tau_{h,large}$ and $\tau_{h,small}$, it is clear that if $A < A_c$, the height oscillations are triggered before position oscillations, whereas the opposite is true if $A > A_c$. This is the main result of the paper. We summarize.

Proposition 3.6.1 *Let A_c as given in (3.3) with $\varepsilon \ll 1$. Suppose that $A < A_c$. Then height oscillations are triggered before the position oscillations as τ is increased just past $\tau_{h,large}$. Suppose that $A > A_c$. Then position oscillations are triggered before height oscillations as τ is increased just past $\tau_{h,small}$.*

Note that the derivation required that $O\left(\frac{1}{\log \frac{1}{\varepsilon}}\right) \ll A^2 \ll O(1)$. Both of these conditions are clearly satisfied in the critical regime $A^2 = O(A_c^2) = O\left(\frac{1}{\log(\log \frac{1}{\varepsilon})}\right)$.

Although in theory, the formula for A_c is valid as $\varepsilon \rightarrow 0$, the log-log scaling has a horrible convergence rate. It is then all the more surprising that the formula (3.3) is able to predict the threshold within a reasonable accuracy, even when $\varepsilon = 0.02$. To further validate this result, we computed A_c numerically up to $\varepsilon = O(10^{-3})$. The result is summarized in the table in Figure 3.2. Attempting to compute at such small ε values required the use of a non-uniform grid to compute eigenvalues numerically. We then used a numerical root solver and continuation to adjust A until $\tau_{h,large} = \tau_{h,small}$.

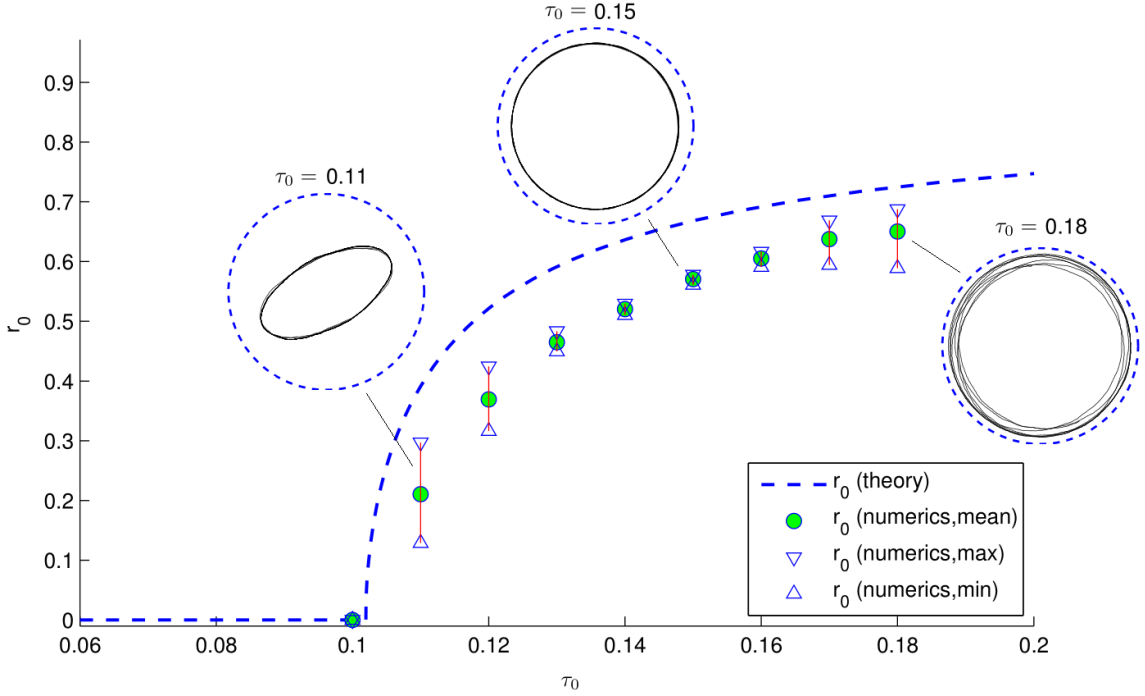


Figure 3.4: Radius of rotating spot as a function of $\tau_0 = \tau \varepsilon^2$. Parameter values are $A = 8$ and $\varepsilon = 0.02$. Dashed line is the asymptotic theory given by Proposition 3.7.1. Circle is the average long-time radius as observed from direct numerical simulations. Inserts show the long-time spike trajectory for τ_0 as indicated (with numerical trajectory shown in solid line and the theoretical rotating-spot trajectory of radius r_0 shown in dashed line).

We validated our computations by doubling the number of meshpoints. The prediction given by (3.3) is increasingly accurate with each halving of ε , although as expected from a log-log scaling, the improvement in accuracy is very slow.

3.7 Rotating Spot

When the spike is destabilized via translational instabilities, it starts to move as illustrated in figure 3.1, and may eventually settling into a circular orbit, rotating with some frequency ω_0 around some radius r_0 . The goal of this section is to compute ω_0 and r_0 asymptotically. Before proceeding, it is convenient to rescale

$$\tau = \frac{\tau_0}{\varepsilon^2}, \quad s = \varepsilon^2 t,$$

so that the problem (3.1) becomes

$$\varepsilon^2 v_s = \varepsilon^2 \Delta v - v + v^2 u, \quad \tau_0 u_s = \Delta u + A - \frac{v^2 u}{\varepsilon^2}. \quad (3.63)$$

Let $x_0(s)$ be the location of the spot. To make further progress, we make the ansatz that the spot travels along a circle of radius r_0 with constant angular velocity ω_0 , so that both u and v undergo a rigid rotation. That is, we assume

$$x_0(s) = e^{i\omega_0 s} r_0 \quad (3.64)$$

and $u(x, s) = u(xe^{-i\omega_0 s})$, $v(x, s) = v(xe^{-i\omega_0 s})$. We will estimate inner and outer region and perform matching in order to obtain a solvability condition which will determine the radius and the angular velocity of the spot.

Outer region. Away from spike location, we estimate the outer problem for u by

$$\Delta u + A = 2\pi S \delta(x - x_0) + \tau_0 u_s \quad (3.65)$$

with Neumann boundary condition $\partial_n u = 0$, $x \in \partial\Omega$. Here, S is defined by

$$2\pi S = \int \frac{uv^2}{\varepsilon^2} dx \sim \int_{\mathbb{R}^2} UV^2 dy, \quad y = \frac{x - x_0(s)}{\varepsilon}$$

The relation between S and A is determined by integrating (3.65) to obtain

$$\pi A = 2\pi S + \tau_0 \frac{d}{ds} \left(\int_{\Omega} u dx \right). \quad (3.66)$$

But since we assumed that u is rigidly rotating, the integral term $\int_{\Omega} u dx$ is independent of time s so that – just as for stationary spot – (3.66) simplifies to

$$S = \frac{A}{2}. \quad (3.67)$$

We write u as

$$u(x, s) = 2SG(x, s) + C$$

where G satisfies

$$\begin{cases} \Delta G + 1 = \pi \delta(x - x_0(s)) + \tau_0 G_s \\ \partial_n G = 0, \quad x \in \partial\Omega; \quad \int G dx = 0 \end{cases}; \quad x_0(s) = e^{i\omega_0 s} r_0, \quad (3.68)$$

and C is some (irrelevant for dynamics) constant. We now show that to leading order, (3.68) has the following singularity structure

$$G(x) = \frac{1}{2} \log |x - x_0| + \frac{\tau_0}{4} \dot{x}_0 \cdot (x - x_0) \log |x - x_0| + R_0(x, x_0). \quad (3.69)$$

where R_0 is the “regular part”, in the sense that its gradient exists at $x = x_0$; we give explicit expression for R_0 in section § 3.8. Note that when $\tau_0 = 0$, this corresponds to the usual Modified Green’s function on a disk; however the non-zero τ_0 induces an additional singularity term $\dot{x}_0 \cdot (x - x_0) \log |x - x_0|$. This latter term is “singular” in the sense that its gradient is infinite as $x \rightarrow x_0$ and therefore needs to be “peeled off”.

To see where this singularity comes from, first consider the source that moves along y -axis, with some speed c , $x_0(s) = (0, cs)$ on all of space; the free-space moving source Green’s function then satisfies

$$\Delta G = \tau_0 G_s + \pi \delta(x - x_0(s)); \quad x \in \mathbb{R}^2 \text{ and } x_0(s) = (0, cs) \quad (3.70)$$

In this case, transforming into co-moving coordinates $x = (\xi, \eta) + (0, cs)$ yields

$$G_{\xi\xi} + G_{\eta\eta} + c\tau_0 G_\eta = \pi \delta(\xi) \delta(\eta).$$

This problem has an exact solution of the form

$$G(\xi, \eta) = -\frac{1}{2} e^{\frac{-c\tau_0}{2}\eta} K_0\left(\frac{c\tau_0}{2}r\right), \quad r = \sqrt{\xi^2 + \eta^2}. \quad (3.71)$$

We then expand for small r and y using Taylor expansions $K_0(z) \sim -\log z$, $e^{c/2\eta} \sim 1 + \frac{c\tau_0}{2}\eta$ which yields

$$G(\xi, \eta) \sim \frac{1}{2} \left(1 - \frac{c\tau_0}{2}\eta\right) \log r + \dots \quad (3.72)$$

This also explains the choice of the constant $\frac{-1}{2}$ in (3.71) which gives the correct leading order behaviour $G \sim \frac{1}{2} \log r$ independent of $c\tau_0$. Replacing $c\eta$ by $\dot{x}_0 \cdot (x - x_0)$ and r by $|x - x_0|$ indeed yields the singularity structure (3.69). Further expanding x near x_0 , the outer problem for $u(x)$ is then given by

$$u(x) \sim S \log |x - x_0| - \frac{\tau_0 S}{2} \dot{x}_0 \cdot (x - x_0) \log |x - x_0| + 2S (x - x_0) \cdot \nabla R_0 + C, \quad x \rightarrow x_0. \quad (3.73)$$

where $\nabla R_0 = \nabla_x R_0(x, x_0)|_{x=x_0}$ and C is some constant.

Inner region. In the inner region near the spot, we rescale

$$y = \frac{x - x_0(s)}{\varepsilon}; \quad v(x, t) = V(y) \quad u(x, t) = U(y).$$

Then V, U satisfies

$$\begin{cases} -\varepsilon \nabla_y V \frac{dx_0}{ds} = \Delta_y V - V + UV^2 \\ -\tau_0 \varepsilon \nabla_y U \frac{dx_0}{ds} = \Delta_y U + A\varepsilon^2 - UV^2 \end{cases} \quad (3.74)$$

We then expand in ε ,

$$U = U_0 + \varepsilon U_1 + \dots, \quad V = V_0 + \varepsilon V_1 + \dots. \quad (3.75)$$

At the leading order we have

$$\begin{cases} \Delta V_0 - V_0 + U_0 V_0^2 = 0 \\ \Delta U_0 - U_0 V_0^2 = 0 \end{cases}. \quad (3.76)$$

At the next order we obtain

$$\begin{cases} \Delta V_1 - V_1 + 2U_0 V_0 V_1 + V_0^2 U_1 = -\nabla V_0 \cdot \dot{x}_0 \\ \Delta U_1 - 2U_0 V_0 V_1 - V_0^2 U_1 = -\tau_0 \nabla U_0 \cdot \dot{x}_0 \end{cases} \quad (3.77)$$

We assume that V_0, V_1 decays exponentially in the far field $|y| \gg 1$. To obtain the far-field behaviour for U_0 and U_1 , we rewrite the outer expansion (3.73) in the inner variables. This yields

$$u(x) = S \log \varepsilon |y| + \frac{\tau_0 S}{2} \dot{x}_0 \cdot y \varepsilon \log \varepsilon |y| + 2S \nabla R_0 \cdot y \varepsilon + C. \quad (3.78)$$

Upon collecting like terms in ε (while treating $\log \varepsilon$ as an $O(1)$ constant with respect to ε), we obtain

$$U_0 \sim S \log |y| + \chi(S), \quad |y| \gg 1; \quad (3.79)$$

The function $\chi(S)$ is the same as in (3.7) and the constant C in (3.78) determined through the relationship $\chi(S) = S \log \varepsilon + C$.

At the next order we obtain

$$U_1 \sim \frac{\tau_0 S}{2} \dot{x}_0 \cdot y \log |y| + \left(2S \nabla R_0 - \frac{\tau_0 S}{2} \dot{x}_0 \log \varepsilon \right) \cdot y, \quad |y| \gg 1.$$

Following the derivation in §3.4, we rewrite the system (3.77) as

$$\Delta W + M \cdot W = f, \quad y \in \mathbb{R}^2 \quad (3.80a)$$

$$W \sim \left(0, -\frac{S \tau_0}{2} \dot{x}_0 \cdot y \ln |y| + \vec{b} \cdot y \right)^t, \quad \text{as } |y| \rightarrow \infty \quad (3.80b)$$

where

$$\vec{b} = \frac{\tau_0 S}{2} \dot{x}_0 \log \varepsilon + 2S \nabla R_0, \quad (3.80c)$$

$$M = \begin{pmatrix} -1 + 2U_0 V_0 & V_0^2 \\ -2U_0 V_0 & -V_0^2 \end{pmatrix}, \quad \mathbf{W} = \begin{pmatrix} V_1 \\ U_1 \end{pmatrix}, \quad \mathbf{f} = \begin{pmatrix} -\nabla_y V_0 \cdot \dot{x}_0 \\ -\tau_0 \nabla_y U_0 \cdot \dot{x}_0 \end{pmatrix}. \quad (3.80d)$$

As in §3.4, to formulate the solvability condition, we let $P(\rho) = (P_1(\rho), P_2(\rho))^t$ be the solution to the homogeneous adjoint problem associated with (3.80a), given by (3.49). Define

$$P_c = P(\rho) \cos \theta, \quad P_s = P(\rho) \sin \theta \quad (3.81)$$

where $\cos \theta = \frac{y_1}{|y|}$ and $\sin \theta = \frac{y_2}{|y|}$; note that P_c and P_s both satisfy $\Delta P + M^t P = 0$.

Multiply (3.48a) by P_c^t and integrate by parts over a ball of large radius R to obtain the solvability condition

$$\int_{B_R} P_c^t \cdot f dy = \int_{\partial B_R} P_c^t \cdot \partial_\rho W - W \cdot \partial_\rho P_c^t dy. \quad (3.82)$$

The left hand side of (3.82) simplifies to

$$\int_{B_R} P_c^t \cdot f dy = -\pi \int_0^R (P_1 V_{0\rho} + \tau_0 P_2 U_{0\rho}) \dot{x}_{01} \rho d\rho \quad (3.83)$$

$$\sim -\pi \dot{x}_{01} \pi (\kappa_1 + \tau_0 S \log R - \tau_0 \kappa_2) \quad (3.84)$$

where κ_1, κ_2 are defined in (3.54b).

The right hand side of (3.82) simplifies to

$$\int_{\partial B_R} P_c^t \cdot \partial_\rho W - W \cdot \partial_\rho P_c^t dy = \pi \left(-S \tau_0 \dot{x}_{01} \left[\frac{1}{2} + \ln R \right] + 2b_1 \right) \quad (3.85)$$

where b_1 is the first component of vector b in (3.80c). Equating (3.84) and (3.85), note that the $\log R$ terms cancel each other out and we finally obtain

$$-(\kappa_1 - \tau_0 \kappa_2) \dot{x}_{01} = -\frac{S}{2} \tau_0 \dot{x}_{01} + 2b_1.$$

The second solvability condition involving \dot{x}_{01} is obtained similarly by using P_s instead of P_c . The two solvability conditions together yield

$$-(\kappa_1 - \tau_0 \kappa_2) \dot{x}_0 = -\frac{S}{2} \tau_0 \dot{x}_0 + 2 \left(2S \nabla R_0 - \frac{\tau_0 S}{2} \dot{x}_0 \log \varepsilon \right). \quad (3.86)$$

Solving for \dot{x}_0 and using $S = A/2$ then yields

$$\frac{d}{ds} x_0 = \beta \nabla R_0 \quad \text{where } \beta = \frac{1}{\tau_0 \left(\frac{1}{4} \log \varepsilon + \frac{1}{8} + \frac{\kappa_2}{2A} \right) - \frac{\kappa_1}{2A}} \quad (3.87)$$

In Appendix 3.8 we derive an exact expansion for R_0 in terms of an infinite series of Bessel functions. By symmetry, we may assume without loss of generality that x_0 lies on the positive x-axis (i.e. $s = 0$). Then $\frac{d}{ds} x_0|_{s=0} = (0, \omega_0 r_0)$ and we write:

$$\nabla R_0(x, x_0)|_{x_0=(r_0, 0), x=x_0} = (F_1(r_0, \omega), F_2(r_0, \omega)), \quad \text{where } \omega = \omega_0 \tau_0, \quad (3.88)$$

with F_1, F_2 given in (3.96). Equation (3.88) is then equivalent to $F_1 = 0$, $\omega_0 r_0 = F_2$, or

$$F_1(r_0, \omega) = 0; \quad \tau_0 = \frac{2\kappa_1}{A \left(\log \varepsilon + \frac{1}{2} - \frac{4F_2(r_0, \omega)}{\omega r_0} \right) + \kappa_2}; \quad \omega_0 = \omega / \tau_0. \quad (3.89)$$

In addition, as we show in Appendix 3.8, the threshold $\tau_{h,small}$ of Proposition 3.4.1 is recovered in the limit $r_0 \rightarrow 0$. We summarize our construction as follows.

Proposition 3.7.1 *The Schnakenberg model (3.1) on a unit disk admits a rotating spot solution for $\tau > \tau_{h,small}$, where $\tau_{h,small}$ is the Hopf bifurcation value with respect to translational eigenvalues as given in Proposition 3.4.1. The spot center $x_0 = r_0 e^{i\omega_0 \varepsilon^2 t}$ rotates with angular velocity $\omega_0 \varepsilon^2$ and radius r_0 . as determined through (3.89).*

Figure 3.4 shows a comparison between the numerical simulations of the full system (3.1) and the asymptotic prediction for the radius of the rotating spot. For example take $\tau_0 = 0.15$, $A = 8$, $\varepsilon = 0.02$. Then using (3.54b) we first compute $\kappa_1 = -1.2938$ and $\kappa_2 = 3.54334$ by solving the radial core problem and the adjoint eigenvalue problem using a boundary value problem solver in Matlab (`bvp4c`). From (3.89) we then obtain $r_0 = 0.669$ and $\omega = 6.1994$. Full numerical simulations of the original model (3.1) exhibit a rotating spot whose radius is $r_{0,numeric} \approx 0.57$, in good agreement with the theoretical prediction. Although the Proposition 3.7.1 applies for any $\tau > \tau_{h,small}$, the rotating spot solution is not always stable as Figure 3.4 shows. For example when $\tau_0 = 0.11$, the numerical solution appears to be in the shape of an ellipse whereas for $\tau_0 = 0.18$ the radius is close to the theoretical prediction but appears to vary with time, generating an annular region. More complex trajectories are possible as shown in Figure 3.5.

3.8 Green's Function For Rotating Spot

In this appendix we compute explicitly gradient of the regular part of the rotating Green's function, defined through (3.68), (3.69). In the rotating frame, the Green's function G from (3.68) satisfies

$$\frac{\partial^2 G}{\partial r^2} + \frac{1}{r} \frac{\partial G}{\partial r} + \frac{1}{r^2} \frac{\partial^2 G}{\partial \theta^2} + \omega \frac{\partial G}{\partial \theta} = 1 - \pi \delta(r - r_0) \delta(\theta) \quad (3.90)$$

$$\partial_r G = 0 \quad \mathbf{x} \in \partial\Omega. \quad (3.91)$$

where

$$\omega = \tau_0 \omega_0. \quad (3.92)$$

Using separation of variable, we write $G(r, \theta)$ as

$$G = G_0(r) + \sum_{m=1}^{\infty} (G_m(r)e^{im\theta} + c.c) \quad (3.93)$$

where c.c refers to the complex conjugate of the term involving the summation. Substituting (3.93) into (3.90) and recalling the Newmann boundary condition, we obtain:

$$\frac{\partial^2 G_0}{\partial r^2} + \frac{1}{r} \frac{\partial G_0}{\partial r} = 1 - \pi \delta(r - r_0) \delta(\theta), \quad G_0 \text{ bounded as } r \rightarrow 0, \quad G'_0(1) = 0 \quad (3.94a)$$

$$\begin{cases} \frac{\partial^2 G_m}{\partial r^2} + \frac{1}{r} G_m - \frac{m^2}{r^2} G_m + im\omega G_m = -\pi \delta(r - r_0) \delta(\theta), & m > 0 \\ G_m \text{ bounded as } r \rightarrow 0, \quad G'_m(1) = 0 \end{cases} \quad (3.94b)$$

For $m > 0$, the homogeneous solution of (3.94b) may be written as

$$G_m(r, \omega) = a_m I_m(c_m r) + b_m K_m(c_m r); \quad c_m \equiv \sqrt{-i\omega m}$$

where $I_m(r)$ and $K_m(r)$ are m-th order modified Bessel functions of the first and second kind, respectively. Solving (3.94b) separately for $r < r_0$ and $r > r_0$, and applying appropriate continuity and jump conditions at $r = r_0$, we obtain the solution for G_m ,

$$G_m(r) = \begin{cases} \frac{1}{2} \left[-\frac{K'_m(c_m)}{I'_m(c_m)} I_m(c_m r_0) + K_m(c_m r_0) \right] I_m(c_m r), & 0 < r < r_0 \\ \frac{1}{2} \left[-\frac{K'_m(c_m)}{I'_m(c_m)} I_m(c_m r) + K_m(c_m r) \right] I_m(c_m r_0), & r_0 < r < 1 \end{cases}$$

where $c_m \equiv \sqrt{-i\omega m}$, $m \neq 0$, $I'_m(c_m)$ and $K'_m(c_m)$ denote the derivatives of I_m and K_m evaluated at c_m , respectively. In a similar way, we find that the solution to (3.94) for $G_0(r)$,

$$G_0(r) = \frac{r^2}{4} + \frac{2r_0^2 - 3}{8} - \begin{cases} \frac{1}{2} \log r_0, & 0 < r < r_0 \\ \frac{1}{2} \log r, & r_0 < r < 1 \end{cases}.$$

Recall that

$$R_0 = G - S_1 - S_2$$

where

$$S_1 := -\frac{1}{2} \log |x - x_0|; \quad S_2 := \frac{1}{4} \tau_0 \frac{\partial x_0}{\partial t} \cdot (x - x_0) \log |x - x_0|. \quad (3.95)$$

To calculate R_0 and its gradient, we first expand the singular parts S_1 and S_2 in terms of their Fourier series, then take the limit $\theta \rightarrow 0, r \rightarrow r_0^-$. We have

$$S_1 := -\frac{1}{2} \log|x - x_0| = -\frac{1}{2} \log(r_M) + \frac{1}{2} \sum_{m \geq 1} \frac{\rho^m}{2m} (e^{im\theta} + e^{-im\theta}),$$

where $r_M = \max(r, r_0)$, $\rho = \frac{\min(r, r_0)}{\max(r, r_0)}$;

$$\frac{1}{4} \tau_0 \frac{\partial x_0}{\partial t} \cdot (x - x_0) = -\frac{\omega r r_0}{8} (ie^{i\theta} - ie^{-i\theta});$$

$$S_2 = \frac{\omega r r_0}{8i} \left[\left(\log(r_M) + \frac{\rho^2}{4} \right) e^{i\theta} - \frac{1}{2} \sum_{m \geq 2} \left(\frac{1}{m-1} \rho^{-1} - \frac{1}{m+1} \rho \right) \rho^m e^{im\theta} \right] + c.c.$$

The function F_1 and F_2 defined through (3.88) are then expressed in terms of polar variables as

$$F_1(r_0, \omega) = \partial_r R_0|_{r=r_0^-, \theta=0}; \quad F_2(r_0, \omega) = \frac{1}{r_0} \partial_\theta R_0|_{r=r_0^-, \theta=0}$$

Differentiating with respect to r and θ and then evaluating at $r = r_0^-$ and $\theta = 0$, we finally obtain the following expressions,

$$F_1(r_0, \omega) = \frac{r_0}{2} + \sum_{m \geq 1} \left(2 \operatorname{Re} (G'_m(r_0^-)) - \frac{1}{2r_0} \right) \quad (3.96a)$$

$$\begin{aligned} r_0 F_2(r_0, \omega) &= -\frac{\omega r_0^2}{4} \left[\left(\log(r_0) + \frac{1}{4} \right) \right] - 2 \operatorname{Im} (G_1(r_0^-)) \\ &\quad + \sum_{m \geq 2} \left(-2m \operatorname{Im} G_m(r_0^-) + \frac{\omega r_0^2}{4} \frac{m}{m^2 - 1} \right) \end{aligned} \quad (3.96b)$$

where

$$G_m(r_0^-) = \frac{1}{2} \left[-\frac{K'_m(c_m)}{I'_m(c_m)} I_m(c_m r_0) + K_m(c_m r_0) \right] I_m(c_m r_0); \quad (3.96c)$$

$$G'_m(r_0^-) = \frac{c_m}{2} \left[-\frac{K'_m(c_m)}{I'_m(c_m)} I_m(c_m r_0) + K_m(c_m r_0) \right] I'_m(c_m r_0). \quad (3.96d)$$

$$c_m \equiv -i\sqrt{i\omega m}$$

The Hopf bifurcation threshold derived in Proposition 3.4.1 corresponds to letting $r_0 \rightarrow 0$. To establish the equivalence between the expression for r_0 in Proposition 3.7.1 and the threshold $\tau_{h,small}$ in Proposition 3.4.1, we using the small-argument expansions for K_m and I_m to obtain the leading-order expressions,

$$F_1(r, \omega) = \frac{r_0}{2} + 2 \operatorname{Re} (G'_1(r_0^-)) - \frac{1}{2r_0};$$

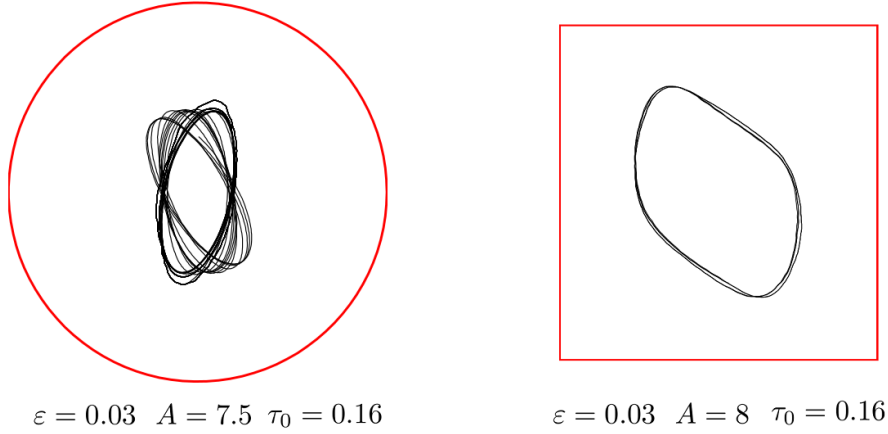


Figure 3.5: Complex spot trajectories. Left the domain is a unit disk. Right: the domain is a square of area π .

$$r_0 F_2(r_0, \omega) = -2 \operatorname{Im} (G_1(r_0)) - \frac{\omega r_0^2}{4} \left[\left(\log(r_0) + \frac{1}{4} \right) \right]$$

Further simplifying, we obtain

$$F_1(r_0, \omega) \sim \frac{r_0}{4} \left(-\operatorname{Im} \left(\frac{K_1'(\sqrt{-\omega i})}{I_1'(\sqrt{-\omega i})} \right) \omega + 2 - \frac{\pi \omega}{4} \right), \quad r_0 \ll 1$$

$$F_2(r_0, \omega) \sim \frac{1}{4} r_0 \omega \left(-\operatorname{Re} \left(\frac{K_1'(\sqrt{-\omega i})}{I_1'(\sqrt{-\omega i})} \right) + \frac{1}{2} \log(\omega/4) + \gamma - \frac{1}{2} \right), \quad r_0 \ll 1$$

Setting $F_1 = 0$ and letting $r_0 \rightarrow 0$, we obtain $\omega = \omega_c$ is the root of (3.55a). Then setting $F_2 = 0$ and recalling that $\omega = \omega_0 \tau_0$, one recovers Proposition 3.7.1.

3.9 Discussion

We have used formal asymptotics to compute Hopf bifurcation thresholds $\tau = \tau_{h,large}$ and $\tau = \tau_{h,small}$ that induce spike oscillations in either height ($\tau_{h,large}$) or position ($\tau_{h,small}$) for the Schankenberg model. These two thresholds cross at $A = A_c$. That is, height oscillations dominate ($\tau_{h,large} < \tau_{h,small}$) when $A < A_c$ whereas position oscillations dominate ($\tau_{h,small} < \tau_{h,large}$) when $A > A_c$, where A_c given by (3.3) has an $O(1/\log(\log \varepsilon))$ scaling. Despite the extremely slow decay of A_c as $\varepsilon \rightarrow 0$, the asymptotically computed value of A_c agrees surprisingly well with numerics even with $\varepsilon = 0.01$ (the constants in (3.3) are very important to get a good agreement). We remark that in one dimension, a similar “double-hopf” point was found in several papers [44–46]. However it has an *algebraic* scaling $A_c = O(\varepsilon^{1/6})$ ([45]).

In the regime $\tau_{h,small} < \tau < \tau_{h,large}$, we have constructed a periodic spike solution consisting of a rotating spot inside a unit disk, and computed the radius and speed of the rotation by expanding the underlying Green's function in terms of complex Bessel series. Numerical experiments suggest that the rotating solution is not always stable – see Figure 3.4. In particular, for τ just slightly above the bifurcation point $\tau_{h,small}$, the spike trajectory is an ellipse, whereas for τ sufficiently large, the spot path fills out an annulus. It would be a very interesting to study the stability of these rotating spots.

It would be interesting to study more general spot motion and for more general domains. Figure 3.5 gives some idea of possible trajectories. A preliminary goal is to derive and numerically simulate the reduced equations of motion. The reduced equations of motion comprise a coupled PDE-ODE system with a moving source, analogous to the equations derived in §3.7. The numerical difficulty is the ODE for the source location requires an extraction of a very weakly singular part of the moving Green's function.

Circular spot motion is intimately related to the model of a small rotating trap inside an insulated unit disk, which was recently studied in [23, 101]. There, the main goal was to minimize the mean first passage time (MFPT) for a rotating trap $x_0 = r_0 e^{i\omega t}$ (or several rotating traps) as a function of its radius r_0 and its angular velocity ω . It turned out that the optimal radius r_0 and velocity ω have precisely the same relation $F_1(r_0, \omega) = 0$ as we found in Proposition 3.7.1. As a result, for small angular velocity ($\omega < \omega_c$), it was optimal for the trap to be located at the origin, whereas for $\omega > \omega_c$ it was better for the spot to move. This is the precise analogue of the Hopf bifurcation computed in Proposition 3.4.1.

Spot motion was also observed for a three-component gas-discharge system [102]. There, the authors also analysed complex spot dynamics, including spot collision and splitting. The initial instability inducing spot motion in this system was further analysed in detail in [103] where theoretical and numerical study of the bifurcation from a stationary to a moving spot was performed. Let us also mention the work [104] where complex motion of a self-propelled deformable particle was studied.

While in many aspects, GM, GS and Schakengerg models are very similar mathematically, the oscillations of spot positions have never been observed in GM model. It would be interesting to have a better understanding of the kind of general conditions

that are needed to observe position oscillations.

Chapter 4

Dynamics of the Spot in Three Dimensional Schankenberg Model

The results in this chapter have appeared in section 4 in the paper [21], which is a joint work between myself, Justin Tzou, Theodore Kolokolnikov, and Michael Ward. The text in this chapter is taken from [21], and was written mostly by Ward and Tzou. The analysis in this chapter was performed mostly by myself. All numerical computations were done by myself.

In this chapter, we study the three dimensional Schankenberg model. In dimensionless form, the rescaled singularly perturbed Schnakenberg model is:

$$v_t = \varepsilon^2 \Delta v - v + uv^2, \quad \mathbf{x} \in \Omega; \quad \partial_n v = 0, \quad \mathbf{x} \in \partial\Omega, \quad (4.1a)$$

$$\varepsilon^3 u_t = \frac{D}{\varepsilon} \Delta u + A - \frac{uv^2}{\varepsilon^3}, \quad \mathbf{x} \in \Omega; \quad \partial_n u = 0, \quad \mathbf{x} \in \partial\Omega. \quad (4.1b)$$

When the stability condition on the source strengths holds, in §4.1 we show that the spot locations associated with an N -spot symmetric quasi-equilibrium evolves to a true steady-state configuration over a long $\mathcal{O}(\varepsilon^{-3})$ time-scale. To leading order in ε , in (4.22) of Main Result 4.1.2 we show that the slow spot dynamics satisfy an ODE system defined by a gradient flow of a certain discrete energy $\mathcal{H}(\mathbf{x}_1, \dots, \mathbf{x}_N)$, which involves the Neumann Green's function and its regular part. Minima of this discrete energy are stable equilibrium points of this limiting ODE spot dynamics, and we explicitly identify certain such equilibrium spot configurations. A higher-order analysis, leading to the ODE dynamics (4.17) coupled to the constraints (4.7), shows that the slow spot dynamics consists of a weakly coupled differential algebraic system (DAE) of ODEs, in which the spot source strengths depend only weakly as $\varepsilon \rightarrow 0$ on the spot locations.

In comparison, in a 2-D setting, the dynamical characterization of slow spot dynamics consists of a DAE system that couples ODEs for the spot locations to a

nonlinear algebraic system for the spot source strengths defined in terms of a Green's matrix, which depends on the overall spot configuration (cf. [50], [53], [105]). This DAE system of slow spot dynamics in 2-D is rather strongly coupled, owing to the logarithmic gauge $\nu = \mathcal{O}(-1/\log \varepsilon)$. As a result of this strong coupling in 2-D, spot self-replication events can be triggered intrinsically during the slow dynamics of a collection of spots whenever a particular spot source strength exceeds a critical value (cf. [50], [53], [106]). In contrast, in our 3-D setting where the spots have an asymptotically common source strength, with an error of only $\mathcal{O}(\varepsilon)$, such intrinsically triggered spot self-replication events do not typically occur for ε small. Instead, in 3-D an external parameter such as the feed-rate, or the domain volume, needs to be increased dynamically in order to trigger spot self-replication events.

In §4.1.1 we extend our asymptotic theory for constant A to the case of a spatially variable feed, where $A = A(\mathbf{x})$ in (4.1b). To leading order in ε , the slow spot dynamics is characterized in Main Result 4.1.3 in terms of the discrete energy \mathcal{H} and an additional nonlocal term involving $A(\mathbf{x})$. In the unit ball, our ODEs characterizing slow spot dynamics are verified with full numerical FlexPDE6 simulations of (4.1). For a few specific choices of the variable feed-rate, we illustrate from our ODEs, and from full numerical PDE simulations, the effect of spot pinning, whereby a spot trajectory can be pinned to a new equilibrium state created by the non-uniform feed-rate. Finally, in §4.2 we suggest a few open problems that warrant further study.

4.1 Slow Spot Dynamics

In this section, we analyze the slow dynamics associated with an N -spot quasi-equilibrium solution. To derive an ODE system characterizing the slow spot dynamics, we must extend the calculation to one higher order beside the leading order. We will proceed by the method of formal asymptotics.

In the inner region near the j -th spot, we let $\mathbf{x}_j = \mathbf{x}_j(\sigma)$ where $\sigma = \varepsilon^3 t$, and expand the inner solution as

$$\begin{aligned} \mathbf{y} &= \varepsilon^{-1}(\mathbf{x} - \mathbf{x}_j(\sigma)), & v(\mathbf{x}_j + \varepsilon\mathbf{y}) &= \sqrt{D} [V_j\varepsilon(\rho) + \varepsilon^2 V_{j2}(\mathbf{y}) + \cdots], \\ u(\mathbf{x}_j + \varepsilon\mathbf{y}) &= \frac{1}{\sqrt{D}} [U_j\varepsilon(\rho) + \varepsilon^2 U_{j2}(\mathbf{y}) + \cdots], \end{aligned} \quad (4.2)$$

with $\rho \equiv |\mathbf{y}|$, where $U_{j\varepsilon}, V_{j\varepsilon}$ satisfy the radially symmetric core problem

$$\Delta_\rho V_{j\varepsilon} - V_{j\varepsilon} + U_{j\varepsilon} V_{j\varepsilon}^2 = 0, \quad V'_{j\varepsilon}(0) = 0, \quad V_{j\varepsilon} \rightarrow 0, \quad \text{as } \rho \rightarrow \infty, \quad (4.3a)$$

$$\Delta_\rho U_{j\varepsilon} - U_{j\varepsilon} V_{j\varepsilon}^2 = 0, \quad U'_{j\varepsilon}(0) = 0, \quad (4.3b)$$

with far-field behavior

$$U_{j\varepsilon} \sim \mu_j - S_{j\varepsilon}/\rho + \dots, \quad \text{as } \rho \rightarrow \infty, \quad (4.3c)$$

where $\mu_j \equiv \mu_0(S_{j\varepsilon})$.

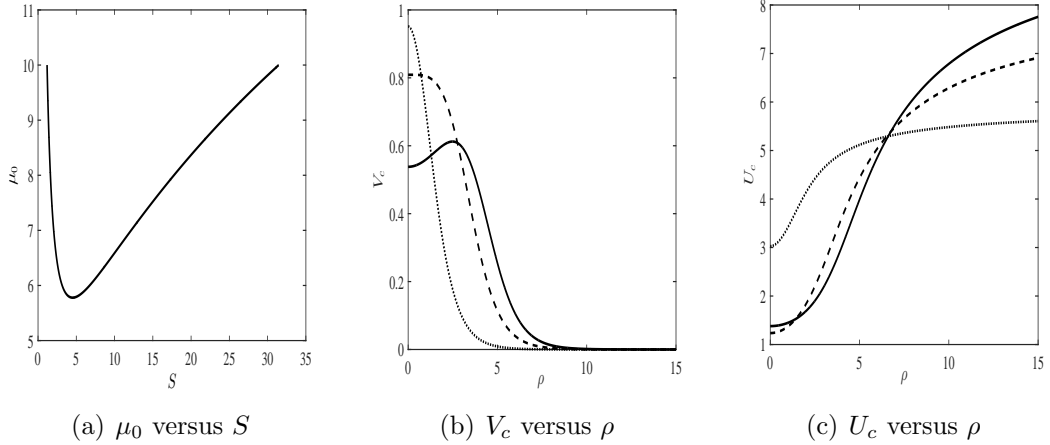


Figure 4.1: In (a), we plot the relationship $\mu_0 = \mu_0(S)$ as obtained from a numerical solution of the core problem (4.3). The fold point at $(S_{cf}, \mu_{0f}) \approx (4.52, 5.78)$ divides $\mu_0(S)$ into a left and right branch. In (b), we plot V_c versus $\rho = |\mathbf{y}|$ for $S = 3.67$ (dotted), $S = 18.7$ (dashed), and $S = 29.1$ (solid). For $S \gtrsim 18.7$, the profile is volcano-shaped so that the maximum of V_c occurs at $\rho > 0$. When $S \lesssim 18.7$, the maximum of V_c is at $\rho = 0$. In (c), we show the corresponding profiles for $U_c(\rho)$.

The corresponding outer solution satisfies:

$$\begin{cases} D\Delta u + A\varepsilon \sim 4\pi\varepsilon \sum_{j=1}^N S_{j\varepsilon} \delta(\mathbf{x}) - \mathbf{x}_j \\ \partial_n u = 0, \quad \mathbf{x} \in \partial\Omega \end{cases} \quad (4.4)$$

Impose Divergence Theorem on (4.4), we obtain:

$$A|\Omega| = 4\pi \sum_{j=1}^N S_{j\varepsilon}$$

Define $G(\mathbf{x}, \boldsymbol{\xi})$ to be the unique Neumann Green's function satisfying

$$\Delta G = \frac{1}{|\Omega|} - \delta(\mathbf{x} - \boldsymbol{\xi}), \quad \mathbf{x} \in \Omega; \quad \partial_n G = 0, \quad \mathbf{x} \in \partial\Omega, \quad (4.5a)$$

$$G(\mathbf{x}; \boldsymbol{\xi}) = \frac{1}{4\pi|\mathbf{x} - \boldsymbol{\xi}|} + R(\mathbf{x}; \boldsymbol{\xi}), \quad \text{as } \mathbf{x} \rightarrow \boldsymbol{\xi}; \quad \int_{\Omega} G \, d\mathbf{x} = 0, \quad (4.5b)$$

where $R(\mathbf{x}; \boldsymbol{\xi})$ is smooth. In (4.5b), $R(\boldsymbol{\xi}; \boldsymbol{\xi})$ is called the regular part of G at the singularity $\mathbf{x} = \boldsymbol{\xi}$.

We can solve (4.4) exactly to obtain:

$$u \sim \xi - \frac{4\pi\varepsilon}{\sqrt{D}} \sum_{j=1}^N S_{j\varepsilon} G(\mathbf{x}; \mathbf{x}_j), \quad \sum_{i=1}^N S_{i\varepsilon} = \frac{A|\Omega|}{4\pi\sqrt{D}}, \quad (4.6)$$

where $S_{j\varepsilon}$, for $j = 1, \dots, N$, and ξ satisfy the $N + 1$ dimensional weakly coupled nonlinear algebraic system:

$$\xi - \frac{4\pi\varepsilon}{\sqrt{D}} (\mathcal{G}\mathbf{S})_j = \frac{\mu_0(S_{j\varepsilon})}{\sqrt{D}}, \quad j = 1, \dots, N; \quad \sum_{j=1}^N S_{j\varepsilon} = \frac{A|\Omega|}{4\pi\sqrt{D}}. \quad (4.7)$$

Here $\mu_0(S_{j\varepsilon})$ is to be computed from the core problem (4.3), $\mathbf{S} \equiv (S_{1\varepsilon}, \dots, S_{N\varepsilon})^T$, and \mathcal{G} is the symmetric Neumann Green's matrix with matrix entries $(\mathcal{G})_{ij} = G(\mathbf{x}_j; \mathbf{x}_i)$ for $i \neq j$ and $(\mathcal{G})_{jj} = R(\mathbf{x}_j; \mathbf{x}_j)$.

We first expand u as $\mathbf{x} \rightarrow \mathbf{x}_j$, while retaining the higher-order gradient terms associated with the Green's function. Upon using (4.5b), we obtain in terms of inner variables that, as $\mathbf{x} \rightarrow \mathbf{x}_j$,

$$u \sim \xi - \frac{S_{j\varepsilon}}{\sqrt{D}\rho} - \frac{4\pi\varepsilon}{\sqrt{D}} (\mathcal{G}\mathbf{S})_j - \frac{4\pi\varepsilon^2}{\sqrt{D}} \mathbf{y} \cdot \left(S_{j\varepsilon} \nabla_{\mathbf{x}} R(\mathbf{x}; \mathbf{x}_j)|_{\mathbf{x}=\mathbf{x}_j} + \sum_{\substack{i=1 \\ i \neq j}}^N S_{i\varepsilon} \nabla_{\mathbf{x}} G(\mathbf{x}; \mathbf{x}_i)|_{\mathbf{x}=\mathbf{x}_j} \right), \quad (4.8)$$

where \mathcal{G} is the Neumann Green's matrix. The $\mathcal{O}(\varepsilon^2)$ term in (4.8) is the motivation for the form of the higher-order expansion in (4.2) and the scaling for the slow time-scale $\sigma = \varepsilon^3 t$.

Upon substituting (4.2) into (4.1), and matching the inner solution to the $\mathcal{O}(\varepsilon^2)$

term in (4.8), we obtain that $\mathbf{W}_2 = (V_{j2}, U_{j2})^T$ satisfies

$$\begin{aligned} \mathcal{L}\mathbf{W}_2 &\equiv \Delta_{\mathbf{y}}\mathbf{W}_2 + \mathcal{M}_\varepsilon\mathbf{W}_2 = - \begin{pmatrix} \mathbf{x}'_j \cdot \nabla_{\mathbf{y}} V_{j\varepsilon} \\ 0 \end{pmatrix}, \quad \mathbf{y} \in \mathbb{R}^2; \\ \mathbf{W}_2 &\sim \begin{pmatrix} 0 \\ \mathbf{b}_j \cdot \mathbf{y} \end{pmatrix}, \quad \text{as } |\mathbf{y}| \rightarrow \infty. \end{aligned} \quad (4.9a)$$

Here the 2×2 matrix \mathcal{M}_ε and the vector \mathbf{b}_j are defined by

$$\begin{aligned} \mathcal{M}_\varepsilon &\equiv \begin{pmatrix} -1 + 2U_{j\varepsilon}V_{j\varepsilon} & V_{j\varepsilon}^2 \\ -2U_{j\varepsilon}V_{j\varepsilon} & -V_{j\varepsilon}^2 \end{pmatrix}, \\ \mathbf{b}_j &\equiv -4\pi S_{j\varepsilon} \nabla_{\mathbf{x}} R(\mathbf{x}; \mathbf{x}_j)|_{\mathbf{x}=\mathbf{x}_j} - 4\pi \sum_{\substack{i=1 \\ i \neq j}}^N S_{i\varepsilon} \nabla_{\mathbf{x}} G(\mathbf{x}; \mathbf{x}_i)|_{\mathbf{x}=\mathbf{x}_j}. \end{aligned} \quad (4.9b)$$

Let $\mathbf{y} = (y_1, y_2, y_3)^T$ and $\mathbf{W}_{j\varepsilon} \equiv (V_{j\varepsilon}, U_{j\varepsilon})^T$. We observe upon differentiating the core problem (4.3) with respect to i -th coordinate y_i of \mathbf{y} that

$$\mathcal{L}(\partial_{y_i} \mathbf{W}_{j\varepsilon}) = 0 \quad \text{where} \quad \partial_{y_i} \mathbf{W}_{j\varepsilon} \equiv \rho^{-1} \begin{pmatrix} V'_{j\varepsilon}(\rho) \\ U'_{j\varepsilon}(\rho) \end{pmatrix} y_i, \quad \text{for } i = 1, 2, 3.$$

This shows that the dimension of the nullspace of \mathcal{L} , and consequently \mathcal{L}^* , is at least three-dimensional. We will assume that this nullspace is exactly three-dimensional, which we can verify numerically provided that $S_{j\varepsilon}$ does not coincide with the critical value $\Sigma_2 \approx 20.16$ for the peanut-splitting instability.

From a Fredholm alternative criterion, the following lemma provides a necessary condition for (4.9) to have a solution.

Lemma 4.1.1 *A necessary condition for (4.9) to have a solution is that $\mathbf{x}_j(\sigma)$ satisfies*

$$\mathbf{x}'_j = -\frac{3}{\kappa_1} \mathbf{b}_j, \quad \kappa_1 = \kappa_1(S_{j\varepsilon}) \equiv \int_0^\infty \rho^2 P_1(\rho) V'_{j\varepsilon}(\rho) d\rho, \quad (4.10)$$

where $P_1(\rho)$ is the first component of $\mathbf{P}(\rho) \equiv (P_1(\rho), P_2(\rho))^T$, which satisfies

$$\Delta_\rho \mathbf{P} - \frac{2}{\rho^2} \mathbf{P} + \mathcal{M}_\varepsilon^T \mathbf{P} = 0, \quad 0 < \rho < \infty; \quad \mathbf{P} \sim \begin{pmatrix} 0 \\ 1/\rho^2 \end{pmatrix}, \quad \text{as } \rho \rightarrow \infty, \quad (4.11)$$

and $\mathbf{P} = \mathcal{O}(\rho)$ as $\rho \rightarrow 0$, where $\Delta_\rho \mathbf{P} \equiv \mathbf{P}'' + 2\rho^{-1} \mathbf{P}'$.

Proof: We first seek three independent nontrivial solutions to the homogeneous adjoint problem $\mathcal{L}^*\Psi \equiv \Delta_{\mathbf{y}}\Psi + \mathcal{M}_{\varepsilon}^T\Psi = 0$ in the form $\Psi_i \equiv \mathbf{P}(\rho)y_i/\rho$ for $i = 1, \dots, 3$. Since

$$\Delta_{\mathbf{y}}[\mathbf{P}y_i/\rho] = \left(\Delta_{\rho}\mathbf{P} - \frac{2}{\rho^2}\mathbf{P} \right) \frac{y_i}{\rho},$$

we readily obtain that $\mathbf{P}(\rho)$ satisfies $\Delta_{\rho}\mathbf{P} - 2\rho^{-2}\mathbf{P} + \mathcal{M}_{\varepsilon}^T\mathbf{P} = 0$. To establish the far-field behavior of \mathbf{P} , we obtain using (4.9b) for $\mathcal{M}_{\varepsilon}$, and the fact that $V_{j0} \rightarrow 0$ exponentially as $\rho \rightarrow \infty$, that $P_2(\rho)$ satisfies $P_2'' + 2\rho^{-1}P_2' - 2\rho^{-2}P_2 \approx 0$ for $\rho \gg 1$. The decaying solution to this Euler's equation implies that $P_2 = \mathcal{O}(\rho^{-2})$ as $\rho \rightarrow \infty$, and the eigenfunction is normalized by imposing the precise behavior that $P_2 \sim 1/\rho^2$ as $\rho \rightarrow \infty$. In contrast, for $P_1(\rho)$ we obtain that $P_1'' + 2\rho^{-1}P_1' - P_1 \approx 0$ as $\rho \rightarrow \infty$, so that P_1 decays exponentially as $\rho \rightarrow \infty$. In this way, we obtain that \mathbf{P} satisfies (4.11).

Next, to derive our solvability condition we use Green's identity over a large ball of radius $|\mathbf{y}| = \rho_0 \gg 1$ to obtain that

$$\lim_{\rho_0 \rightarrow \infty} \int_{\Omega_{\rho_0}} (\Psi_i^T \mathcal{L}\mathbf{W}_2 - \mathbf{W}_2^T \mathcal{L}^*\Psi_i) d\mathbf{y} = \lim_{\rho_0 \rightarrow \infty} \int_{\partial\Omega_{\rho_0}} (\Psi_i^T \partial_{\rho}\mathbf{W}_2 - \mathbf{W}_2^T \partial_{\rho}\Psi_i) \Big|_{\rho=\rho_0} dS. \quad (4.12)$$

With $\Psi_i \equiv \mathbf{P}(\rho)y_i/\rho$, and for a fixed $i \in \{1, 2, 3\}$, we first calculate the left-hand side of this expression using (4.9a) to obtain

$$\begin{aligned} \lim_{\rho_0 \rightarrow \infty} \int_{\Omega_{\rho_0}} (\Psi_i^T \mathcal{L}\mathbf{W}_2 - \mathbf{W}_2^T \mathcal{L}^*\Psi_i) d\mathbf{y} &= - \lim_{\rho_0 \rightarrow \infty} \int_{\Omega_{\rho_0}} \frac{y_i}{\rho} P_1(\rho) (\mathbf{x}'_j \cdot \nabla_{\mathbf{y}} V_{j\varepsilon}) d\mathbf{y}, \\ &= - \sum_{k=1}^3 x'_{jk} \lim_{\rho_0 \rightarrow \infty} \int_{\Omega_{\rho_0}} \frac{y_i y_k}{\rho^2} V'_{j\varepsilon}(\rho) P_1(\rho) d\mathbf{y}, \end{aligned} \quad (4.13)$$

where $\mathbf{x}'_j \equiv (x'_{j1}, x'_{j2}, x'_{j3})^T$. By using symmetry considerations, we readily establish that $\int_{\Omega_{\rho_0}} y_i y_k f(\rho) d\mathbf{y} = 0$ when $i \neq k$ and $\int_{\Omega_{\rho_0}} y_i^2 f(\rho) d\mathbf{y} = \frac{4\pi}{3} \int_0^{\rho_0} \rho^4 f(\rho) d\rho$ for any radially symmetric function $f(\rho)$. In this way, the last expression (4.13) becomes

$$\lim_{\rho_0 \rightarrow \infty} \int_{\Omega_{\rho_0}} (\Psi_i^T \mathcal{L}\mathbf{W}_2 - \mathbf{W}_2^T \mathcal{L}^*\Psi_i) d\mathbf{y} = -\frac{4\pi}{3} x'_{ji} \int_0^{\infty} \rho^2 P_1(\rho) V'_{j\varepsilon}(\rho) d\rho. \quad (4.14)$$

Next, we calculate the right-hand side of (4.12). For the first term on the right-hand side of (4.12) we use $P_2(\rho) \sim 1/\rho^2$, $U_{j1} \sim \mathbf{b}_j \cdot \mathbf{y}$ and $\partial_{\rho} U_{j1} \sim \mathbf{b}_j \cdot \mathbf{y}/\rho$ as $\rho \rightarrow \infty$, to estimate that

$$\lim_{\rho_0 \rightarrow \infty} \int_{\partial\Omega_{\rho_0}} \Psi_i^T \partial_{\rho}\mathbf{W}_2 \Big|_{\rho=\rho_0} dS = \lim_{\rho_0 \rightarrow \infty} \int_{\partial\Omega_{\rho_0}} P_2(\rho) \frac{y_i}{\rho} \partial_{\rho} U_{j1} \Big|_{\rho=\rho_0} dS = \lim_{\rho_0 \rightarrow \infty} \int_{\partial\Omega_{\rho_0}} \frac{y_i}{\rho^4} (\mathbf{b}_j \cdot \mathbf{y}) \Big|_{\rho=\rho_0} dS.$$

Then, since $\int_{\partial\Omega_{\rho_0}} y_i y_k f(\rho)|_{\rho=\rho_0} dS = 0$ for $i \neq k$, and writing $dS = \rho_0^2 d\Omega_0$, where $d\Omega_0$ is the solid angle for the unit ball, we obtain that

$$\lim_{\rho_0 \rightarrow \infty} \int_{\partial\Omega_{\rho_0}} \boldsymbol{\Psi}_i^T \partial_\rho \mathbf{W}_2|_{\rho=\rho_0} dS = \lim_{\rho_0 \rightarrow \infty} \int_{\partial\Omega_{\rho_0}} \frac{y_i^2}{\rho_0^2} b_{ji} d\Omega_0 = \frac{4\pi}{3} b_{ji}, \quad (4.15)$$

for each $i = 1, 2, 3$. In a similar way, we can calculate the second boundary integral in (4.12) as

$$\begin{aligned} - \lim_{\rho_0 \rightarrow \infty} \int_{\partial\Omega_{\rho_0}} \mathbf{W}_2^T \partial_\rho \boldsymbol{\Psi}_i|_{\rho=\rho_0} dS &= - \lim_{\rho_0 \rightarrow \infty} \int_{\partial\Omega_{\rho_0}} (\mathbf{b}_j \cdot \mathbf{y}) \partial_\rho \left[P_2(\rho) \frac{y_i}{\rho} \right] \Big|_{\rho=\rho_0} \rho_0^2 d\Omega_0, \\ &= - \lim_{\rho_0 \rightarrow \infty} \int_{\partial\Omega_{\rho_0}} (\mathbf{b}_j \cdot \mathbf{y}) \partial_\rho \left(\frac{y_i}{\rho^3} \right) \Big|_{\rho=\rho_0} \rho_0^2 d\Omega_0, \\ &= \lim_{\rho_0 \rightarrow \infty} \int_{\partial\Omega_{\rho_0}} (\mathbf{b}_j \cdot \mathbf{y}) \left(\frac{2y_i}{\rho^4} \right) \Big|_{\rho=\rho_0} \rho_0^2 d\Omega_0, \\ &= 2 \lim_{\rho_0 \rightarrow \infty} \int_{\partial\Omega_{\rho_0}} b_{ji} \frac{y_i^2}{\rho_0^2} \Big|_{\rho=\rho_0} d\Omega_0 = \frac{8\pi}{3} b_{ji}. \end{aligned} \quad (4.16)$$

By adding (4.15) and (4.16), we obtain that the right-hand side of (4.12) is $4\pi b_{ji}$. Finally, by equating this expression with that given in (4.14) for the left-hand side of (4.12), we obtain that $x'_{ji} = -3b_{ji}/\kappa_1$, where κ_1 is defined in (4.10). In vector form, with $i = 1, 2, 3$, we obtain (4.10). \blacksquare

By combining (4.10) with our expression for \mathbf{b}_j in (4.9b), we obtain an ODE-DAE system for the slow spot dynamics given by

$$\frac{d\mathbf{x}_j}{dt} = \frac{12\pi\varepsilon^3}{\kappa_1} \left(S_{j\varepsilon} \nabla_{\mathbf{x}} R(\mathbf{x}; \mathbf{x}_j)|_{\mathbf{x}=\mathbf{x}_j} + \sum_{\substack{i=1 \\ i \neq j}}^N S_{i\varepsilon} \nabla_{\mathbf{x}} G(\mathbf{x}; \mathbf{x}_i)|_{\mathbf{x}=\mathbf{x}_j} \right), \quad j = 1, \dots, N, \quad (4.17)$$

where $\kappa_1 = \kappa_1(S_{j\varepsilon})$ and $S_{1\varepsilon}, \dots, S_{N\varepsilon}$ are determined from the nonlinear algebraic system (4.7), which for $\varepsilon \ll 1$ depends weakly on the spot locations $\mathbf{x}_1, \dots, \mathbf{x}_N$. This ODE-DAE system is valid when the N -spot quasi-equilibrium pattern is linearly stable to either competition or peanut-splitting instabilities. Our numerical computations of κ_1 shown in the left panel of Fig. 4.2 reveal that $\kappa_1 < 0$ for $0 < S_j < \Sigma_2 \approx 20.16$.

Numerical realizations of the ODE-DAE system (4.17) and (4.7) are readily possible when Ω is the unit ball. In this special case, the Neumann Green's function and its

regular part can be given explicitly as

$$G(\mathbf{x}; \boldsymbol{\xi}) = \frac{1}{4\pi} \left(\frac{1}{|\mathbf{x} - \boldsymbol{\xi}|} + \frac{1}{|\boldsymbol{\xi}|} \frac{1}{|\mathbf{x} - \boldsymbol{\xi}'|} \right) - \frac{1}{4\pi} \log(\mathcal{T}) + \frac{1}{8\pi} |\mathbf{x}|^2 + h(\boldsymbol{\xi}),$$

$$\mathcal{T} \equiv (\boldsymbol{\xi}' - \mathbf{x}) \cdot \frac{\boldsymbol{\xi}}{|\boldsymbol{\xi}|} + |\boldsymbol{\xi}' - \mathbf{x}|, \quad (4.18)$$

for some $h(\boldsymbol{\xi})$, where $\boldsymbol{\xi}' \equiv \boldsymbol{\xi}/|\boldsymbol{\xi}|^2$. A simple calculation of the gradient, which is needed in (4.17), yields

$$\nabla_{\mathbf{x}} G(\mathbf{x}; \boldsymbol{\xi}) = -\frac{1}{4\pi} \left(\frac{\mathbf{x} - \boldsymbol{\xi}}{|\mathbf{x} - \boldsymbol{\xi}|^3} + \frac{1}{|\boldsymbol{\xi}|} \frac{\mathbf{x} - \boldsymbol{\xi}'}{|\mathbf{x} - \boldsymbol{\xi}'|^3} \right) + \frac{1}{4\pi\mathcal{T}} \left(\frac{\boldsymbol{\xi}}{|\boldsymbol{\xi}|} + \frac{\boldsymbol{\xi}' - \mathbf{x}}{|\mathbf{x} - \boldsymbol{\xi}'|} \right) + \frac{\mathbf{x}}{4\pi}, \quad (4.19a)$$

$$\nabla_{\mathbf{x}} R(\mathbf{x}; \boldsymbol{\xi}) = -\frac{1}{4\pi} \frac{1}{|\boldsymbol{\xi}|} \frac{\mathbf{x} - \boldsymbol{\xi}'}{|\mathbf{x} - \boldsymbol{\xi}'|^3} + \frac{1}{4\pi\mathcal{T}} \left(\frac{\boldsymbol{\xi}}{|\boldsymbol{\xi}|} + \frac{\boldsymbol{\xi}' - \mathbf{x}}{|\mathbf{x} - \boldsymbol{\xi}'|} \right) + \frac{\mathbf{x}}{4\pi}. \quad (4.19b)$$

For a particular parameter set, as described in the caption of the right panel of Fig. 4.2, we compare results from (4.17) for a 2-spot evolution in the ball with corresponding full numerical results computed from the PDE (4.1) using FlexPDE6 [107]. In our example, the two spots are initially taken to be in an antipodal configuration so that $\mathbf{e} = (1, 1)^T$ is an eigenvector of the Green's matrix \mathcal{G} . As a result, from (4.7), we have $S_{1\varepsilon} = S_{2\varepsilon} \equiv S_c = A/(6\sqrt{D})$. The results shown in the right panel of Fig. 4.2 show that the asymptotic result (4.17) is highly accurate in predicting the full dynamics. For this special configuration, we obtain from (4.17) and (4.19) that $\mathbf{x}_1 = (0, 0, z_0)$ and $\mathbf{x}_2 = -\mathbf{x}_1$ satisfies the explicit ODE

$$\frac{dz_0}{dt} = -\frac{3S_c\varepsilon^3}{|\kappa_1|} \mathcal{F}_2(z_0), \quad \mathcal{F}_2(z_0) \equiv \frac{2z_0^3(3 - z_0^4)}{(z_0^4 - 1)^2} + 2z_0 - \frac{1}{4z_0^2}. \quad (4.20)$$

It is readily verified that there is a unique root z_{0e} to $\mathcal{F}_2(z_0) = 0$ on $0 < z_0 < 1$, and using a root finder we get $z_{0e} \approx 0.42885$, which confirms the result shown in Fig. 4.2.

For an arbitrary initial configuration of spots, we recall from (4.7) that to leading order in ε we have $S_j = S_c + \mathcal{O}(\varepsilon)$, where S_c is $\frac{A|\Omega|}{4\pi N\sqrt{D}}$. Then, upon introducing the discrete energy $\mathcal{H}(\mathbf{x}_1, \dots, \mathbf{x}_N)$ defined by

$$\mathcal{H}(\mathbf{x}_1, \dots, \mathbf{x}_N) \equiv \sum_{i=1}^N R(\mathbf{x}_i; \mathbf{x}_i) + 2 \sum_{i=1}^N \sum_{j>i}^N G(\mathbf{x}_i; \mathbf{x}_j), \quad (4.21)$$

we can write (4.17) in the form of a gradient flow. The result is summarized as follows:

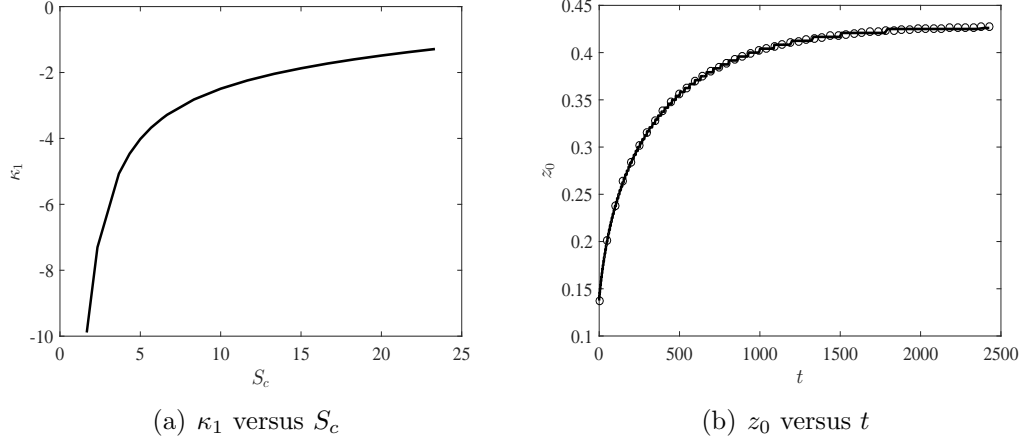


Figure 4.2: Left panel: κ_1 versus S_c computed numerically from (4.10), which shows that $\kappa_1 < 0$ for $0 < S_c < \Sigma_2 \approx 20.16$. Right panel: plot of the z -coordinate $z_0(t) > 0$ of two antipodal spots initially located at $(0, 0, \pm 0.1375)$. The other spot evolves as $-z_0(t)$. The solid curve is obtained from numerically solving the full Schnakenberg model (4.1) in the unit ball, while the circles are obtained from numerically solving the ODE (4.20), as derived from (4.17), with $S_{1\varepsilon} = S_{2\varepsilon} = A/(6\sqrt{D})$. The parameters are $D = 1$, $A = 80$, and $\varepsilon = 0.02$. For this parameter set, where $S_{1\varepsilon} \approx 13.33$, we get $\kappa_1 = -2.0395$.

Main Result 4.1.2 *Let $\varepsilon \rightarrow 0$, and suppose that the N -spot quasi-equilibrium solution of (4.1) is linearly stable on an $\mathcal{O}(1)$ time-scale to either competition or peanut-splitting instabilities. Then, to leading order in ε , the collection of spots evolve by the gradient flow*

$$\frac{d\mathbf{x}_j}{dt} = -\frac{6\pi\varepsilon^3 S_c}{|\kappa_1|} \nabla_{\mathbf{x}_j} \mathcal{H}(\mathbf{x}_1, \dots, \mathbf{x}_N), \quad j = 1, \dots, N; \quad S_c = \frac{A|\Omega|}{4\pi N\sqrt{D}}, \quad (4.22)$$

where the discrete energy \mathcal{H} is defined in (4.21). Here $\kappa_1 = \kappa_1(S_c)$ is defined in (4.10). In terms of the spatial configuration $\{\mathbf{x}_1, \dots, \mathbf{x}_N\}$ of spots, a two-term expansion for the spot strengths when $\mu'_0(S_c) \neq 0$ is

$$S_{j\varepsilon} \sim S_c + \frac{4\pi\varepsilon S_c}{\mu'_0(S_c)} \left(\frac{\mathbf{e}^T \mathcal{G} \mathbf{e}}{N} - (\mathcal{G} \mathbf{e})_j \right) + \dots, \quad j = 1, \dots, N, \quad (4.23)$$

where $\mathbf{e} = (1, \dots, 1)^T$ and \mathcal{G} is the Neumann Green's matrix.

We now use (4.22) to discuss possible steady-state spot configurations. It follows from (4.22) that spatial configurations of steady-state spots are critical points of the discrete energy \mathcal{H} , and that patterns that are linearly stable with respect to the ODE

dynamics (4.22) are minima of \mathcal{H} . The discrete energy \mathcal{H} also arises in the analysis of the mean first passage time for a Brownian walk in a 3-D domain with small localized spherical traps (cf. [108]). Following the decomposition in [108], we define \mathcal{H}_0 by

$$\mathcal{H}(\mathbf{x}_1, \dots, \mathbf{x}_N) = \frac{\mathcal{H}_0}{4\pi} - \frac{7N^2}{10\pi},$$

$$\mathcal{H}_0 \equiv 4\pi \left[\sum_{i=1}^N \left(R(\mathbf{x}_i; \mathbf{x}_i) + \frac{7}{10\pi} \right) + 2 \sum_{i=1}^N \sum_{j>i}^N \left(G(\mathbf{x}_i; \mathbf{x}_j) + \frac{7}{10\pi} \right) \right]. \quad (4.24)$$

For the unit ball, in Table 4.1 we give some results for $N = 2, \dots, 20$ computed in [108] using numerical optimization software for a restricted optimization problem whereby \mathcal{H}_0 is minimized subject to the condition that either all N spots must be on a single ring (second and third columns), or all $N - 1$ points are on a single ring while the remaining spot is at the origin (fourth and fifth columns). From this table we observe for $N \geq 16$ that the second class of patterns gives a smaller \mathcal{H}_0 . It was found in [108] that, for $N = 2, \dots, 20$, an unrestricted optimization of \mathcal{H}_0 gives results that coincide to the number of digits shown with the restricted minimum energies in Table 4.1, with all spots being very close to, but not exactly on, a common ring of radius r_c . As a result, for $N = 2, \dots, 20$, the global minimum of \mathcal{H}_0 can be predicted rather accurately from the restricted optimization results in Table 4.1.

Point configurations corresponding to such global minima of \mathcal{H}_0 are linearly stable equilibria of the ODE dynamics (4.22). We then perform numerical simulations of (4.22) with randomly generated initial conditions in an attempt to classify steady-states of (4.22) with large basins of attraction of initial conditions. We find for $N = 2, 3, 4, 6, 8$ that the computed steady-state solutions agree precisely with those for the one-ring patterns shown in the second and third columns in Table 4.1 and that, for these values of N , $\mathbf{e} = (1, \dots, 1)^T$ is an eigenvector of the Green's matrix \mathcal{G} at the steady-state. In particular, for $N = 2$, the first row of Table 4.1 predicts that a two-spot steady-state of (4.22) will correspond to antipodal spots on an interior ball of radius $r_c \approx 0.429$, which is precisely what was observed in the results shown in the right panel of Fig. 4.2. Moreover, our numerical results show for $N = 12$ that some initial conditions lead for (4.22) lead to a steady-state where the spots are centered at the vertices of an icosahedron with discrete energy and radius given in Table 4.1, for which \mathbf{e} is an eigenvector of \mathcal{G} , while other initial conditions lead to a pattern with 11 spots nearly on a common ring with a spot at the center. For $N = 13, 14, 15$, initial conditions lead

N	$\mathcal{H}_0^{(a)}$	Spherical radii $r_j = r_c \forall j$	$\mathcal{H}_0^{(b)}$	Spherical radii $r_j = r_c \forall j, (r_1 = 0)$
2	7.2763	0.429	9.0316	0.563
3	18.5047	0.516	20.3664	0.601
4	34.5635	0.564	36.8817	0.626
5	56.2187	0.595	58.1823	0.645
6	82.6490	0.618	85.0825	0.659
7	115.016	0.639	116.718	0.671
8	152.349	0.648	154.311	0.680
9	195.131	0.659	196.843	0.688
10	243.373	0.668	244.824	0.694
11	297.282	0.676	297.283	0.700
12	355.920	0.683	357.371	0.705
13	420.950	0.689	421.186	0.710
14	491.011	0.694	491.415	0.713
15	566.649	0.698	566.664	0.717
16	647.738	0.702	647.489	0.720
17	734.344	0.706	733.765	0.722
18	826.459	0.709	825.556	0.725
19	924.360	0.712	922.855	0.727
20	1027.379	0.715	1025.94	0.729

Table 4.1: Numerically computed minimal values of the discrete energy function \mathcal{H}_0 for the optimal arrangement of N -traps within a unit ball where the optimization is restricted to a one-ring configuration $\mathcal{H}_0^{(a)}$, or to a one-ring configuration with a center spot $\mathcal{H}_0^{(b)}$ (see [108]). The minimum of these two values is shown in bold face. The unrestricted optimization of \mathcal{H}_0 gives results extremely close to the restricted minimum energies in Table 4.1, but that not all spots lie exactly on a ring of a common radius.

either to spots nearly on a common ring or to the near-ring and center-hole pattern. For $N = 16, \dots, 20$ our computations of (4.22) lead typically to the near-ring and center-hole pattern. For $N = 12, \dots, 20$, we find that the discrete energies at the steady-state coincide very closely with the restricted optimization results in Table 4.1. For $N = 5$, our simulations of (4.22) with random initial conditions, shows that (4.22) converges to a steady-state with 2 antipodal spots at a distance of 0.59279 from the origin, and with 3 spots equally-spaced on a mid-plane with spots being at a distance 0.59605 from the origin.

4.1.1 Spot Dynamics with a Spatially Varying Feed-Rate

In this subsection we extend our previous analysis of (4.1) to the case where the feed-rate A depends on \mathbf{x} , with $A(\mathbf{x}) > 0$ in Ω . We only briefly highlight the new features of the analysis needed when $A = A(\mathbf{x})$.

Since the inner solution near each spot does not depend on A , we can allow the source strength S_j to depend weakly on ε , and so we write $U_{j\varepsilon}, V_{j\varepsilon}$ to be the solution to (4.3) for which $U_{j\varepsilon} \sim \mu_j - S_{j\varepsilon}/\rho$ as $\rho \rightarrow \infty$, where $\mu_j \equiv \mu_0(S_{j\varepsilon})$. In place of (4.4), the outer solution now satisfies

$$\Delta u \sim -\frac{\varepsilon A(\mathbf{x})}{D} + \frac{4\pi\varepsilon}{\sqrt{D}} \sum_{j=1}^N S_{j\varepsilon} \delta(\mathbf{x} - \mathbf{x}_j), \quad \mathbf{x} \in \Omega; \quad \partial_n u = 0, \quad \mathbf{x} \in \partial\Omega. \quad (4.25)$$

By the divergence theorem, we obtain that

$$\sum_{i=1}^N S_{i\varepsilon} = \frac{\bar{A}|\Omega|}{4\pi\sqrt{D}}, \quad \bar{A} \equiv \frac{1}{|\Omega|} \int_{\Omega} A(\mathbf{x}) d\mathbf{x}. \quad (4.26)$$

The exact solution to (4.25) is simply

$$u = \xi + \frac{\varepsilon}{D} u_{1p}(\mathbf{x}) - \frac{4\pi\varepsilon}{\sqrt{D}} \sum_{i=1}^N S_{i\varepsilon} G(\mathbf{x}; \mathbf{x}_i), \quad (4.27)$$

where ξ is a constant, G is the Neumann Green's function of (4.5), and $u_{1p}(\mathbf{x})$ is the unique solution to

$$\Delta u_{1p} = -A(\mathbf{x}) + \bar{A}, \quad \mathbf{x} \in \Omega; \quad \partial_n u_{1p} = 0, \quad \mathbf{x} \in \partial\Omega; \quad \int_{\Omega} u_{1p} d\mathbf{x} = 0, \quad (4.28)$$

which is given explicitly by

$$u_{1p}(\mathbf{x}) = \int_{\Omega} G(\boldsymbol{\xi}; \mathbf{x}) A(\boldsymbol{\xi}) d\boldsymbol{\xi}. \quad (4.29)$$

By expanding (4.27) as $\mathbf{x} \rightarrow \mathbf{x}_j$ we obtain in terms of inner variables that

$$u \sim \xi - \frac{S_j \varepsilon}{\sqrt{D} \rho} + \frac{\varepsilon}{D} u_{1p}(\mathbf{x}_j) - \frac{4\pi \varepsilon}{\sqrt{D}} (\mathcal{G}\mathbf{S})_j + \frac{\varepsilon^2}{\sqrt{D}} \mathbf{y} \cdot \tilde{\mathbf{b}}_j + \dots, \quad \text{as } \mathbf{x} \rightarrow \mathbf{x}_j, \quad (4.30)$$

where \mathcal{G} is the Neumann Green's matrix, $\mathbf{S} \equiv (S_{1\varepsilon}, \dots, S_{N\varepsilon})^T$, and where we have defined $\tilde{\mathbf{b}}_j$ by

$$\tilde{\mathbf{b}}_j \equiv \frac{1}{\sqrt{D}} \nabla_{\mathbf{x}} u_{1p}|_{\mathbf{x}=\mathbf{x}_j} - 4\pi \left(S_{j\varepsilon} \nabla_{\mathbf{x}} R(\mathbf{x}; \mathbf{x}_j)|_{\mathbf{x}=\mathbf{x}_j} + \sum_{\substack{i=1 \\ i \neq j}}^N S_{i\varepsilon} \nabla_{\mathbf{x}} G(\mathbf{x}; \mathbf{x}_i)|_{\mathbf{x}=\mathbf{x}_j} \right). \quad (4.31)$$

Upon matching (4.30) to the far-field behavior of the j -th inner solution defined in (4.2) we obtain, in place of (4.7), that $S_{j\varepsilon}$, for $j = 1, \dots, N$, and ξ now satisfy

$$\begin{aligned} \xi - \frac{4\pi \varepsilon}{\sqrt{D}} (\mathcal{G}\mathbf{S})_j + \frac{\varepsilon}{D} u_{1p}(\mathbf{x}_j) &= \frac{\mu_0(S_{j\varepsilon})}{\sqrt{D}}, \quad j = 1, \dots, N; \\ \sum_{j=1}^N S_{j\varepsilon} &= \frac{\bar{A}|\Omega|}{4\pi\sqrt{D}}, \end{aligned} \quad (4.32)$$

where the graph of $\mu_0(S_{j\varepsilon})$ versus $S_{j\varepsilon}$ was shown in Fig. 4.1(a). In addition, we obtain that $\mathbf{W}_2 = (V_{j2}, U_{j2})^T$ now satisfies (4.9) with \mathbf{b}_j replaced by $\tilde{\mathbf{b}}_j$. Therefore, by using Lemma 4.1.1 we can determine the slow spot dynamics in terms of $\tilde{\mathbf{b}}_j$. This yields, in place of (4.17), that the ODE-DAE system for the slow spot dynamics when $A = A(\mathbf{x})$

$$\frac{d\mathbf{x}_j}{dt} = -\frac{\varepsilon^3}{\kappa_1} \left[\frac{3}{\sqrt{D}} \nabla_{\mathbf{x}} u_{1p}|_{\mathbf{x}=\mathbf{x}_j} - 12\pi \left(S_{j\varepsilon} \nabla_{\mathbf{x}} R(\mathbf{x}; \mathbf{x}_j)|_{\mathbf{x}=\mathbf{x}_j} + \sum_{\substack{i=1 \\ i \neq j}}^N S_{i\varepsilon} \nabla_{\mathbf{x}} G(\mathbf{x}; \mathbf{x}_i)|_{\mathbf{x}=\mathbf{x}_j} \right) \right] \quad (4.33)$$

where $S_{1\varepsilon}, \dots, S_{N\varepsilon}$ are now determined from the nonlinear algebraic system (4.32), and $\kappa_1 = \kappa_1(S_{j\varepsilon}) < 0$ from Fig. 4.2(a). Finally, upon making the leading-order approximation $S_j = S_c + \mathcal{O}(\varepsilon)$, for $j = 1, \dots, N$, where

$$S_c = \frac{\bar{A}|\Omega|}{4\pi N\sqrt{D}}, \quad (4.34)$$

we can readily reduce (4.33) to the following simple result:

Main Result 4.1.3 *Let $\varepsilon \rightarrow 0$, and suppose that the N -spot quasi-equilibrium solution of (4.1) with $A = A(\mathbf{x}) > 0$ is linearly stable on an $\mathcal{O}(1)$ time-scale to either competition or peanut-splitting instabilities. Then, to leading order in ε , for*

$j = 1, \dots, N$, the slow time evolution of the collection of spots satisfies

$$\frac{d\mathbf{x}_j}{dt} = -\frac{12\pi S_c \varepsilon^3}{|\kappa_1|} \left(\nabla_{\mathbf{x}} R(\mathbf{x}; \mathbf{x}_j)|_{\mathbf{x}=\mathbf{x}_j} + \sum_{\substack{i=1 \\ i \neq j}}^N \nabla_{\mathbf{x}} G(\mathbf{x}; \mathbf{x}_i)|_{\mathbf{x}=\mathbf{x}_j} - \frac{N}{A|\Omega|} \nabla_{\mathbf{x}} u_{1p}|_{\mathbf{x}=\mathbf{x}_j} \right) \quad (4.35)$$

where S_c is given in (4.34). In term of the discrete energy \mathcal{H} of (4.21), we have equivalently that

$$\frac{d\mathbf{x}_j}{dt} = -\frac{6\pi S_c \varepsilon^3}{|\kappa_1|} \left(\nabla_{\mathbf{x}_j} \mathcal{H}(\mathbf{x}_1, \dots, \mathbf{x}_N) - \frac{2N}{A|\Omega|} \nabla_{\mathbf{x}} u_{1p}|_{\mathbf{x}=\mathbf{x}_j} \right) \quad (4.36)$$

where u_{1p} , which satisfies (4.28), is given explicitly in (4.29). Here $\kappa_1 = \kappa_1(S_c) < 0$ is defined in (4.10) (see Fig. 4.2(a)). In terms of the spatial configuration $\{\mathbf{x}_1, \dots, \mathbf{x}_N\}$ of spots, a two-term expansion for the source strengths when $\mu'_0(S_c) \neq 0$, as obtained from (4.32), is

$$S_{j\varepsilon} \sim S_c + \frac{4\pi\varepsilon S_c}{\mu'_0(S_c)} \left(\frac{\mathbf{e}^T \mathcal{G} \mathbf{e}}{N} - (\mathcal{G} \mathbf{e})_j \right) + \frac{\varepsilon}{\sqrt{D} \mu'_0(S_c)} \left(u_{1p}(\mathbf{x}_j) - \frac{1}{N} \sum_{i=1}^N u_{1p}(\mathbf{x}_i) \right) \quad (4.37)$$

where $\mathbf{e} = (1, \dots, 1)^T$ and \mathcal{G} is the Neumann Green's matrix.

We now illustrate Main Result 4.1.3 for a few choices of the variable feed A in the unit ball.

Example 1: (Radially Symmetric Feed-Rate: $A = A(r)$)

We first use (4.35) to derive an ODE for a one-spot solution centered at $\mathbf{x}_1 = (r, 0, 0)$ along the positive x axis inside a unit ball when the feed-rate A is purely radial, i.e. $A = A(r)$. We use $S_c = \bar{A}/(3\sqrt{D})$ from (4.34), together with (4.19) and the solution u_{1p} to (4.28), to readily obtain that (4.35) reduces to

$$\frac{dr}{dt} = -\frac{\bar{A}\varepsilon^3}{\sqrt{D}|\kappa_1|} \mathcal{F}_{1a}(r), \quad \text{where} \quad \mathcal{F}_{1a}(r) \equiv \frac{r(2-r^2)}{(1-r^2)^2} + \frac{3}{\bar{A}r^2} \int_0^r A(\rho) \rho^2 d\rho, \quad (4.38)$$

and $\bar{A} = 3 \int_0^1 \rho^2 A(\rho) d\rho$. Since $\mathcal{F}_{1a}(0) = 0$, then $r = 0$ is always an equilibrium point. Moreover, since $\mathcal{F}_{1a}(r) \sim r [2 + A(0)/\bar{A}] > 0$ as $r \rightarrow 0$, it follows that $r = 0$ is a stable equilibrium point of the ODE (4.38) for any $A(r) > 0$. Finally, since $\mathcal{F}_{1a}(r) > 0$ on $0 < r < 1$, we conclude that there is no radially symmetric feed-rate that can lead to the pinning of a spot at some distance r_e , with $0 < r_e < 1$, from the origin.

Next, we consider a two-spot pattern in a spherical domain where the spots are symmetrically placed at $\mathbf{x}_1 = (r, 0, 0)$ and $\mathbf{x}_2 = -\mathbf{x}_1$ with $0 < r < 1$. Assume that

$A = A(r) > 0$. We use $S_c = \bar{A}/(6\sqrt{D})$ from (4.34), together with (4.19) and the solution u_{1p} to (4.28), to readily obtain that (4.35) reduces to

$$\frac{dr}{dt} = -\frac{3S_c\varepsilon^3}{|\kappa_1|}\mathcal{F}_{2a}(r), \quad \mathcal{F}_{2a}(r) \equiv \frac{2r^3(3-r^4)}{(r^4-1)^2} + r - \frac{1}{4r^2} + \frac{3}{r^2\bar{A}} \int_0^r A\rho^2 d\rho, \quad (4.39)$$

where $\bar{A} = 3 \int_0^1 \rho^2 A(\rho) d\rho$. Any steady-state r_{0e} of (4.39) must satisfy

$$\frac{2r^5(3-r^4)}{(r^4-1)^2} + \frac{\int_0^r \rho^2 A(\rho) d\rho}{\int_0^1 \rho^2 A(\rho) d\rho} = \frac{1}{4} - r^3. \quad (4.40)$$

The left-hand side of (4.40) is monotone increasing, is zero at $r = 0$ and is unbounded as $r \rightarrow 1^-$. Since the right-hand side is monotone decreasing on $0 < r < 1$ and has a unique sign change at $r = 4^{-1/3}$, it follows that there is a unique steady-state solution r_{0e} to (4.39) on $0 < r_{0e} < 4^{-1/3}$ for any $A(\rho) > 0$. Therefore, the effect of the radially symmetric feed-rate is simply to modify the location of the steady-state observed in Fig. 4.2 for the case where A was constant.

Example 2: (Pinning of a Spot)

We consider a one-spot solution and take $A(\mathbf{x}) = A_0 + Bz$ with $0 < B < A_0$, where $\mathbf{x} = (x, y, z)^T$. For this case, $\bar{A} = A_0$, and we calculate from (4.28) that

$$u_{1p}(\mathbf{x}) = \frac{Bz}{10} (3 - |\mathbf{x}|^2), \quad \nabla_{\mathbf{x}} u_{1p}(\mathbf{x}) = \frac{B}{10} (-2xz, -2yz, 3 - |\mathbf{x}|^2 - 2z^2)^T. \quad (4.41)$$

We obtain from (4.19b) that

$$\nabla_{\mathbf{x}} R(\mathbf{x}; \mathbf{x}_1)|_{\mathbf{x}=\mathbf{x}_1} = \frac{\mathbf{x}_1}{4\pi} \left[\frac{2-r^2}{(1-r^2)^2} + 1 \right], \quad (4.42)$$

so that (4.35) with $N = 1$ and u_{1p} as in (4.41) yield that

$$\frac{d\mathbf{x}_1}{dt} = -\frac{3\varepsilon^3 S_1}{|\kappa_1|} \left[\mathbf{x}_1 \left(\frac{(2-r^2)}{(1-r^2)^2} + 1 \right) + \frac{3B}{10A_0} (2x_1z_1, 2y_1z_1, -3 + r^2 + 2z_1^2)^T \right], \quad (4.43)$$

where $r = |\mathbf{x}_1|$ and $S_1 = A_0/(3\sqrt{D})$. The steady-state for (4.43) is $x_{1e} = y_{1e} = 0$, and where $z_{1e} = r_e$ is the unique root on $0 < r_e < 1$ of

$$r \left(\frac{(2-r^2)}{(1-r^2)^2} + 1 \right) = \frac{9B}{10A_0}(1-r^2), \quad (4.44)$$

which can be found numerically. In particular, if $A_0 = 40$ and $B = 20$ so that $A(\mathbf{x}) = 40(1 + z/2)$, the unique equilibrium point is $(x_{1e}, y_{1e}, z_{1e})^T = (0, 0, 0.14387)^T$.

Therefore, in this case we predict that the variable feed-rate leads to an equilibrium spot solution on the positive z axis in the direction where the feed is largest. For $\varepsilon = 0.03$ and the initial location $\mathbf{x}_1(0) = (0.4, 0.5, 0.3)^T$, this is confirmed in Fig. 4.3(a) from a FlexPDE6 [107] full numerical computation of (4.1). We remark that the full numerical results in Fig. 4.3(a) compare very favorably with results from the ODE (4.43).

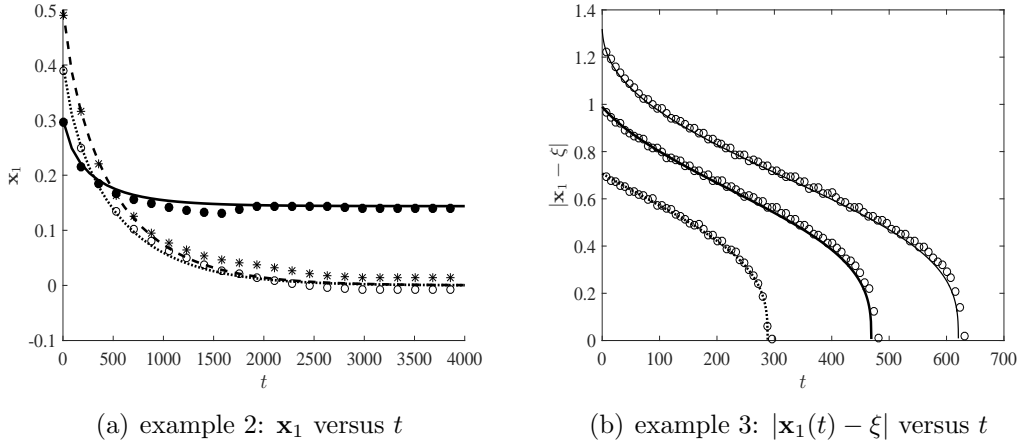


Figure 4.3: Left panel: Plot of the full numerical results (discrete points) computed from (4.1) using FlexPDE6 [107] for the three components of the spot trajectory \mathbf{x}_1 versus t for example 2 where $A(\mathbf{x}) = 40 + 20z$, $D = 1$, $\varepsilon = 0.03$, and with initial condition $\mathbf{x}_1(0) = (0.4, 0.5, 0.3)^T$. The three curves are the asymptotic result (4.43) with the labels x (dotted), y (dashed), and z (solid), where $\mathbf{x}_1 = (x, y, z)^T$. The results confirm that $\mathbf{x}_1 \rightarrow (0, 0, 0.14387)^T$ as $t \rightarrow \infty$. Right panel: numerical solution of the ODE (4.46) (solid curve) for example 3 where $A(\mathbf{x})$ is given in (4.45) with $D = 1$ and $\varepsilon = 0.03$. The discrete points are full numerical results computed from (4.1) using FlexPDE6 [107]. The parameters are $A_0 = 20$ and $B = 20|\Omega|$, with $|\Omega| = 4\pi/3$. The localized feed is at $\xi = (0, 0, 0.5)$, and we plot the distance $|\mathbf{x}_1(t) - \xi|$ versus t for three initial conditions: $\mathbf{x}_1(0) = (0, 0.7, -0.2)^T$ (heavy solid curve), $\mathbf{x}_1(0) = (-0.7, -0.2, -0.6)^T$ (solid curve), and $\mathbf{x}_1 = (-0.5, 0.0, 0.0)^T$ (dotted curve).

Example 3: (Pinning of a Spot by a Localized Source of Feed)

Finally, we consider one-spot dynamics for the case where the variable feed-rate has a background state that is augmented by a localized source where the feed is large. As a model for this situation we take

$$A(\mathbf{x}) = A_0 + B\delta(\mathbf{x} - \xi), \quad (4.45)$$

where $A_0 > 0$, $B > 0$, and $\boldsymbol{\xi} \in \Omega$. We calculate $\bar{A} = A_0 + B/|\Omega|$, and the solution to (4.28) is $u_{1p}(\mathbf{x}) = BG(\mathbf{x}; \boldsymbol{\xi})$. From (4.35) and (4.19), we obtain that the one-spot dynamics is

$$\frac{d\mathbf{x}_1}{dt} = -\frac{3\varepsilon^3 S_1}{|\kappa_1|} \left[\mathbf{x}_1 \left(\frac{(2-r^2)}{(1-r^2)^2} + 1 \right) - \frac{3B}{A_0 + B/|\Omega|} \nabla_{\mathbf{x}} G(\mathbf{x}; \boldsymbol{\xi})|_{\mathbf{x}=\mathbf{x}_1} \right], \quad (4.46)$$

with $S_1 = (A_0 + B/|\Omega|)/(3\sqrt{D})$, and where $\nabla_{\mathbf{x}} G(\mathbf{x}; \boldsymbol{\xi})|_{\mathbf{x}=\mathbf{x}_1}$ can be calculated from (4.19a). Due to the $1/r$ singularity in G , it follows from (4.46) that if the initial point $\mathbf{x}_1(0)$ is sufficiently close to the source $\boldsymbol{\xi}$ of the feed, then we claim that $\mathbf{x}_1(T) = \boldsymbol{\xi}$ at some $t = T < \infty$. To see this, we observe from (4.46) and (4.19a) that for \mathbf{x}_1 near $\boldsymbol{\xi}$, we have $d\mathbf{x}_1/dt \sim -c(\mathbf{x}_1 - \boldsymbol{\xi})/|\mathbf{x}_1 - \boldsymbol{\xi}|^3$ for some $c > 0$, which implies that $|\mathbf{x}_1 - \boldsymbol{\xi}| \sim (3c)^{1/3}(T - t)^{1/3}$ for t near T .

This finite-time pinning phenomena is shown in Fig. 4.3(b) where we plot the distance $|\mathbf{x}_1(t) - \boldsymbol{\xi}|$ versus t for a one-spot solution in the unit ball for the parameter set $A_0 = 20$, $B = 20|\Omega|$, $D = 1$, and $\varepsilon = 0.03$. In this figure we show a very favorable comparison between results computed from the asymptotic ODE (4.46) and the full numerical solution to (4.1) using FlexPDE6 [107] for three different initial conditions $\mathbf{x}_1(0)$. When using FlexPDE6 on (4.1) for $A(\mathbf{x})$ given in (4.45), we mollified the delta singularity by using the following 3-D Gaussian approximation with $\sigma = 0.005$:

$$A(\mathbf{x}) = A_0 + BF(|\mathbf{x} - \boldsymbol{\xi}|), \quad \text{where} \quad F(|\mathbf{x} - \boldsymbol{\xi}|) \equiv (\pi\sigma)^{-3/2} \exp(-\sigma^{-1}|\mathbf{x} - \boldsymbol{\xi}|^2).$$

4.2 Discussion

We have developed a hybrid asymptotic-numerical approach to analyze the slow dynamics of quasi-equilibrium N -spot patterns for the singularly perturbed 3-D Schnakenberg model (4.1) in the limit $\varepsilon \rightarrow 0$. In terms of the original model, such patterns occur in the large diffusivity regime $\mathcal{D} = \mathcal{O}(\varepsilon^{-4})$. Our hybrid asymptotic-numerical framework characterizing the slow spot dynamics was implemented numerically for some spot patterns in the unit ball. Our asymptotic predictions for the slow spot dynamics were shown to compare very favorably with results obtained from full numerical simulations of the 3-D Schnakenberg model (4.1) using FlexPDE6 [107].

We now briefly discuss a few open problems that warrant further study. Our implementation of slow spot dynamics was done only for the case where Ω is the

unit ball, for which there is an explicit analytical formula for the Neumann Green's function and its regular part. To leading-order in ε , the slow ODE dynamics in (4.22) for a spatially uniform feed A , and in (4.36) for a variable feed $A(\mathbf{x})$, depend on the gradient of this Neumann Green's function. For more complicated domains, it would be interesting to implement the explicit ODE dynamics numerically by using fast multipole methods (cf. [109]) to compute the required Green's function both accurately and rapidly. Such fast multipole methods would be highly advantageous in this setting, since in simulating the ODE dynamics in (4.22) or (4.36) the gradients of the Green's function must be evaluated at each discrete point of the discretization of the ODE dynamics. With this approach it should be tractable to numerically study spot-dynamics and, in particular, spot-pinning effects due to either changes in the domain geometry or spatial variations in the variable feed-rate $A(\mathbf{x})$.

For the case where $A > 0$ is constant, a second open problem is to identify stable equilibria of the leading-order ODE dynamics (4.22) that have large basins of attraction for initial conditions. As N increases, the energy landscape of the discrete energy \mathcal{H} in (4.21) will have an increasingly large number of local minima with nearly the same energy (cf. [108] and the references therein). These local minima are all linearly stable equilibrium points of (4.22). A natural question is to study, as N increases, whether most initial conditions for (4.22) tend to the global minimum point of \mathcal{H} . Our computations of (4.22) for random configurations of spots have suggested that this property holds $N = 2, \dots, 20$. For the unit ball, the global minimum of \mathcal{H} for $N = 2, \dots, 20$ was computed using numerical optimization software in [108], but it becomes computationally much more challenging to compute it for larger N . Therefore, in what sense can the ODE system (4.22) be used as a regularization for computing the global minimum point of \mathcal{H} ? From a numerical analysis viewpoint, a related ODE regularization was used in [110] to compute a minimum energy configuration for 2-D Coulomb particles on the surface of a ball. We remark that the identification of the global minimum point of \mathcal{H} also arises in other contexts. In particular, it corresponds to the spatial configuration of the centers of small traps that minimize the average mean first passage time for a Brownian walker in a 3-D domain [108] that has a uniformly distributed starting point in the domain.

Finally, we remark that it should be possible to develop a similar hybrid asymptotic-numerical approach to study localized quasi-equilibrium spot patterns in a 3-D setting for other well-known singularly perturbed RD systems, such as the Gierer-Meinhardt, Gray-Scott, and Brusselator models.

Chapter 5

Multi-vortex Crystal Lattices in Bose-Einstein Condensates with a Rotating Trap

The results of this chapter have been submitted for publication [111]. Our starting point is the Gross-Pitaevskii equation with an inhomogeneous rotating trap in two dimensions given by

$$(\gamma - \kappa i)w_t = \Delta w + \frac{1}{\varepsilon^2} (V(x) - |w|^2) w + i\Omega (x_2 w_{x_1} - x_1 w_{x_2}) \quad (5.1a)$$

The parameter ε is assumed to be small, which corresponds to the large chemical potential limit. Ω is the rotation rate, and $V(x)$ is the trap potential. We consider the general anisotropic parabolic potential $V(x)$,

$$V(x) = 1 - x_1^2 - b^2 x_2^2 \quad (5.1b)$$

The parameter b represents the strength of the anisotropy, with isotropic trap corresponding to $b = 1$. Finally, the ratio γ/κ represents the finite temperature effects [112, 113]. For the purposes of numerical simulations, we mostly work in the overdamped regime $\gamma/\kappa \rightarrow \infty$, sometimes referred to as imaginary time integration [113, 114]. While the equilibrium vortex lattice state is independent of γ , numerical simulations are easier to perform in the overdamped regime.

Let us now summarize the main findings of this chapter.

1. **Reduced equations for vortex motion.** In §5.1 and §5.1.2 we extend the asymptotic methods first developed in [22] to the case of nonconstant rotating trap. The presence of the inhomogeneous trap introduces several complications. The end-result is the the following system for the motion of N vortices whose

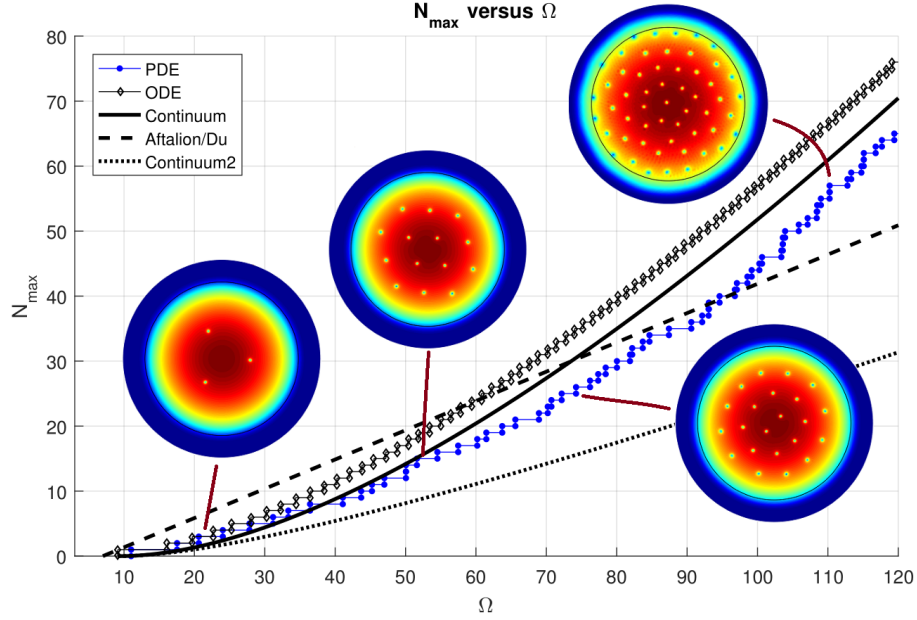


Figure 5.1: N_{\max} as a function of Ω . “PDE” denotes the full PDE simulation (5.1) with $b = 1, \varepsilon = 0.01, \kappa = 0, \gamma = 1$. We start with $\Omega = 125$ and an initial configuration of 80 vortices. Then Ω is gradually decreased in time according to the formula $\Omega = 140 - 10^{-4}t$. We count the number of vortices at each value of Ω , and this is what is plotted. “ODE” denotes the simulation of the reduced ODE system (5.2), with the same parameters as PDE. “Continuum” refers to formula (5.4). “Aftalion/Du” is the formula (5.44) originally derived in [115]. Finally, “Continuum2” is formula (5.46) first derived in [116].

positions are given by $\xi_j, j = 1 \dots N$:

$$\gamma \log(1/\varepsilon) \xi_{jt} + \kappa \xi_{jt}^\perp = \left(-\frac{2\Omega}{1+b^2} + \frac{2 \log(1/\varepsilon)}{V(\xi_j)} \right) \begin{pmatrix} 1 & 0 \\ 0 & b^2 \end{pmatrix} \xi_j + 2 \sum_{k \neq j} \frac{(\xi_j - \xi_k) V(\xi_j)}{|\xi_j - \xi_k|^2 V(\xi_k)}. \quad (5.2)$$

Here and below, we use the notation $(a, b)^\perp = (-b, a)$.

We draw the reader’s attention to the term $\frac{V(\xi_j)}{V(\xi_k)}$ which modifies the “classical” Helmholtz-type vortex-to-vortex interaction of the form $\xi_{jt}^\perp = \sum_{k \neq j} \frac{(\xi_j - \xi_k)}{|\xi_j - \xi_k|^2}$ (equation (5.2) reduces to the “classical” case when $V = 1, \gamma = 0$ and $\Omega = 0$, corresponding to a constant trap, no rotation, and no damping). To our knowledge, this is the first time that this additional term has been proposed. In [116, 117] the same equation as (5.2) but without the term $\frac{V(\xi_j)}{V(\xi_k)}$ was used to

describe vortex dynamics in BEC. We show that our modified equation (5.2) agrees with full numerical simulations of the original GPE (5.1a) much better, particularly in the case of multiple vortices; see figures 5.1, 5.2.

The remaining results in the paper follow from the analysis of the reduced equation (5.2).

2. **Large- N vortex lattice density and radius for isotropic potential.** Here, we extend the methods reported in [116] to derive the continuum limit density for the steady state of (5.2). In §5.2 we show that in the large- N limit, the radius a of the vortex lattice is related to Ω, N, ε via the formula

$$N \sim \frac{1}{\nu} \left(\left(-1 - \frac{1}{2} \Omega \nu \right) \ln(1 - a^2) + 2 - 2(1 - a^2)^{-1} \right), \quad N \gg 1 \quad (5.3)$$

where $\nu = 1/\log(1/\varepsilon)$. See figure 5.2, where the asymptotic radius a given by solving (5.3) is shown in dashed curve, and a good agreement with full numerics is observed.

3. **Maximal admissible number of vortices.** As we show in §5.2, an immediate consequence of (5.3) is the existence of a fold-point bifurcation which results in the disappearance of some vortices as Ω is decreased, as illustrated in figure 5.1. Stated differently, for a fixed Ω , there is a maximum N_{\max} such that N -vortex lattice exists if and only if $N \leq N_{\max}$ where

$$N_{\max} = \frac{1}{\nu} \left\{ (\Omega \nu + 2) \left(\frac{1}{2} \ln(\Omega \nu + 2) - \ln(2) - \frac{1}{2} \right) + 2 \right\}. \quad (5.4)$$

Figure 5.1 illustrates this result.

4. **Stability of two vortices in the anisotropic case.** In §5.3 we study the stability of a two-vortex steady state with respect to the ODE dynamics of (5.50). By symmetry, there are two equilibria states: the two vortices lying on major or minor axis. However the equilibrium along the minor axis is unstable. Furthermore, a two vortex-state on a the major axis becomes unstable as Ω is decreased due to a fold point bifurcation. We compute this bifurcation and compare this to numerics. In paper [115] a similar threshold was computed for the anisotropic case from the energy point of view.

5. **High anisotropy, large N limit (§5.4).** Sufficiently high anisotropy “pushes” all the vortices to align along the major axis (see figure 5.5). In the dual limit of high anisotropy and large N , the steady state becomes essentially one-dimensional and we compute the effective one-dimensional density using techniques involving the Chebychev polynomials. As in the radially symmetric case, the vortex “lattice” has a radius a which, in the case $b \gg 1$, is implicitly given via equation

$$N \sim \frac{1}{\nu} \left(\frac{\Omega\nu}{1+b^2} \frac{a^2}{2\sqrt{1-a^2}} - \frac{(a^2-2)^2}{\nu(1-a^2)^{\frac{3}{2}}} + 1 \right). \quad (5.5)$$

6 **Maximal admissible number of vortices, high anisotropy (§5.4).** Finally, as in the radially symmetric anisotropic case, we compute $N_{\max,1d}$, the maximum number of vortices admissible for a given Ω when the anisotropy is sufficiently high to align all vortices along the major axis. It is obtained by computing maximizing (5.5) which yields

$$N_{\max,1d} = \frac{1}{\nu} \left(1 + 3^{-3/2} \left(\frac{\Omega\nu}{1+b^2} - 4 \right) \sqrt{1 + 2 \frac{\Omega\nu}{1+b^2}} \right), \quad b > 1 \quad (5.6)$$

There have been two approaches to the dynamics of vortices in a trapped condensate. The first approach relies on the fact that GP equation is the Euler-Lagrange equation for the time-dependent Lagrangian functional under variation of the wave function. If the condensate wave function depends on one or more parameters, the resulting Lagrangian functional provides approximate Lagrangian equations of motion for these parameters [93, 115, 118, 119]. Another approach is to study GP equation itself, which is the approach we take. Due to the presence of two length scales: the size of vortex core and the inter-vortex distance, it is possible to employ the method of matched asymptotics [22, 94–97]. Our approach results in a more precise equation of motion.

5.1 Vortex Dynamics

We now derive vortex dynamics for (5.1a), following closely the exposition in [22]. We start by deriving the dynamics of a single vortex, then expand our calculations to multiple vortices.

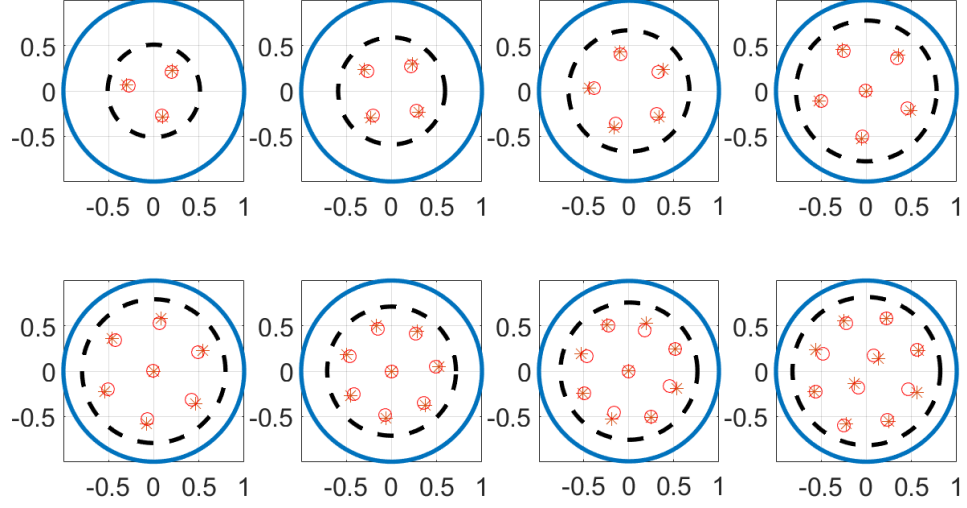


Figure 5.2: Comparison of the steady state of PDE and ODE simulations. ‘*’ denotes the steady state of the ODE system (5.2) whereas ‘o’ is from the PDE system (5.1). The parameters are chosen as: $\gamma = 1$, $\kappa = 0$, $b = 1$, $\varepsilon = 0.025$ and $\Omega = 29.51$ for 3 to 7 vortices and $\Omega = 36.89$ for 8 to 10 vortices. The dashed line represents the radius prediction a from (5.3).

5.1.1 Single Vortex

Suppose that the vortex center is located at $\xi = (\zeta, \eta) \in \mathbb{R}^2$. Following [22], we decompose the solution into the outer region $O(\varepsilon)$ away from the vortex center, and the inner region near the vortex center. We will then use matched asymptotics to match the two regions which will yield the equation of motion.

In the outer region, outside the vortex core $|x - \xi| \gg O(\varepsilon)$, we decompose the solution into phase ϕ and amplitude u :

$$w = ue^{i\phi}. \quad (5.7)$$

Substituting (5.7) into (5.1a) and separating the real and imaginary part, we then obtain:

$$\begin{aligned} \gamma u_t + \kappa u \phi_t &= (\Delta u - u|\nabla \phi|^2) + \frac{1}{\varepsilon^2} (V(x) - u^2) u + \Omega u \phi_\theta \\ -\kappa u_t + \gamma u \phi_t &= u \Delta \phi + 2 \nabla u \cdot \nabla \phi - \Omega u_\theta. \end{aligned}$$

We then expand u and v with respect to ε : $u = u_0 + \varepsilon u_1 + \dots$ and $\phi = \phi_0 + \varepsilon \phi_1 + \dots$.

Leading order equations yield

$$u_0 = \sqrt{V(x)} \quad (5.8)$$

and

$$\gamma\phi_{0t} = \Delta\phi_0 + \frac{1}{2} \frac{\nabla V}{V} \cdot (2\nabla\phi_0 - \Omega x^\perp). \quad (5.9)$$

Here and in the following, we use the notation $(a, b)^\perp = (-b, a)$. Assume that a vortex has charge +1, so that ϕ_0 satisfies a point boundary condition

$$\phi_0 \rightarrow \arg(x - \xi) \quad \text{as } x \rightarrow \xi. \quad (5.10)$$

In order to match to the inner solution of the vortex inside the vortex core, we need to understand in more detail the local behaviour of the outer solution away from the vortex points. We first decompose ϕ_0 as

$$\phi_0 = S + \tilde{\phi}_0 \quad (5.11)$$

where S is the regular solution (without any singularities) to

$$0 = \Delta S + \frac{1}{2} \frac{\nabla V}{V} \cdot (2\nabla S - \Omega x^\perp). \quad (5.12)$$

For the elliptic trap (5.1b), its solution is given by

$$S(x) = \frac{\Omega b^2 - 1}{2} \frac{1}{1 + b^2} x_1 x_2. \quad (5.13)$$

We change to moving coordinate $\tilde{x} = x - \xi(t)$ and denote by $(\tilde{r}, \tilde{\theta})$ the polar coordinates in moving coordinate. Then (5.9) becomes:

$$\gamma \left(\tilde{\phi}_{0t} - \xi_t \cdot \nabla \tilde{\phi}_0 \right) = \Delta \tilde{\phi}_0 + \frac{\nabla V(\xi + \tilde{x}) \cdot \nabla \tilde{\phi}_0}{V(\xi + \tilde{x})}, \quad (5.14)$$

or, to leading order,

$$0 \sim \Delta \tilde{\phi}_0 + \left(\gamma \xi_t^\perp + \frac{\nabla^\perp V(\xi)}{V(\xi)} \right) \cdot \nabla \tilde{\phi}_0. \quad (5.15)$$

where we have assumed that the time-dynamics are sufficiently slow that $\gamma\tilde{\phi}_{0t}$ can be discarded. In particular this is the case near a stable equilibrium.

We now solve (5.15) iteratively near the singularity $\tilde{x} \rightarrow 0$. The leading-order solution must match the point-boundary condition (5.10) which yields $\tilde{\phi}_0 \sim \tilde{\theta}$. Upon substituting $\tilde{\phi}_0 \sim \tilde{\theta} + \phi_{01}$ we obtain

$$0 = \Delta\phi_{01} + \left(\gamma \xi_t + \frac{\nabla V(\xi)}{V(\xi)} \right) \cdot \left(\frac{\tilde{x}^\perp}{|\tilde{x}|^2} + \nabla\phi_{01} \right). \quad (5.16)$$

The term $\nabla\phi_{01}$ is of smaller than the other terms. A formal expansion then yields

$$\phi_{01} = \frac{1}{2}(\log \tilde{r}) \left(\gamma \xi_t^\perp + \frac{\nabla^\perp V(\xi)}{V(\xi)} \right) \cdot \tilde{x}.$$

Finally, at the next iteration, we let $\tilde{\phi}_0 \sim \tilde{\theta} + \phi_{01} + \phi_{02}$, this yields $\phi_{02} \sim K \cdot \tilde{x}$, where the vector K depends on the vortex locations and will be determined later via asymptotic matching. In summary, we obtain

$$\phi_0(\tilde{x}, t) = S + \tilde{\theta} + \frac{1}{2}(\log \tilde{r}) \left(\gamma \xi_t^\perp + \frac{\nabla^\perp V(\xi)}{V(\xi)} \right) \cdot \tilde{x} + K \cdot \tilde{x} + \mathcal{O}(\tilde{r}^2 \log \tilde{r}) \quad (5.17)$$

which yields the following singularity behaviour for w as $x \rightarrow \xi$:

$$w(\tilde{x}, t) = e^{i(\tilde{\theta} + S(\xi))} \left(\sqrt{V(\xi)} + \frac{\nabla V(\xi) \cdot \tilde{x}}{2\sqrt{V(\xi)}} \right) \cdot \left\{ 1 + \frac{i}{2}(\log \tilde{r}) \left(\gamma \xi_t^\perp + \frac{\nabla^\perp V(\xi)}{V(\xi)} \right) \cdot \tilde{x} + i(K + \nabla S) \cdot \tilde{x} + \mathcal{O}(\tilde{r}^2 \log \tilde{r}) \right\} \quad (5.18)$$

Next we consider the inner region,

$$y = \frac{x - \xi}{\varepsilon}$$

and expand $w = W_0(y) + \varepsilon W_1(y) + \dots$. In order to match each order of ε , W_0, W_1 must satisfy:

$$\begin{aligned} 0 &= \Delta_y W_0 + V(\xi)W_0 - |W_0|^2 W_0 \\ (-\gamma - \kappa i)\xi_t + i\Omega \xi^\perp &\cdot \nabla_y W_0 - 2\nabla V(\xi) \cdot y W_0 = \Delta_y W_1 + V(\xi)W_1 - |W_0|^2 W_1 \\ &\quad - W_0 (W_0 \overline{W_1} + W_1 \overline{W_0}) \end{aligned} \quad (5.19)$$

We scale out $V(\xi)$ by changing variables

$$z = \sqrt{V(\xi)}y; \quad W_0(y) = \sqrt{V(\xi)}U_0(z), \quad W_1(y) = U_1(z)$$

so that U_0, U_1 satisfies:

$$0 = \Delta_z U_0 + U_0 - |U_0|^2 U_0 \quad (5.20)$$

$$\begin{aligned} (-\gamma - \kappa i)\xi_t + i\Omega \xi^\perp &\cdot \nabla_z U_0 - \frac{\nabla V(\xi) \cdot z}{V(\xi)} U_0 = \Delta_y U_1 + U_1 - |U_0|^2 U_1 \\ &\quad - U_0 (U_0 \overline{U_1} + U_1 \overline{U_0}). \end{aligned} \quad (5.21)$$

We look for a vortex solution of U_0 in the form of $U_0(z) = f_0(R)e^{i(\theta+S(\xi))}$, where R, θ denote the polar coordinates of $z = Re^{i\theta}$. Then (5.20) reduces to

$$f_0'' + \frac{1}{R}f_0' - \frac{1}{R^2}f_0 + f_0(1 - f_0^2) = 0 \quad (5.22)$$

with the boundary condition:

$$f_0(0) = 0, \quad f_0(+\infty) = 1. \quad (5.23)$$

The solution to (5.22, 5.23) is well known to be unique [120]. Large R expansion shows that f_0 satisfies

$$1 - f_0^2 - 1/R^2 = O(1/R^4), \quad R \rightarrow \infty. \quad (5.24)$$

Let $U_1 = f_1(R, \theta, t)e^{i(\theta+S(\xi))}$. In terms of f_1 , (5.21) becomes:

$$\begin{aligned} (-\gamma - \kappa i)\xi_t + i\Omega\xi^\perp \cdot (f_0'\nabla_z R + if_0\nabla_z\theta) - \frac{\nabla V(\xi) \cdot z}{V(\xi)}f_0 = \Delta_z f_1 + 2i(\nabla_z f_1 \cdot \nabla_z\theta) \\ - \frac{1}{R^2}f_1 + f_1(1 - 2f_0^2) - f_0^2\overline{f_1}. \end{aligned}$$

We then decompose further $f_1 = A(R)\cos\theta + B(R)\sin\theta$ and separate real and imaginary part:

$$A = A_r + iA_i, \quad B = B_r + iB_i$$

to obtain the following equations for A_r, A_i, B_r, B_i :

$$\begin{aligned} -\frac{V_{x_1}(\xi)R}{V(\xi)}f_0 - \gamma\zeta_t f_0' - \frac{\Omega\zeta + \kappa\eta_t}{R}f_0 &= A_r'' + \frac{1}{R}A_r' + (1 - 3f_0^2 - \frac{2}{R^2})A_r - \frac{2B_i}{R^2} \\ -\frac{V_{x_2}(\xi)R}{V(\xi)}f_0 - \gamma\eta_t f_0' - \frac{\Omega\eta - \kappa\zeta_t}{R}f_0 &= B_r'' + \frac{1}{R}B_r' + (1 - 3f_0^2 - \frac{2}{R^2})B_r + \frac{2A_i}{R^2} \\ \frac{-\gamma\eta_t f_0}{R} - \Omega\eta f_0' + \kappa\zeta_t f_0' &= A_i'' + \frac{1}{R}A_i' + (1 - f_0^2 - \frac{2}{R^2})A_i + \frac{2B_r}{R^2} \\ \frac{\gamma\zeta_t f_0}{R} + \Omega\zeta f_0' + \kappa\eta_t f_0' &= B_i'' + \frac{1}{R}B_i' + (1 - f_0^2 - \frac{2}{R^2})B_i + \frac{2A_r}{R^2} \end{aligned}$$

We are concerned about the behaviour of the solutions of these equations at infinity.

As $R \rightarrow \infty$, we have:

$$\begin{aligned} -\frac{V_{x_1}(\xi)R}{V(\xi)}\left(1-\frac{1}{R^2}\right)-\frac{\Omega\zeta+\kappa\eta_t}{R} &= A_r'' + \frac{1}{R}A_r' + \left(-2+\frac{1}{R^2}\right)A_r - \frac{2B_i}{R^2} + \mathcal{O}\left(\frac{1}{R^3}\right) \\ -\frac{V_{x_2}(\xi)R}{V(\xi)}\left(1-\frac{1}{R^2}\right)-\frac{\Omega\eta-\kappa\zeta_t}{R} &= B_r'' + \frac{1}{R}B_r' + \left(-2+\frac{1}{R^2}\right)B_r + \frac{2A_i}{R^2} + \mathcal{O}\left(\frac{1}{R^3}\right) \\ \frac{-\gamma\eta_t}{R} &= A_i'' + \frac{1}{R}A_i' - \frac{1}{R^2}A_i + \frac{2B_r}{R^2} + \mathcal{O}\left(\frac{1}{R^3}\right) \\ \frac{\gamma\zeta_t}{R} &= B_i'' + \frac{1}{R}B_i' - \frac{1}{R^2}B_i - \frac{2A_r}{R^2} + \mathcal{O}\left(\frac{1}{R^3}\right) \end{aligned}$$

By writing solutions in power series of R and $\log R$ for large R , we obtain

$$A_r = \frac{V_{x_1}(\xi)R}{2V(\xi)} - \left(\frac{\gamma\zeta_t}{2} + \frac{V_{x_1}(\xi)}{2V(\xi)}\right)\frac{\log R}{R} + \mathcal{O}\left(\frac{1}{R}\right) \quad (5.25a)$$

$$B_r = \frac{V_{x_2}(\xi)R}{2V(\xi)} + \left(-\frac{\gamma\eta_t}{2} - \frac{V_{x_2}(\xi)}{2V(\xi)}\right)\frac{\log R}{R} + \mathcal{O}\left(\frac{1}{R}\right) \quad (5.25b)$$

$$A_i = \left(-\frac{\gamma\eta_t}{2} - \frac{V_{x_2}(\xi)}{2V(\xi)}\right)R \log R - \frac{1}{2}\Omega\eta R + \frac{\kappa\zeta_t R}{2} + \mathcal{O}(\log R) \quad (5.25c)$$

$$B_i = \left(\frac{\gamma\zeta_t}{2} + \frac{V_{x_1}(\xi)}{2V(\xi)}\right)R \log R + \frac{1}{2}\Omega\zeta R + \frac{\kappa\eta_t R}{2} + \mathcal{O}(\log R) \quad (5.25d)$$

Putting these together, we get for $R \gg 1$,

$$U_1(z, t) = e^{i\theta+S(\xi)} \left[\frac{\nabla V(\xi)z}{2V(\xi)} + \frac{i}{2}(\log R) \left(\gamma\xi_t^\perp + \frac{\nabla^\perp V(\xi)}{V(\xi)} \right) \cdot z + \frac{i}{2}\Omega\xi^\perp \cdot z + \frac{\kappa\xi_t}{2} \cdot z \right].$$

Therefore, as $R \rightarrow \infty$, the asymptotic behaviour of the inner solution is given by:

$$\begin{aligned} W_0 + \varepsilon W_1 &= e^{i\theta+iS(\xi)} \left(\sqrt{V(\xi)}f_0(R) + \varepsilon \left[\frac{\nabla V(\xi)z}{2V(\xi)} \right. \right. \\ &\quad \left. \left. + \frac{i}{2}(\log R) \left(\gamma\xi_t^\perp + \frac{\nabla^\perp V(\xi)}{V(\xi)} \right) \cdot z + \frac{i}{2}\Omega\xi^\perp \cdot z + \frac{\kappa\xi_t}{2} \cdot z \right] \right) \end{aligned} \quad (5.26)$$

To match (5.26) with (5.18), we recall that $\tilde{x} = \frac{\varepsilon z}{\sqrt{V(\xi)}}$, $\tilde{r} = \frac{\varepsilon R}{\sqrt{V(\xi)}}$. Asymptotic matching then yields

$$\frac{i}{2}\Omega\xi^\perp + \frac{\kappa\xi_t}{2} \sim i(K + \nabla S) + \frac{i}{2}\left(\log \frac{\varepsilon}{\sqrt{V}}\right) \left(\gamma\xi_t^\perp + \frac{\nabla^\perp V(\xi)}{V(\xi)} \right)$$

or

$$\gamma\xi_t^\perp - \kappa\nu\xi_t \sim \nu \left(-\Omega\xi^\perp + 2\nabla S + 2K \right) - \frac{\nabla^\perp V(\xi)}{V(\xi)}. \quad (5.27)$$

where $\nu = \frac{1}{\log(\sqrt{V(\xi)}/\varepsilon)} \sim \frac{1}{\log(1/\varepsilon)}$. The quantity K will be determined in §5.1.2 below through asymptotic matching, and incorporates multi-vortex interactions. In the case

of a single vortex, we will show that K is bounded and thus asymptotic small compared with the other terms. In addition, we recall from (5.13, 5.1b) that $\nabla S = \frac{\Omega}{2} \frac{b^2-1}{1+b^2} (\eta, \zeta)$ and $\frac{\nabla^\perp V(\xi)}{V(\xi)} = \frac{2(b^2\eta, -\zeta)}{1-\zeta^2-b^2\eta^2}$ so that (5.27) simplifies to

$$\gamma \xi_t^\perp - \kappa \nu \xi_t = \left(\frac{-2\Omega\nu}{1+b^2} + \frac{2}{1-\zeta^2-b^2\eta^2} \right) (-b^2\eta, \zeta) \quad (5.28)$$

or equivalently,

$$\gamma \xi_t + \kappa \nu \xi_t^\perp = \left(\frac{-2\Omega\nu}{1+b^2} + \frac{2}{1-\zeta^2-b^2\eta^2} \right) \begin{pmatrix} 1 & 0 \\ 0 & b^2 \end{pmatrix} \xi \quad (5.29)$$

An immediate corollary of (5.29) is that a single vortex at the center $\xi = 0$ is stable if and only if $\Omega > \Omega_1$ where

$$\Omega_1 = \frac{1+b^2}{\nu}. \quad (5.30)$$

As a consequence, no stable vortices exist below the critical rotation rate $\Omega < \Omega_1$. The exact same critical rate was previously derived in [115] using energy methods, and it also agrees well with full numerical simulations of the full PDE system (5.1).

5.1.2 Multiple Vortices

We now seek an approximate solution of (5.1a) with N vortices in the location ξ_j , $j = 1..N$, all of the same sign $+1$. Proceeding in the same way as a single vortex, we study the dynamics of N such vortices. The inner solution W_0 near the core of vortices is the same as a single vortex. In the outer region, $\tilde{\phi}_0$ still satisfies the equation (5.9) but with N point boundary conditions $\tilde{\phi}_0 \sim \arg(x - \xi_j)$ as $x \rightarrow \xi_j$. The singularity analysis of the outer region near ξ_j is identical to the derivation of (5.17) with the end result

$$\tilde{\phi}_0(\tilde{x}, t) \sim \tilde{\theta} + \frac{1}{2}(\log \tilde{r}) \left(\gamma \xi_t^\perp + \frac{\nabla^\perp V(\xi_j)}{V(\xi_j)} \right) \cdot \tilde{x} + K_j \cdot \tilde{x} \quad (5.31)$$

where $\tilde{x} = x - \xi_j$, $\tilde{r} = |\tilde{x}|$ with $\tilde{x} \rightarrow 0$. The multi-vortex analogue for (5.29) is

$$\gamma \xi_{jt} + \kappa \nu \xi_{jt}^\perp = \left(\frac{-2\Omega\nu}{1+b^2} + \frac{2}{1-\xi_{j1}^2-b^2\xi_{j2}^2} \right) \begin{pmatrix} 1 & 0 \\ 0 & b^2 \end{pmatrix} \xi_j - \nu 2K_j^\perp. \quad (5.32)$$

It remains to determine the constants K_j via asymptotic matching. In the outer region, $\tilde{\phi}_0$ satisfies $0 \sim \Delta \tilde{\phi}_0 + \frac{\nabla V(x) \cdot \nabla \tilde{\phi}_0}{V(x)}$ or equivalently,

$$\nabla \cdot \left(V(x) \nabla \tilde{\phi}_0 \right) = 0, \quad (5.33a)$$

with N point-boundary conditions

$$\tilde{\phi}_0 \sim \arg(x - \xi_j) \quad \text{as } x \rightarrow \xi_j, \quad j = 1 \dots N \quad (5.33b)$$

In the derivation that follows, we will assume that the vortices are close to each other, separated by a small distance of $O(1/\log(1/\varepsilon))$. Similarly to a computation in [90], the leading-order solution to (5.33) is then given by¹

$$\nabla \tilde{\phi} \sim \sum_k \frac{V(\xi_k)}{V(x)} \nabla \arg(x - \xi_k).$$

Letting $x \rightarrow \xi_j$ we then obtain

$$\nabla \tilde{\phi} \sim \nabla \tilde{\theta} + \sum_{k \neq j} \frac{V(\xi_k)}{V(\xi_j)} \nabla \arg(\xi_k - \xi_j).$$

Matching with (5.31) then yields

$$K_j = \sum_{k \neq j} \frac{V(\xi_k)}{V(\xi_j)} \nabla \arg(\xi_k - \xi_j) = - \sum_{k \neq j} \frac{V(\xi_k)}{V(\xi_j)} \frac{(\xi_j - \xi_k)^\perp}{|\xi_j - \xi_k|^2}.$$

This yields the final result, which we summarize as follows:

$$\begin{aligned} \gamma \xi_{jt} + \nu \kappa \xi_{jt}^\perp \sim & \left(-\frac{2\nu\Omega}{1+b^2} + \frac{2}{1-\xi_{j1}^2 - b^2\xi_{j2}^2} \right) \begin{pmatrix} 1 & 0 \\ 0 & b^2 \end{pmatrix} \xi_j \\ & + 2 \sum_{k \neq j} \frac{\nu(\xi_j - \xi_k)}{|\xi_j - \xi_k|^2} \frac{V(\xi_j)}{V(\xi_k)}. \end{aligned} \quad (5.34)$$

This concludes the derivation of formula (5.2), which is the starting point for all the subsequent results of this paper.

5.2 Multi-vortex Lattice Density, Isotropic Trap.

We now consider the isotropic parabolic potential ($b = 1$) in the regime where the number of vortices N is large. As demonstrated in experiments [83, 121], in this case

¹The full solution to (5.33) is $\nabla \tilde{\phi} = \sum_k \frac{V(\xi_k)}{V(x)} \nabla \arg(x - \xi_k) + \frac{\nabla^\perp \psi}{V(x)}$ where ψ is chosen in such a way as to satisfy the solvability condition to make $\tilde{\phi}$ a true gradient. In particular, $\frac{\nabla^\perp \psi}{V(x)}$ is zero when V is constant. More generally, ψ satisfies $\nabla \cdot \left(\frac{\nabla \psi}{V(x)} \right) = \sum_k \nabla \cdot \left(\frac{V(\xi_k)}{V(x)} \right) \cdot \nabla^\perp \arg(x - \xi_k)$. In what follows, we assume that the vortices are close to each other in which case the term $\nabla \arg(x - \xi_k)$ dominates and ψ is a higher-order term which we ignore.

the vortices settle to a hexagonal “crystal lattice” configurations such as shown in Figure 5.1. Our goal is to estimate the asymptotic density of the resulting lattice using techniques similar to those of [116]. As a direct consequence, this computation will also yield the maximum allowed number N_{\max} of vortices as a function of system parameters.

We start with the ODE system (5.2) that describes the evolution of multiple vortex centers. Since we are interested in the steady state $\xi_j(t) \rightarrow \xi_j$, we only consider the overdamped regime (i.e. imaginary time integration) $\gamma \rightarrow \infty$. Equivalently, by rescaling the time, in the case of the isotropic potential ($b = 1$) the system (5.34) may be written as

$$\xi_{j\tau} = \left(-\nu\Omega + \frac{2}{1 - |\xi_j|^2} \right) \xi_j + 2\nu(1 - |\xi_j|^2) \sum_{k \neq j} \frac{\xi_k - \xi_j}{|\xi_k - \xi_j|^2} \frac{1}{1 - |\xi_k|^2}. \quad (5.35)$$

Following [116], we coarse-grain by defining the particle density to be

$$\rho(x) = \sum \delta(x - \xi_k). \quad (5.36)$$

Equation (5.35) can then be written as $\xi_{j\tau} = v(\xi_j)$ where the velocity v is given by

$$v(x) = \left(-\nu\Omega + \frac{2}{1 - |x|^2} \right) x + 2\nu(1 - |x|^2) \int_{R^2} \frac{x - y}{|x - y|^2} \frac{1}{1 - |y|^2} \rho(y) dy. \quad (5.37a)$$

In the continuum limit $N \rightarrow \infty$, this equation is coupled to the conservation of mass,

$$\rho_\tau(x, \tau) + \nabla_x \cdot (v(x)\rho(x, \tau)) = 0 \quad (5.37b)$$

Together, (5.37) describe the vortex density evolution in the limit $N \rightarrow \infty$ for the overdamped regime (5.35). The density ρ is compactly supported. Assuming that the density is radial, it is possible to compute the steady state $\rho(x, t) = \rho(|x|)$ and its radial support explicitly using techniques from [116], as we now show. Assume that the density is supported on a disk of radius a , so that $\rho(r) = 0$ for $r > a$ and $\rho(r) > 0$ for $0 \leq r < a$. A key identity is

$$\int_{R^2} \frac{x - y}{|x - y|^2} g(|y|) dy = x \frac{2\pi}{r^2} \int_0^r g(s) s ds, \quad (5.38)$$

which holds for any integrable function $g(r)$.

Applying (5.38) to (5.37a) then yields

$$v(x) = \left(-\nu\Omega + \frac{2}{1 - r^2} + \frac{4\pi\nu(1 - r^2)}{r^2} \int_0^r \frac{1}{1 - s^2} \rho(s) s ds \right) x. \quad (5.39)$$

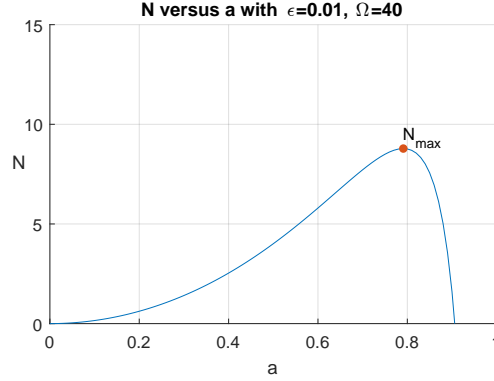


Figure 5.3: Number of vortices N as a function the vortex lattice radius a . Note the appearance of a maximum N_{\max} corresponding to the maximum admissible number of vortices. Other parameters are as given in the title.

Inside the support $r < a$, we set $v = 0$. Upon differentiating with respect to r we obtain

$$\rho(r) = \frac{1}{4\pi\nu} \left(-\frac{2\Omega\nu r}{(1-r^2)} - \frac{4}{(1-r^2)} + \frac{8}{(1-r^2)^2} \right). \quad (5.40)$$

Note from (5.36) that the total mass is N . Since we assumed that the density is supported on $|x| < a$, this leads to an additional constraint

$$\int_0^a \rho(s) s ds = \frac{N}{2\pi}. \quad (5.41)$$

Combining (5.40) and (5.41), we obtain an explicit relationship between the support radius a and N ,

$$N = \frac{1}{\nu} \left(\left(-1 - \frac{1}{2}\Omega\nu \right) \ln(1-a^2) + 2 - 2(1-a^2)^{-1} \right) \quad (5.42)$$

A typical graph of N versus a is shown in Figure 5.3. Note that this graph attains the maximum which we compute by setting $\partial N/\partial a = 0$. This maximum N_{\max} is attained at $a = \frac{\sqrt{\Omega\nu-2}}{\sqrt{\Omega\nu+2}}$ and has an explicit expression given by

$$N_{\max} = \frac{1}{\nu} \left\{ (\Omega\nu + 2) \left(\frac{1}{2} \ln(\Omega\nu + 2) - \ln(2) - \frac{1}{2} \right) + 2 \right\}. \quad (5.43)$$

We remark that Aftalion and Du [115] derived yet another formula for the threshold N_{\max} but using the variational framework; see formula (3.4) in [115]. In our notation, this formula can be rewritten as

$$N_{\max, \text{Aftalion/Du}} = 1 + \left(\Omega - \frac{2}{\nu} \right) \frac{1}{\log(2/\nu)}. \quad (5.44)$$

It is also shown in Figure 5.2. Unlike our formula (5.44), Aftalion/Du formula is linear in Ω . It works reasonably well for a small number of vortices, but loses its accuracy as the number of vortices increases.

Finally, let us mention that a similar computation was done in [116] for a simplified version of vortex motion equations that did not incorporate the trap density in vortex-to-vortex interactions suggested in [117], namely

$$z_{j\tau} = \left(-\nu\Omega + \frac{2}{1 - |z_j|^2} \right) z_j + 2\nu \sum_{k \neq j} \frac{z_k - z_j}{|z_k - z_j|^2}. \quad (5.45)$$

For this simplified system, a similar analysis (see [116], section 4) yields the formula

$$N_{\max, \text{CKK}} = \frac{1}{\nu} \left(\sqrt{\frac{\Omega\nu}{2}} - 1 \right)^2. \quad (5.46)$$

In fact, formulas (5.43) and (5.46) both agree near $\Omega\nu = 2$ as can be seen by expanding in Taylor series around $\Omega\nu = 2$; in this regime, νN_{\max} is small, the radius a is also small and both formulas yield $\nu N_{\max} = \frac{1}{16} (\Omega\nu - 2)^2 + O((\Omega\nu - 2)^3)$ with $a \sim \sqrt{\Omega\nu - 2} + o(\sqrt{\Omega\nu - 2})$. However the formula (5.46) has a very poor agreement for larger N .

5.3 Two Vortices, Anisotropic Trap

Let us now investigate in some more detail the case of two vortices in an anisotropic trap ($b \neq 1$). In the isotropic case ($b = 1$), a basic steady state configuration consists of two antipodal vortices along *any* line through the center. However the introduction of the anisotropy breaks the rotational symmetry, leading to two possible steady states: either vortex centers lie on the x-axis or on the y-axis. Both configurations may be admissible as steady states. However the stability analysis below will show that only the configuration with two vortices along the longest axis of the ellipse $x^2 + by^2 = 1$ is stable, the other configuration being unstable.

First, consider two vortices in a stable configuration along the x -axis, with coordinates $\xi_1 = (r, 0)$ and $\xi_2 = (-r, 0)$. Upon substituting into equation of motion (5.2) we obtain an algebraic equation for r ,

$$\left(-\frac{\nu\Omega}{1 + b^2} + \frac{1}{1 - r^2} \right) r + \frac{\nu}{2r} = 0. \quad (5.47)$$

This equation is quadratic in r^2 , and admits two positive solutions r_{\pm} with $r_- < r_+$, provided that $\Omega > \Omega_2$ where

$$\Omega_2 = \frac{1}{\nu} \frac{1+b^2}{2} \left(\sqrt{2} + \sqrt{\nu} \right)^2. \quad (5.48)$$

There is a fold point at $\Omega = \Omega_2$ and the solution disappears when $\Omega < \Omega_2$. The same formula for Ω_2 holds for two vortices along the y -axis. Note that to leading order in ν , $\Omega_2 \sim (1+b^2)/\nu$, which agrees with the stability threshold for a single spike Ω_1 , see (5.30).

In a pioneering work [115], Aftalion and Du derived slightly different formula was derived for Ω_2 , using a related energy method, see formula (22) there. Written in our notation, the formula in [115] is:

$$\Omega_{2,\text{Aftalion/Du}} = \frac{1+b^2}{\nu} + \frac{1+b^2}{2} \log \left(\frac{1+b^2}{\nu} \right). \quad (5.49)$$

While both formulas have the same leading-order behaviour in ν , they have very different (and large) correction terms. Figure 5.4(a) shows a direct comparison between (5.48), (5.49) and the full numerical simulations of the PDE (5.1). Formula (5.48) appears to be a significant improvement over (5.49).

For $\Omega > \Omega_2$, the only *potentially stable* solution is the one corresponding to r_- as can be seen by considering perturbations along the x -axis. However this does not tell the whole story: a solution may exist and be stable along the x -axis, but be unstable with respect to the full spectrum of two-dimensional perturbations. To describe the full stability, as in section 5.2, we will – for simplicity – consider the overdamped system $\kappa = 0, \gamma = 1$ (it can be shown that stability properties are independent of κ as long as $\gamma > 0$). The full equations then become

$$\begin{aligned} \frac{dx_1}{dt} &= \left(-2\hat{\Omega} + \frac{2}{1-x_1^2-b^2y_1^2} \right) x_1 + \frac{2\nu(x_1-x_2)}{(x_1-x_2)^2+(y_1-y_2)^2} \frac{1-x_1^2-b^2y_1^2}{1-x_2^2-b^2y_2^2} \\ \frac{dy_1}{dt} &= \left(-2\hat{\Omega} + \frac{2}{1-x_1^2-b^2y_1^2} \right) b^2y_1 + \frac{2\nu(y_1-y_2)}{(x_1-x_2)^2+(y_1-y_2)^2} \frac{1-x_1^2-b^2y_1^2}{1-x_2^2-b^2y_2^2} \\ \frac{dx_2}{dt} &= \left(-2\hat{\Omega} + \frac{2}{1-x_2^2-b^2y_2^2} \right) x_2 + \frac{2\nu(x_2-x_1)}{(x_1-x_2)^2+(y_1-y_2)^2} \frac{1-x_2^2-b^2y_2^2}{1-x_1^2-b^2y_1^2} \\ \frac{dy_2}{dt} &= \left(-2\hat{\Omega} + \frac{2}{1-x_2^2-b^2y_2^2} \right) b^2y_2 + \frac{2\nu(y_2-y_1)}{(x_1-x_2)^2+(y_1-y_2)^2} \frac{1-x_2^2-b^2y_2^2}{1-x_1^2-b^2y_1^2} \end{aligned} \quad (5.50)$$

where we defined

$$\hat{\Omega} := \frac{\nu\Omega}{1+b^2}. \quad (5.51)$$

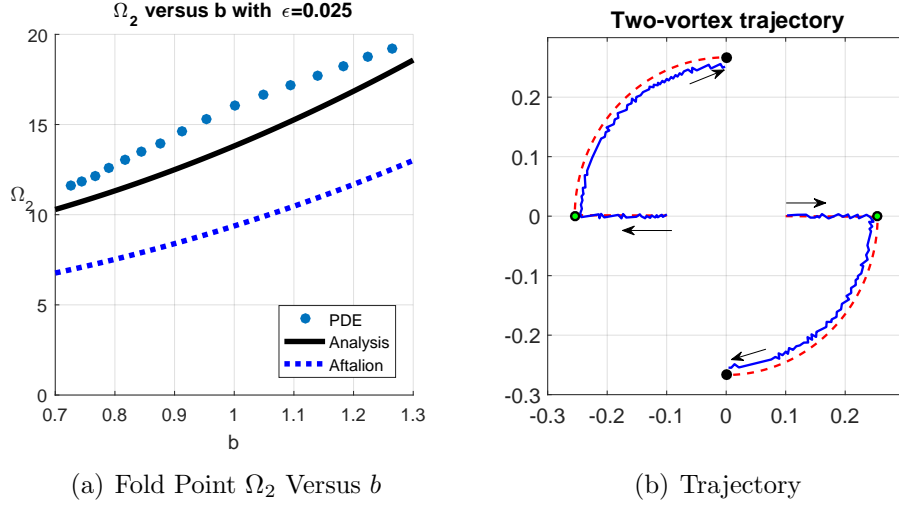


Figure 5.4: (a) Ω_2 as a function of b : comparison of full numerics and asymptotics. Dots are obtained from full numerical computations of the full PDE (5.1). Dashed line denotes the asymptotic formula (5.48). Dashed line is the formula (5.49) derived in [115]. Parameter values are $\gamma = 1$, $\kappa = 0$, $\varepsilon = 0.025$. (b) Two-vortex trajectory. Parameter values are $\varepsilon = .025$, $\Omega = 22.133$ and $b = 0.9535$. Initial conditions consist of two vortices along x -axis. Arrows indicate the direction of motion. At first, the vortices approach a saddle point along the x -axis (indicated by green-black dots). But eventually the two vortices settle along the y -axis (indicated by black dots). Solid curve shows vortex centers from the full PDE simulation of (5.1) with $\gamma = 1, \kappa = 0$. Dashed line shows the simulation of the the reduced ODE (5.50).

Linearizing around the equilibrium $x_1 = r, x_2 = -r, y_1 = y_2 = 0$, we obtain the following Jacobian matrix,

$$\begin{pmatrix} 2M_1 & 0 & 2M_3 & 0 \\ 0 & 2M_2 & 0 & 2M_4 \\ 2M_3 & 0 & 2M_1 & 0 \\ 0 & 2M_4 & 0 & 2M_2 \end{pmatrix}$$

where

$$\begin{aligned} M_1 &= -\hat{\Omega} + \frac{1}{1-r^2} + \frac{2r^2}{(1-r^2)^2} - \frac{\nu}{4r^2} - \frac{\nu}{1-r^2}, & M_2 &= -\hat{\Omega}b^2 + \frac{b^2}{1-r^2} + \frac{\nu}{4r^2} \\ M_3 &= \frac{\nu}{4r^2} - \frac{\nu}{1-r^2}, & M_4 &= -\frac{\nu}{r^2} \end{aligned}$$

The eigenvalues of this matrix are easily computed as $2M_1 \pm 2M_3$ and $2M_2 \pm 2M_4$

which yields,

$$\begin{aligned}\lambda_1 &= 2M_1 + 2M_3 = -2\hat{\Omega} + \frac{2}{1-r^2} + \frac{4r^2}{(1-r^2)^2} - \frac{4\nu}{1-r^2} \\ \lambda_2 &= 2M_1 - 2M_3 = -2\hat{\Omega} + \frac{2}{1-r^2} + \frac{4r^2}{(1-r^2)^2} - \frac{2\nu}{r^2} \\ \lambda_3 &= 2M_2 + 2M_4 = -2\hat{\Omega}b^2 + \frac{2b^2}{1-r^2} \\ \lambda_4 &= 2M_2 - 2M_4 = -2\hat{\Omega}b^2 + \frac{2b^2}{1-r^2} + \frac{\nu}{r^2}.\end{aligned}$$

Using the relationships $\hat{\Omega} = \frac{\nu}{2r^2} + \frac{1}{1-r^2}$ and $\Omega > \Omega_2$, basic algebra shows that $\lambda_{1,2,3} < 0$. On the other hand, λ_4 becomes

$$\lambda_4 = 2(-b^2 + 1)\frac{\nu}{r^2}$$

and goes through zero precisely at $b = 1$; it is stable for $b > 1$ and unstable for $0 < b < 1$. The underlying elliptic trap has the form $x^2 + b^2y^2 = 1$. When $b > 1$, the x-axis is the major axis and the y-axis is the minor axis of the ellipse; the opposite is true for $b < 1$. This shows that the two-vortex configuration is stable only along the *major* axis.

Figure 5.4(b) illustrates this stability result. There, we took $b = 0.9535$, so that the trap is nearly circular but with the y -axis slightly longer. So we expect a two-vortex equilibrium to be unstable along the x -axis but stable along the y -axis. This is indeed what happens. We ran the imaginary-time integration ($\kappa = 0$) for the full PDE (5.1), starting with initial conditions consisting of two vortices along the x -axis. At first, the two vortices approach the unstable equilibrium along the x -axis (although unstable, it is a saddle point and initial conditions are along its stable manifold). However eventually, since this equilibrium is unstable, they travel towards a stable equilibrium along the y -axis.

5.4 Large N Limit with Strongly Anisotropic Trap

We now consider a strong anisotropic parabolic potential case $b \rightarrow \infty$. Figure 5.5 illustrates this case with $b = 3$. For sufficiently strong anisotropy, the vortices align along the major axis of the elliptic trap (the x-axis in the case $b \rightarrow \infty$). Exactly *how* strong depends on the number of vortices and the exact dependence is an open question

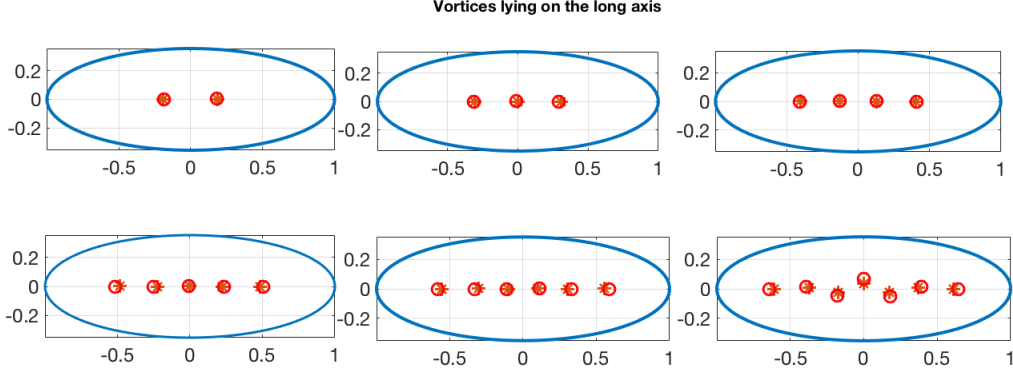


Figure 5.5: Comparison of the steady state of PDE and ODE simulations for $N = 2 \dots 7$ vortices. ‘*’ denotes the steady state of the ODE system (5.2) whereas ‘o’ is from the PDE system (5.1). The parameters are chosen as: $\gamma = 1$, $\kappa = 0$, $b = \sqrt{8}$, $\varepsilon = 0.0083$ and $\Omega = 57.67$. The boundary of the elliptical trap $x^2 + b^2y^2 = 1$ is also shown.

that we leave for future study. For now, we simply assume that the anisotropy is sufficiently strong for the full alignment to occur, so that the steady state is effectively one-dimensional. In this case, the ODE system (5.2) reduces motion purely along the x -axis, leading to the following dynamical system of N variables:

$$x_{jt} = \left(-2\hat{\Omega} + \frac{2}{1-x_j^2} \right) x_j + 2\nu \sum_{k \neq j} \frac{1-x_j^2}{1-x_k^2} \frac{x_j - x_k}{|x_j - x_k|^2}, \quad (5.52a)$$

where

$$\hat{\Omega} := \nu \frac{\Omega}{1+b^2}. \quad (5.52b)$$

(where for simplicity we took the overdamped limit $\gamma = 1, \kappa = 0$). We wish to compute the effective one-dimensional density of the resulting steady state in the continuum limit $N \rightarrow \infty$ of this system. As in §5.2, we define the one-dimensional density to be

$$\rho(x) = \sum \delta(x - x_j).$$

The steady-state density then satisfies

$$\left(-\hat{\Omega} + \frac{1}{1-x^2} \right) z + \nu (1-x^2) \int_{-a}^a \frac{1}{y-x} \frac{1}{1-y^2} \rho(y) dy = 0 \quad (5.53a)$$

where \int_{-a}^a denotes the Cauchy principal value integral. Here, a is the radius of the vortex “lattice”. The solution to (5.53a) is subject to the additional mass constraint

$$\int_{-a}^a \rho(x) dx = N \quad (5.53b)$$

Together, equations (5.53) are to be solved for both the density $\rho(x)$ and the radius a .

A solution to (5.53) can be derived using techniques involving the Chebychev polynomials, as suggested by [122], (see Chapter 18 there the Fourier–Chebyshev series). We start by recalling the following basic identities between Chebyshev polynomials U_n and T_n (see, for example, the Wikipedia entry):

$$\int_{-1}^1 \frac{\sqrt{1-y^2} U_{n-1}(x)}{y-x} dy = -\pi T_n(x) \quad (5.54a)$$

$$\int_{-1}^1 \frac{T_n(x)}{(y-x)\sqrt{1-y^2}} dy = \pi U_{n-1}(x) \quad (5.54b)$$

$$\int_{-1}^1 \frac{T_n(x) T_m(x)}{\sqrt{1-y^2}} dy = \begin{cases} 0 & n \neq m \\ \pi & n = m = 0 \\ \pi/2 & n = m \neq 0 \end{cases} \quad (5.54c)$$

$$\int_{-1}^1 U_n(x) U_m(x) \sqrt{1-y^2} dy = \begin{cases} 0 & n \neq m \\ \pi/2 & n = m = 0 \end{cases} \quad (5.54d)$$

Identity (5.54a) as well as the form of the integral equation (5.53a) motivates the following ansatz for the density ρ :

$$\rho(x) = -\frac{1}{\pi} \sum_{i=1}^{\infty} c_i U_{i-1}\left(\frac{x}{a}\right) (1-x^2) \sqrt{1-\frac{x^2}{a^2}}. \quad (5.55a)$$

Using (5.54d) then yields the following expression for c_i in terms of a :

$$c_i = \frac{2}{\pi} \int_{-1}^1 \left(-\hat{\Omega} + \frac{1}{1-a^2 y^2} \right) \frac{ay}{\nu(1-a^2 y^2)} T_i(y) \frac{1}{\sqrt{1-y^2}} dy. \quad (5.55b)$$

Upon substituting (5.55a) into (5.53a) and using identities (5.54) we obtain

$$\int_{-a}^a \rho(x) dx = -\frac{a}{2} \left(c_1 \left(1 - \frac{a^2}{4}\right) - \frac{a^2}{4} c_3 \right) = N \quad (5.55c)$$

Evaluating c_1 and c_3 using (5.55b) finally yields the following relationship between N and a ,

$$N = \frac{1}{\nu} \left(\frac{\hat{\Omega} a^2}{2\sqrt{1-a^2}} - \frac{(a^2-2)^2}{\nu(1-a^2)^{\frac{3}{2}}} + 1 \right). \quad (5.55d)$$

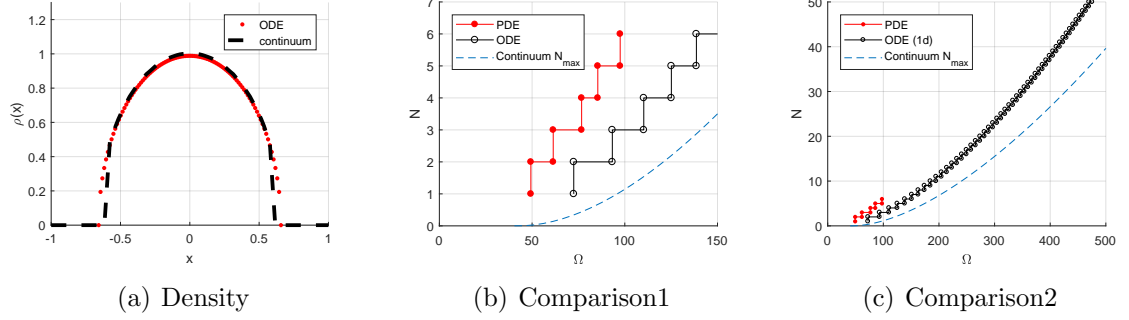


Figure 5.6: (a) Steady state density of the ODE system (5.52), compared with the continuum limit (5.55), where only eight terms of the series is used. Here, $N = 40$ and $\hat{\Omega} = 10.8$ (b) Maximal admissible number of vortices for the full PDE simulation of (5.1) versus the ODE system (5.2), versus the continuum formula (5.56). Both PDE and ODE simulations are fully two-dimensional. Parameters are $\gamma = 1, \kappa = 0, \varepsilon = 0.0088, b = 2.83$ and Ω is slowly decreasing according to the formula $\Omega = 150 - 10^{-4}t$. (c) Comparison of the ODE (5.52) and continuum limit formula (5.56) with ODE motion restricted to the x-axis, for larger number of vortices. Same parameters as in (b), except that $\Omega = 500 - 10^{-4}t$.

Note that while the expression for the radius a is explicit, the density $\rho(x)$ itself does not appear to have a closed form solution, having an infinite-series representation (5.55a). However the coefficients c_i in (5.55a) are easy to compute numerically, while in practice the series representation converges very quickly. Figure 5.6(a) shows a direct comparison between the analytical density (5.55a) and the steady state of (5.53) with $N = 40$.

The function $a \rightarrow N(a)$ has a unique maximum at $a^2 = 2(\hat{\Omega} - 1)/(2\hat{\Omega} + 1)$, given by

$$N_{\max,1d} = \frac{1}{\nu} \left(1 + 3^{-3/2}(\hat{\Omega} - 4)\sqrt{1 + 2\hat{\Omega}} \right). \quad (5.56)$$

This provides the asymptotic upper bound for the number of vortices that can be aligned along the x-axis. This is the main result of this section, concluding the derivation of (5.6). Figure 5.6(c) shows the comparison between the formula (5.56) and the ODE. Although it appears that the two curves diverge, their ratio approaches 1 as $\hat{\Omega}$ is increased.

5.5 Discussion

In this chapter we derived a novel and more accurate set of ODE's (5.2) for vortex motion in BEC with an anisotropic trap. These ODE's incorporate the effect of the trap inhomogeneity on vortex-to-vortex interactions. In turn, the analysis of ODEs yield an accurate analytical formula for the vortex lattice density, as well as the maximal admissible number of vortices N_{\max} as a function of rotation rate Ω under two scenarios: isotropic trap with large N , and high-anisotropy regime with large N . Additionally, we examined existence and stability of two vortices in an anisotropic trap. For the isotropic case, we used techniques from the swarming literature [116, 123] to estimate the large- N vortex lattice density. In the case of high-anisotropy, we used Chebychev expansions to obtain expansion in the density and explicitly compute the critical thresholds.

It would be interesting to redo the analysis of [117] for the new ODE system (5.2). For example, is there asymmetric configurations of two vortex-pairs?

Our results improve upon known results in the literature in two ways. The reduced system of motion (5.2) is more accurate than that previously reported in, e.g., [116, 117]. As a consequence, we have obtained more accurate thresholds for existence and stability, especially in the case of multiple vortices, but also in the case of two vortices within an anisotropic trap. Numerical experiments show that these thresholds improve upon those found in [115].

It is interesting to note that in addition to the upper bound N_{\max} , there is also a lower bound on the number of vortices, N_{\min} , for a given rotation rate Ω . As Ω is sufficiently increased, vortices suddenly nucleate from the Thomas-Fermi boundary. In the case of an isotropic trap, a zero-vortex state becomes unstable as Ω increases past $\underline{\Omega} = 2.561\varepsilon^{-2/3}$ – see [124–126] for derivation. This computation can be extended to a single vortex at the center of degree N . In this case, one finds that the stability threshold is $\underline{\Omega} = 2.53\varepsilon^{-2/3} + 2N$. Solving for N , this in turn yields the formula

$$N_{\min} = \frac{\Omega}{2} - 1.28\varepsilon^{-2/3}. \quad (5.57)$$

Assuming that the whole vortex lattice is concentrated near the origin, one can approximate the whole lattice of N vortices by a single vortex of degree N . This suggests that (5.57) provides an asymptotic *lower bound* for existence of N vortices as

a function of Ω , so that $N_{\min} < N < N_{\max}$. We have verified numerically that this is the case as long as the vortex lattice is not too “spread-out” throughout the trap. An open question is to extend this bound to an anisotropic trap, as well as the situation where the vortex lattice is spread throughout the trap, and cannot be easily reduced to a single N -degree vortex.

In conclusion, direct asymptotic reduction of the GPE, combined with coarse-graining techniques for large number of vortices provide a powerful tool that yields novel insights into a well-studied classical problem of Bose-Einstein Condensates.

Chapter 6

Conclusions and Future Research

In this thesis we studied the dynamics (especially oscillatory dynamics) and stability of localized patterns in PDE's. We employed a combination of asymptotic and numerical methods to compute instability thresholds and describe the motion of patterns.

First, we considered the dynamics of many interfaces for a general class of reaction diffusion systems. We showed that $2K$ interfaces will oscillate in-phase with a constant amplitude like a single interface after τ in (2.1) exceeds a critical threshold. We began with a reduced ODE-PDE coupled system that is used to capture the locations of interfaces. Through the study of this coupled system, we showed that there are only three possible long time behaviors for the interface locations: (1) some interfaces collide; (2) all n interfaces reach a symmetric steady state; (3) all n interfaces oscillate indefinitely.

Second, we studied the periodic motion of the location and height of a spot solution in the two dimensional Schnakenberg model. These two different behaviors are due to two different Hopf bifurcations. We determined which motion happens first by conducting linear stability analysis of the steady state. We explicitly computed the critical feed rate for the intersection point of these two stability thresholds. Beyond the Hopf bifurcation, we studied the dynamics of spot location. We derived an ODE-PDE coupled system that governs the slow dynamics of the spot position and obtained an explicit solution to this system by using Bessel series, which is in good agreement with the the original PDE model.

We then applied a similar method to the three-dimensional Schnakenberg system and characterized the dynamics of spots in this case. The ODEs we derive provide useful information for the configuration of many spot steady state. We also extend the result to the situation of a spatially varying feed rate.

In addition, we investigated the vortex dynamics in Bose-Einstein Condensate with a rotating trap. In the framework of Gross-Pitaveskii equation, we derived a reduced

ODE system to capture the location of vortices. The vortex-to-vortex interaction term we used in our system is novel and led to a better description of the configuration of vortex lattices. From the ODEs we derived, we showed that a pair of symmetric vortices lying on the long (short) axis is linearly stable (unstable) for the anisotropic potential. We then further investigated the many-vortex limit in the case of isotropic potential and strong anisotropic potential and computed the effective vortex density in both case, as well as N_{max} , the maximum admissible number of vortices for a given rotation rate..

There are many directions for the further work. We have mentioned some of them in the discussion of each chapter. Let us emphasize some common themes here.

- **Moving singularity problems:** In chapters 2-5, we have derived a series of reduced systems for the slow dynamics of localized structures: (2.15,3.87,4.17,5.34). In the context of oscillating interfaces (chapter 2) or spot (chapter 3), these reduced systems typically consist of a PDE for the outer region coupled to an ODE for the location of the pattern. In particular the circular motion of a spot (chapter 3) is described by a PDE with a moving source. Due to the moving source term in the PDE, the system could be solved explicitly or asymptotically only under a restricted regime. Thus numerical simulation of this system is essential for further study. The numerical difficulty is that the ODE for the singularity location requires an extraction of a very weakly singular part of the solution of the PDE. The analysis in chapter 3 illustrate how the singularity can be extracted under some specific assumption. In general, how to obtain the right form of the singular part is an open problem that needs further study.
- **Distribution of many localized structures:** The reduced system we derived describing the location of local structures could be approximated by a nonlocal PDE that describes their density when the number of localized structures becomes large (the so-called mean-field limit). This can yield important insights that cannot easily be obtained from looking at the finite N situation. This analysis has been done for GPE in chapter 5 and for the Schnakenberg mode in [128]. It would be interesting if we could apply this analysis to other systems.
- **Three or more component system:** All the systems we study have at most

two components. With three components, the dynamics of localized structures can exhibit much richer behaviors. One possible avenue of research is to carry out the method we used in this thesis to three or more component systems, such as the gas discharge model [129]. In particular, in [39] the authors show that out-of-sync oscillations are possible for this system, something that we could not observe in the two-component systems studied in chapter 3.

- **Rigorous proof of the formal results** The reader must have noted that we have used methods of formal asymptotics to derive our results throughout this thesis. Although we validate our results by comparing to full numerical simulations, it is still important to provide rigorous proofs to the order of errors. There are techniques available to provide formal justification such as a method based on Liapunov-Schmidt reduction [58]. It is an open problem to apply these rigorous methods to the problems studied in this thesis.

Bibliography

- [1] V. Deimede, K. Nikitopoulou, A. Voegelé, J. Kallitsis, Study of polymer blend membranes composed of sulfonated polysulfone and pego-grafted aromatic polyether with controllable morphology, *European Polymer Journal* 63 (2015) 113–122.
- [2] Wikipedia, URL "<https://en.wikipedia.org/wiki/Patternsinnature>".
- [3] T. Simula, A. Penckwitt, R. Ballagh, Giant vortex lattice deformations in rapidly rotating bose-einstein condensates, *Physical review letters* 92 (6) (2004) 060401.
- [4] R. FitzHugh, Mathematical models of threshold phenomena in the nerve membrane, *Bulletin of Mathematical Biology* 17 (4) (1955) 257–278.
- [5] J. Nagumo, S. Arimoto, S. Yoshizawa, An active pulse transmission line simulating nerve axon, *Proceedings of the IRE* 50 (10) (1962) 2061–2070.
- [6] J. Schnakenberg, Simple chemical reaction systems with limit cycle behaviour, *Journal of theoretical biology* 81 (3) (1979) 389–400.
- [7] P. Gray, S. Scott, Autocatalytic reactions in the isothermal, continuous stirred tank reactor: isolas and other forms of multistability, *Chem. Eng. Sci.* 38 (1983) 29–43.
- [8] Y. Chen, T. Kolokolnikov, J. Tzou, C. Gai, Patterned vegetation, tipping points, and the rate of climate change, *European Journal of Applied Mathematics* 26 (06) (2015) 945–958.
- [9] D. L. Benson, J. A. Sherratt, P. K. Maini, Diffusion driven instability in an inhomogeneous domain, *Bulletin of mathematical biology* 55 (2) (1993) 365–384.
- [10] L. Shaw, J. Murray, Analysis of a model for complex skin patterns, *SIAM Journal on Applied Mathematics* 50 (2) (1990) 628–648.
- [11] E. P. Gross, Structure of a quantized vortex in boson systems, *Il Nuovo Cimento* (1955-1965) 20 (3) (1961) 454–477.
- [12] S. Rice, *Diffusion-Limited Reactions*, Elsevier, Amsterdam, 1985.
- [13] J. K. I. Eliazar, T. Koren, Searching circular dna strands, *J. Phys: Condens. Matter* 6.
- [14] O. Bénichou, C. Loverdo, M. Moreau, R. Voituriez, A minimal model of intermittent search in dimension two, *Journal of Physics: Condensed Matter* 19 (6) (2007) 065141.

- [15] G. Oshanin, H. Wio, K. Lindenberg, S. Burlatsky, Intermittent random walks for an optimal search strategy: one-dimensional case, *J. Phys: Condens. Matter* 19.
- [16] O. Benichou, C. Loverdo, M. Moreau, R. Voituriez, Optimizing intermittent reaction paths, *Phys. Chem. Chem. Phys.* 10.
- [17] R. M. M.A. Lomholt, K. Tal, K. Joseph, Levy strategies in intermittent search processes are advantageous, *Proc. Natl. Acad. Sci.* 105 (32) (2008) 11055.
- [18] M. M. O. Benichou, C. Loverdo, R. Voituriez, Intermittent search strategies, *Rev. Modern Phys.* 83.
- [19] S. Xie, T. Kolokolnikov, Oscillations of many interfaces in the near-shadow regime of two-component reaction-diffusion systems, *DISCRETE AND CONTINUOUS DYNAMICAL SYSTEMS-SERIES B* 21 (3) (2016) 959–975.
- [20] S. Xie, T. Kolokolnikov, Moving and jumping spot in a two-dimensional reaction–diffusion model, *Nonlinearity* 30 (4) (2017) 1536.
- [21] J. Tzou, S. Xie, T. Kolokolnikov, M. Ward, The stability and slow dynamics of localized spot patterns for the 3-d schnakenberg reaction-diffusion model, *SIAM Journal on Applied Dynamical Systems* 16 (1) (2017) 294–336.
- [22] E. Weinan, Dynamics of vortices in ginzburg-landau theories with applications to superconductivity, *Physica D: Nonlinear Phenomena* 77 (4) (1994) 383–404.
- [23] J. C. Tzou, S. Xie, T. Kolokolnikov, First-passage times, mobile traps, and hopf bifurcations, *Physical Review E* 90 (6) (2014) 062138.
- [24] Y. Nishiura, H. Fujii, Stability of singularly perturbed solutions to systems of reaction-diffusion equations, *SIAM J.Math.Anal* 18 (1987) 1726–1770.
- [25] Y. Nishiura, M. Mimura, Layer oscillations in reaction-diffusion systems, *SIAM J.Appl. Math* 49 (1989) 481–514.
- [26] R. E. Goldstein, D. J. Muraki, D. M. Petrich, Interface proliferation and the growth of labyrinths in a reaction-diffusion system, *Phys. Rev. E* 53 (4) (1996) 3933–3957.
- [27] B. S. Kerner, V. V. Osipov, *Autosolitons: a New Approach to Problems of Self-Organization and Turbulence*, Kluwer, Dordrecht, 1994.
- [28] C. B. Muratov, V. Osipov, Scenarios of domain pattern formation in a reaction-diffusion system, *Phys.Rev.E* 54 (1996) 4860–4879.
- [29] M. Taki, M. Tlidi, T. Kolokolnikov, editors, *Dissipative localized structures in extended systems*.

- [30] T. Kolokolnikov, T. Erneux, J. Wei, Mesa-type patterns in the one-dimensional brusselator and their stability, *Physica D* 214 (2006) 63–77.
- [31] T. Kolokolnikov, M. Ward, J. Wei, Self-replication of mesa patterns in reaction-diffusion models, *Physica D*, Vol 236 (2) (2007) 104–122.
- [32] R. McKay, T. Kolokolnikov, Stability transitions and dynamics of mesa patterns near the shadow limit of reaction-diffusion systems in one space dimension, *Discrete and Continuous Dynamical Systems-Series B* 17 (1) (2012) 191–220.
- [33] S. Koga, Y. Kuramoto, Localized patterns in reaction-diffusion systems, *Progress of Theoretical Physics* 63 (1) (1980) 106–121.
- [34] D. Haim, G. Li, Q. Ouyang, W. D. McCormick, H. L. Swinney, A. Hagberg, E. Meron, Breathing spots in a reaction-diffusion system, *Phys. Rev. Lett* 77 (1996) 190–193.
- [35] A. Hagberg, E. Meron, Pattern formation in non-gradient reaction-diffusion systems: the effect of front bifurcations, *Nonlinearity* 7 (1994) 805–835.
- [36] T. Ikeda, Y. Nishiura, Pattern selection for two breathers, *SIAM J. Appl. Math* 54 (1) (1994) 195–230.
- [37] H. Ikeda, T. Ikeda, Bifurcation phenomena from standing pulse solutions in some reaction-diffusion systems, *J. Dyn. Diff. Eqns* 12 (1).
- [38] S. V. Gurevich, S. Amiranashvili, H. G. Purwins, Breathing dissipative solitons in three component reaction-diffusion system, *Physical Review E* 74.
- [39] M. Suzuki, T. Ohta, M. Mimura, H. Sakaguchi, Breathing and wiggling motions in three-species laterally inhibitory systems, *Physical Review E* 52 (4) (1995) 3645–3655.
- [40] I. Rozada, Topics in the stability of localized patterns for some reaction-diffusion systems, Ph.D. thesis, University of British Columbia (2012).
- [41] R. McKay, T. Kolokolnikov, P. Muir, Interface oscillations in reaction-diffusion systems above the hopf bifurcation, *Discrete and Continuous Dynamical Systems-Series B* 17 (7).
- [42] J. E. Pearson, Complex patterns in a simple system, *Science* 261 (5118) (1993) 189–192.
- [43] A. Doelman, R. A. Gardner, T. J. Kaper, A stability index analysis of 1-D patterns of the Gray-Scott model, *American Mathematical Soc.*, 2002.
- [44] A. Doelman, T. J. Kaper, W. Eckhaus, Slowly modulated two-pulse solutions in the gray-scott model i: Asymptotic construction and stability, *SIAM Journal on Applied Mathematics* 61 (3) (2000) 1080–1102.

- [45] C. Muratov, V. Osipov, Traveling spike autosolitons in the gray–scott model, *Physica D: Nonlinear Phenomena* 155 (1) (2001) 112–131.
- [46] T. Kolokolnikov, M. J. Ward, J. Wei, The existence and stability of spike equilibria in the one-dimensional gray–scott model: the pulse-splitting regime, *Physica D: Nonlinear Phenomena* 202 (3) (2005) 258–293.
- [47] C. Muratov, V. Osipov, Spike autosolitons and pattern formation scenarios in the two-dimensional gray-scott model, *The European Physical Journal B-Condensed Matter and Complex Systems* 22 (2) (2001) 213–221.
- [48] M. J. Ward, J. Wei, The existence and stability of asymmetric spike patterns for the schnakenberg model, *Studies in Applied Mathematics* 109 (3) (2002) 229–264.
- [49] J. Wei, M. Winter, Stationary multiple spots for reaction–diffusion systems, *Journal of mathematical biology* 57 (1) (2008) 53–89.
- [50] T. Kolokolnikov, M. J. Ward, J. Wei, Spot self-replication and dynamics for the schnakenburg model in a two-dimensional domain, *Journal of nonlinear science* 19 (1) (2009) 1–56.
- [51] D. Iron, J. Wei, M. Winter, Stability analysis of turing patterns generated by the schnakenberg model, *Journal of mathematical biology* 49 (4) (2004) 358–390.
- [52] Y. Nishiura, D. Ueyama, Spatio-temporal chaos for the gray–scott model, *Physica D: Nonlinear Phenomena* 150 (3) (2001) 137–162.
- [53] W. Chen, M. J. Ward, The stability and dynamics of localized spot patterns in the two-dimensional Gray-Scott model., *SIAM J. Appl. Dynam. Systems*, 2010.
- [54] W. Chen, M. J. Ward, Oscillatory instabilities and dynamics of multi-spike patterns for the one-dimensional gray-scott model, *European Journal of Applied Mathematics* 20 (2009) 187–214.
- [55] J. Tzou, A. Bayliss, B. Matkowsky, V. Volpert, Stationary and slowly moving localised pulses in a singularly perturbed brusselator model, *European Journal of Applied Mathematics* 22 (5) (2011) 423–453.
- [56] D. Iron, M. J. Ward, J. Wei, The stability of spike solutions to the one-dimensional gierer–meinhardt model, *Physica D: Nonlinear Phenomena* 150 (1) (2001) 25–62.
- [57] M. J. Ward, J. Wei, Hopf bifurcations and oscillatory instabilities of spike solutions for the one-dimensional gierer-meinhardt model, *Journal of Nonlinear Science* 13 (2) (2003) 209–264.
- [58] J. Wei, M. Winter, *Mathematical aspects of pattern formation in biological systems*, Vol. 189, Springer Science & Business Media, 2013.

- [59] T. Kolokolnikov, M. J. Ward, J. Wei, The existence and stability of spike equilibria in the one-dimensional gray–scott model: The low feed-rate regime, *Studies in Applied Mathematics* 115 (1) (2005) 21–71.
- [60] I. Barrass, E. J. Crampin, P. K. Maini, Mode transitions in a model reaction–diffusion system driven by domain growth and noise, *Bulletin of mathematical biology* 68 (5) (2006) 981–995.
- [61] E. Gaffney, N. Monk, Gene expression time delays and turing pattern formation systems, *Bulletin of mathematical biology* 68 (1) (2006) 99–130.
- [62] M. J. Ward, J. Wei, Hopf bifurcation of spike solutions for the shadow Gierer–Meinhardt model, *Europ. J. Appl. Math.* 14 (6) (2003) 677–711.
- [63] D. Iron, M. J. Ward, A metastable spike soluton for a non-local reaction-diffusion model, *SIAM J. Appl. Math.* 60 (3) (2000) 778–802.
- [64] S. Redner, *A guide to first-passage processes*, Cambridge University Press, 2001.
- [65] F. W. D. Toussaint, Particleantiparticle annihilation in diffusive motion, *The Journal of Chemical Physics* 78 (5).
- [66] A. Szabo, R. Zwanzig, N. Agmon, Diffusion-controlled reactions with mobile traps, *Physical review letters* 61 (21) (1988) 2496.
- [67] A. J. Bray, R. A. Blythe, Exact asymptotics for one-dimensional diffusion with mobile traps, *Physical review letters* 89 (15) (2002) 150601.
- [68] M. Bramson, J. L. Lebowitz, Asymptotic behavior of densities in diffusion-dominated annihilation reactions, *Physical review letters* 61 (21) (1988) 2397.
- [69] N. Komarov, P. Winkler, Capturing the drunk robber on a graph, arXiv preprint arXiv:1305.4559.
- [70] A. Kehagias, D. Mitsche, P. Prałat, Cops and invisible robbers: The cost of drunkenness, *Theoretical Computer Science* 481 (2013) 100–120.
- [71] G. Oshanin, O. Vasilyev, P. Krapivsky, J. Klafter, Survival of an evasive prey, *Proceedings of the National Academy of Sciences* 106 (33) (2009) 13696–13701.
- [72] A. Gabel, S. N. Majumdar, N. K. Panduranga, S. Redner, Can a lamb reach a haven before being eaten by diffusing lions?, *Journal of Statistical Mechanics: Theory and Experiment* 2012 (05) (2012) P05011.
- [73] O. Bénichou, M. Coppey, M. Moreau, P. Suet, R. Voituriez, Optimal search strategies for hidden targets, *Physical review letters* 94 (19) (2005) 198101.
- [74] T. H. Chung, G. A. Hollinger, V. Isler, Search and pursuit-evasion in mobile robotics, *Autonomous Robots* 31 (4) (2011) 299–316.

- [75] A. B. R. Blythe, Survival probability of a diffusing particle in the presence of poisson-distributed mobile traps, *Physical Review E* 67 (4) (2003) 041101.
- [76] M. Moreau, G. Oshanin, O. Bénichou, M. Coppey, Pascal principle for diffusion-controlled trapping reactions, *Physical Review E* 67 (4) (2003) 045104.
- [77] O. M. Moreau, G. Oshanin, M. Coppey, Lattice theory of trapping reactions with mobile species, *Physical Review E* 69 (4) (2004) 046101.
- [78] Y. Castin, R. Dum, Bose-einstein condensates with vortices in rotating traps, *The European Physical Journal D-Atomic, Molecular, Optical and Plasma Physics* 7 (3) (1999) 399–412.
- [79] A. L. Fetter, Rotating trapped bose-einstein condensates, *Reviews of Modern Physics* 81 (2) (2009) 647.
- [80] A. Aftalion, *Vortices in Bose-Einstein Condensates*, Vol. 67, Springer Science & Business Media, 2007.
- [81] E. H. Lieb, R. Seiringer, J. Yngvason, A rigorous derivation of the gross-pitaevskii energy functional for a two-dimensional bose gas, *Communications in Mathematical Physics* 224 (1) (2001) 17–31.
- [82] E. H. Lieb, R. Seiringer, Derivation of the gross-pitaevskii equation for rotating bose gases, *Communications in mathematical physics* 264 (2) (2006) 505–537.
- [83] J. Abo-Shaeer, C. Raman, J. Vogels, W. Ketterle, Observation of vortex lattices in bose-einstein condensates, *Science* 292 (5516) (2001) 476–479.
- [84] K. Madison, F. Chevy, W. Wohlleben, J. Dalibard, Vortex formation in a stirred bose-einstein condensate, *Physical Review Letters* 84 (5) (2000) 806.
- [85] S. Serfaty, On a model of rotating superfluids, *ESAIM: Control, Optimisation and Calculus of Variations* 6 (2001) 201–238.
- [86] R. Ignat, V. Millot, The critical velocity for vortex existence in a two-dimensional rotating bose-einstein condensate, *Journal of Functional Analysis* 233 (1) (2006) 260–306.
- [87] R. Ignat, V. Millot, Energy expansion and vortex location for a two-dimensional rotating bose-einstein condensate, *Reviews in Mathematical Physics* 18 (02) (2006) 119–162.
- [88] V. Bretin, S. Stock, Y. Seurin, J. Dalibard, Fast rotation of a bose-einstein condensate, *Physical review letters* 92 (5) (2004) 050403.
- [89] V. Schweikhard, I. Coddington, P. Engels, V. Mogendorff, E. A. Cornell, Rapidly rotating bose-einstein condensates in and near the lowest landau level, *Physical review letters* 92 (4) (2004) 040404.

- [90] D. E. Sheehy, L. Radzihovsky, Vortices in spatially inhomogeneous superfluids, *Physical Review A* 70 (6) (2004) 063620.
- [91] D. E. Sheehy, L. Radzihovsky, Vortex lattice inhomogeneity in spatially inhomogeneous superfluids, *Physical Review A* 70 (5) (2004) 051602.
- [92] M. Correggi, N. Rougerie, Inhomogeneous vortex patterns in rotating bose-einstein condensates, *Communications in Mathematical Physics* 321 (3) (2013) 817–860.
- [93] J.-k. Kim, A. L. Fetter, Dynamics of a single ring of vortices in two-dimensional trapped bose-einstein condensates, *Physical Review A* 70 (4) (2004) 043624.
- [94] A. A. Svidzinsky, A. L. Fetter, Dynamics of a vortex in a trapped bose-einstein condensate, *Physical Review A* 62 (6) (2000) 063617.
- [95] A. A. Svidzinsky, A. L. Fetter, Stability of a vortex in a trapped bose-einstein condensate, *Physical review letters* 84 (26) (2000) 5919.
- [96] L. Pismen, J. Rubinstein, Motion of vortex lines in the ginzburg-landau model, *Physica D: Nonlinear Phenomena* 47 (3) (1991) 353–360.
- [97] B. Rubinstein, L. Pismen, Vortex motion in the spatially inhomogeneous conservative ginzburg-landau model, *Physica D: Nonlinear Phenomena* 78 (1-2) (1994) 1–10.
- [98] T. Ohta, A. Ito, A. Tetsuka, Self-organization in an excitable reaction-diffusion system: synchronization of oscillatory domains in one dimension., *Physical Review A* 42 (1990) 3225.
- [99] M. Ikeda, T. Mimura, An interfacial approach to regional segregation of two competing species mediated by a predator., *Journal of Mathematical Biology* 31 (1993) 215–240.
- [100] C.-C. Chen, T. Kolokolnikov, Simple pde model of spot replication in any dimension, *SIAM Journal on Mathematical Analysis* 44 (5) (2012) 3564–3593.
- [101] A. LINDSAY, J. TZOU, T. KOLOKOLNIKOV, Optimization of first passage times by multiple cooperating mobile traps, Submitted, M3AS.
- [102] Y. Nishiura, T. Teramoto, K.-I. Ueda, Scattering of traveling spots in dissipative systems, *Chaos: An Interdisciplinary Journal of Nonlinear Science* 15 (4) (2005) 047509.
- [103] P. Van Heijster, B. Sandstede, Bifurcations to travelling planar spots in a three-component fitzhugh-nagumo system, *Physica D: Nonlinear Phenomena* 275 (2014) 19–34.

- [104] T. Ohta, T. Ohkuma, Deformable self-propelled particles, *Physical review letters* 102 (15) (2009) 154101.
- [105] P. Trinh, M. J. Ward, The dynamics of localized spot patterns for reaction-diffusion systems on the sphere, *Nonlinearity* 29 (3) (2016) 766–806.
- [106] I. Rozada, S. Ruuth, M. J. Ward, The stability of localized spot patterns for the Brusselator on the sphere, *SIAM J. Appl. Dyn. Sys.* 13 (1) (2014) 564–627.
- [107] FlexPDE6, PDE Solutions Inc. URL <http://www.pdesolutions.com>.
- [108] A. Cheviakov, M. J. Ward, Optimizing the principal eigenvalue of the Laplacian in a sphere with interior traps, *Math. and Comp. Modeling* 53 (7-8) (2011) 1394–1409.
- [109] L. Greengard, V. Rokhlin, A new version of the fast multipole method for the laplace equation in three dimensions, *Acta Numerica* 6 (1997) 229–269.
- [110] W. Stortelder, J. de Swart, J. Pintér, Finding elliptic Fekete point sets: Two numerical solution approaches, *J. Comput. Appl. Math.* 130 (1-2) (1998) 205–216.
- [111] S. Xie, T. Kolokolnikov, P. G. Kevrekidis, Multiple vortex lattices in bose-einstein condensate with a rotating trap.
- [112] M. Tsubota, K. Kasamatsu, M. Ueda, Vortex lattice formation in a rotating bose-einstein condensate, *Physical Review A* 65 (2) (2002) 023603.
- [113] A. Penckwitt, R. Ballagh, C. Gardiner, Nucleation, growth, and stabilization of bose-einstein condensate vortex lattices, *Physical review letters* 89 (26) (2002) 260402.
- [114] D. L. Feder, C. W. Clark, B. I. Schneider, Vortex stability of interacting bose-einstein condensates confined in anisotropic harmonic traps, *Physical review letters* 82 (25) (1999) 4956.
- [115] A. Aftalion, Q. Du, Vortices in a rotating bose-einstein condensate: Critical angular velocities and energy diagrams in the thomas-fermi regime, *Physical Review A* 64 (6) (2001) 063603.
- [116] T. Kolokolnikov, P. Kevrekidis, R. Carretero-González, A tale of two distributions: from few to many vortices in quasi-two-dimensional bose-einstein condensates, *The Royal Society* 470 (2168) (2014) 20140048.
- [117] R. Navarro, R. Carretero-González, P. Torres, P. Kevrekidis, D. Frantzeskakis, M. Ray, E. Altuntaş, D. Hall, Dynamics of a few corotating vortices in bose-einstein condensates, *Physical review letters* 110 (22) (2013) 225301.

- [118] V. Schweikhard, I. Coddington, P. Engels, S. Tung, E. A. Cornell, Vortex-lattice dynamics in rotating spinor bose-einstein condensates, *Physical review letters* 93 (21) (2004) 210403.
- [119] K. Kasamatsu, M. Tsubota, M. Ueda, Vortices in multicomponent bose-einstein condensates, *International Journal of Modern Physics B* 19 (11) (2005) 1835–1904.
- [120] F. Bethuel, H. Brezis, F. Hélein, *Ginzburg-Landau Vortices*, Vol. 13, Springer Science & Business Media, 2012.
- [121] C. Raman, J. Abo-Shaeer, J. Vogels, K. Xu, W. Ketterle, Vortex nucleation in a stirred bose-einstein condensate, *Physical review letters* 87 (21) (2001) 210402.
- [122] Y. V. Shestopalov, Y. G. Smirnov, *Integral equations*, Karlstad University, Karlstad.
- [123] R. C. Fetecau, Y. Huang, T. Kolokolnikov, Swarm dynamics and equilibria for a nonlocal aggregation model, *Nonlinearity* 24 (10) (2011) 2681.
- [124] J. Anglin, Local vortex generation and the surface mode spectrum of large bose-einstein condensates, *Physical review letters* 87 (24) (2001) 240401.
- [125] R. Carretero-González, P. G. Kevrekidis, T. Kolokolnikov, Vortex nucleation in a dissipative variant of the nonlinear schrödinger equation under rotation, *Physica D: Nonlinear Phenomena* 317 (2016) 1–14.
- [126] J. C. Tzou, P. G. Kevrekidis, T. Kolokolnikov, R. Carretero-Gonzalez, Weakly nonlinear analysis of vortex formation in a dissipative variant of the gross-pitaevskii equation, *SIAM Journal on Applied Dynamical Systems* 15 (2) (2016) 904–922.
- [127] O. Bénichou, R. Voituriez, From first-passage times of random walks in confinement to geometry-controlled kinetics, *Physics Reports* 539 (4) (2014) 225–284.
- [128] T. Kolokolnikov, J. Wei, Pattern formation in a reaction-diffusion system with space-dependent feed rate.
- [129] S. Gurevich, S. Amiranashvili, H.-G. Purwins, Breathing dissipative solitons in three-component reaction-diffusion system, *Physical Review E* 74 (6) (2006) 066201.